Theory of Superconducting Quantum Devices and Reconfigurable Quantum Materials for Quantum Computing Applications

by

Nicholas M. Hougland

B.S. in Physics, Carnegie Mellon University, 2019

B.S. in Mathematics, Carnegie Mellon University, 2019

M.S. in Physics, University of Pittsburgh, 2021

Submitted to the Graduate Faculty of

the Dietrich School of Arts and Sciences in partial fulfillment

of the requirements for the degree of

Doctor of Philosophy

University of Pittsburgh

2025

UNIVERSITY OF PITTSBURGH

KENNETH P. DIETRICH SCHOOL OF ARTS AND SCIENCES

This dissertation was presented

by

Nicholas M. Hougland

It was defended on

July 13, 2025

and approved by

David Pekker, Associate Professor, Department of Physics and Astronomy

Jeremy Levy, Distinguished Professor, Department of Physics and Astronomy

Roger Mong, Associate Professor, Department of Physics and Astronomy

Michael Wood-Vasey, Professor, Department of Physics and Astronomy

Roy Briere, Professor, Carnegie Mellon University Department of Physics

Theory of Superconducting Quantum Devices and Reconfigurable Quantum Materials for Quantum Computing Applications

Nicholas M. Hougland, PhD

University of Pittsburgh, 2025

The physics of quantum devices is a vast and growing field with active research into many emerging technologies based on quantum effects. In particular, new devices which rely on the quantum properties of superconducting materials, as well as technologies which allow for fine control of the superconductivity in such materials, are being developed. However, a major limitation on practical hardware which takes advantage of quantum effects is scaling. Quantum systems are naturally susceptible to the effects of noise, which can destroy useful properties of practical quantum hardware. This is especially true in quantum computing, which represents a major application for quantum hardware. In this field, quantum information which relies on the coherence of many qubits is easily destroyed.

In addition to quantum computing, quantum hardware based on superconducting materials can be used in a variety of applications. This is because superconducting devices can be engineered with various properties to build components such as amplifiers and masers which have broad applicability. These classes of devices are useful in all areas of physics and engineering, including radio astronomy and communication where amplification of small signals is essential, as well as atomic physics and even molecular biology, which rely on sources of coherent light for fine control and probing of atoms and molecules.

In this Dissertation, I theoretically investigate the properties of superconducting quantum hardware and how they can be used to design new devices for various applications. I will describe my work on examining fundamental properties of reconfigurable materials which may prove useful in these applications, in particular by modeling and engineering the band structure of graphene with an electrostatic potential and by modeling supercurrents in 2D superconductors at complex oxide heterointerfaces. Then I will describe designing superconducting hardware which relies on the nonlinearity of Josephson junctions, specifically amplifiers and masers. These devices each represent a significant new property or

improvement in performance along some dimension as compared to the quantum hardware of the past, and the further investigation of these properties in this Dissertation lays the groundwork for building useful quantum devices which can be practically realized.

Table of Contents

List of Tables

List of Figures

Preface

Over the last several years as I have pursued my PhD, I have had the support of so many loving friends and family, as well as mentorship from my advisor and collaborators, and I could not have arrived where I am today without them. First and foremost, I want to thank my advisor, David Pekker, for taking me on as a student and for going above and beyond the level of advisement that I thought possible during a time when we could meet only remotely. David helped me grow my interest in pursuing research in quantum theory into a career path that I'm excited to follow.

I would like to thank my collaborators Roger Mong, Jeremy Levy, and Michael Hatridge. I had the opportunity to work with Dr. Mong and his student, Zhuan Li, on joint theory research which I could not have completed on my own. Dr. Levy and Dr. Hatridge both gave me experience working directly with experimentalists, which has guided me to a career path where I continue to do theory in collaboration with experimental research. It was a pleasure to discuss our work with their students, Muqing Yu, Ranjani Ramachandran, Maria Mucci, Ryan Kaufman, Boris Mesits, Maria Nowicki, and Chun-Che Wang.

I thank Roy Briere for introducing me to doing my own research in physics, and for giving me the academic freedom and independence to pursue my interests. His guidance and our weekly physics discussions solidified my desire to go to grad school, and I could not have gotten here without my experience as his student as my foundation.

My family has been extremely supportive and has always encouraged me, even when the path to where I am today seemed difficult. My parents instilled in me the value of education from an early age, and I have carried that with me as I strove to earn my PhD. My sister Juliana was always there for me as my closest family and roommate, and I could always rely on her to keep me centered. I am incredibly grateful to my extended family, especially my grandparents and all my aunts and uncles in Brazil, who have followed my graduate career closely and showed such interest in my work. I feel so lucky to have a large support network of family who I know I can count on.

I am so happy to have met some of my closest friends while in grad school, including

Amy, Emily, Melanie, MK, Param, Ryan, and Travis. I had more fun as a PhD student than I ever expected, and I'm so glad I could share the good times with you.

Finally, I owe it all to my best friend, my love, Mary Garrett. You have given my life so much joy and happiness, and I can't imagine doing any of this without you. Even through hard times, being with you makes it all easier. You make me want to be a better scientist and a better person, and I am so excited for the next phase in my life with you.

1.0 Introduction

Superconductivity was discovered in 1911 by Kamerlingh Onnes [109] (or perhaps his graduate student [103]) when it was observed that mercury exhibited zero electrical resistance at temperatures below 4.2K. This discovery, along with subsequent discoveries of properties of superconductors, has prompted investigation into theoretical explanations of these phenomena. The impetus for a deeper understanding of superconductivity often stems from the desire to take advantage of superconducting properties for practical applications. Throughout this Dissertation, we will investigate theoretical models for superconducting systems and devices which we anticipate may be useful in quantum computing applications in particular. In this Chapter, we will introduce established theoretical models which describer superconductivity, and which form the basis for our work in later Chapters.

We begin by introducing the Bardeen-Cooper-Schrieffer (BCS) model of superconductivity in Section 1.1.1, which explains the origin of superconductivity from a microscopic perspective. While we do not make direct use of the BCS theory in this thesis, the BCS theory is a strong motivator for designing materials (or meta-materials) with a high density of states in order to promote the formation of strongly correlated states, which is the subject of Chapter 2. Next, in Section 1.1.2, we introduce the phenomenological/macroscopic theory of Ginzburg and Landau which we refer to in Chapter 3 to model supercurrents in nanoscale superconducting quantum interference devices. In Section 1.1.3 we then introduce the theory of the Josephson effects, which describe supercurrents through and voltages across junction between pairs of superconductors. We also argue that the Josephson relation for the current results in the DC-SQUID effect, i.e. flux quantization in superconducting devices with pairs of Josephson junction. The DC-SQUIDs in the novel superconductor formed at the interface of two complex metal oxides is the central topic of Chapter 3. Finally, in Section 1.2, we introducing circuit quantum electrodynamics (cQED), which is the theory of superconducting circuits that plays a crucial role in our investigation of superconducting parametric amplifiers in Chapter 4 and superconducting micromaser circuits made of qubits in Chapter 4.

1.1 Superconductivity

1.1.1 Bardeen-Cooper-Schrieffer theory of superconductivity

While superconductors had been phenomenologically studied since their discovery in 1911, a microscopic theory for the origin of superconductivity was not developed until 1957, when Bardeen, Cooper, and Schrieffer proposed a theory by which electrons would form a bound state known as a Cooper pair. This theory has become known as BCS theory, and is the accepted model for the origin of superconductivity in low-temperature superconductors. In this Subsection, we will derive important results of the BCS theory, primarily following the derivation in Chapter 3 of Refs. [109][1] and originally formulated by Bardeen, Cooper, and Schrieffer in Ref. [7].

We will first present Cooper's argument which shows that under the presence of an attractive potential, even if it is very weak, the electrons will form Cooper pairs. We will consider the case of two electrons added to the Fermi sea at temperature $T = 0$, where these electrons do not interact with the electrons in the sea (except for Pauli blocking). We will consider a wavefunction for the two electrons with equal and opposite momenta and opposite spin, i.e.

$$\Psi(\mathbf{r_1}, \mathbf{r_2}) = \sum_{\mathbf{k}} g_{\mathbf{k}} e^{i\mathbf{k}(\mathbf{r_1}-\mathbf{r_2})}(|\uparrow\downarrow\rangle - |\downarrow\uparrow\rangle), \tag{1}$$

where $g_{\mathbf{k}}$ is the amplitude for the pair being in the $\mathbf{k}, -\mathbf{k}$ state, and Pauli blocking by the electrons in the Fermi sea requires that $|\mathbf{k}| > k_F$. We insert this to the Schrodinger equation, $H\Psi = E\Psi$, to get

$$\sum_{\mathbf{k}} g_{\mathbf{k}}\big(\epsilon_{\mathbf{k}} + \epsilon_{\mathbf{k}} + V(\mathbf{r_1} - \mathbf{r_2})\big)e^{i\mathbf{k}(\mathbf{r_1}-\mathbf{r_2})} = E\sum_{\mathbf{k}} g_{\mathbf{k}} e^{i\mathbf{k}(\mathbf{r_1}-\mathbf{r_2})}, \tag{2}$$

where $\epsilon_{\mathbf{k}}$ is the kinetic energy of each electron (and we have assumed that $\epsilon_{\mathbf{k}} = \epsilon_{|\mathbf{k}|}$). Then, we can write this as

$$2\epsilon_{\mathbf{k}} g_{\mathbf{k}}\Omega + \sum_{\mathbf{k'}>\mathbf{k_F}} \int d^3\mathbf{r} g_{\mathbf{k'}} V(\mathbf{r}) e^{i(\mathbf{k'}-\mathbf{k})\cdot\mathbf{r}} = E g_{\mathbf{k}}\Omega, \tag{3}$$

[1] Other useful references include [1] and [59].

where we have integrated over space so that Ω is the normalization volume. Finally, we can write this as

$$(E - 2\epsilon_{\mathbf{k}})g_{\mathbf{k}} = \sum_{\mathbf{k}'>\mathbf{k_F}} V_{\mathbf{k}\mathbf{k}'}g_{\mathbf{k}'}, \tag{4}$$

where

$$V_{\mathbf{k}\mathbf{k}'} = \frac{1}{\Omega}\int d^3\mathbf{r}V(\mathbf{r})e^{i(\mathbf{k}'-\mathbf{k})\cdot\mathbf{r}}. \tag{5}$$

We will now approximate $V_{\mathbf{k}\mathbf{k}'}$ as a constant attractive potential. I.e. it has strength $-V$ for all $\mathbf{k}$ states with energy from E_F to $E_F + \hbar\omega_c$. Beyond this cutoff energy, the potential is zero. Plugging in this potential, we have

$$g_{\mathbf{k}} = \frac{-V\sum_{\mathbf{k}'>\mathbf{k_F}} g_{\mathbf{k}'}}{E - 2\epsilon_{\mathbf{k}}}. \tag{6}$$

We can sum over $\mathbf{k}$ and get

$$\frac{1}{V} = \sum_{\mathbf{k}>\mathbf{k_F}} (2\epsilon_{\mathbf{k}} - E)^{-1}. \tag{7}$$

We can convert this into an integral over energy, and obtain

$$\frac{1}{V} = N_0\int_{E_F}^{E_F+\hbar\omega_c} \frac{d\epsilon}{2\epsilon - E} = \frac{N_0}{2}\ln\frac{2E_F - E + 2\hbar\omega_c}{2E_F - E}, \tag{8}$$

where N_0 is the density of states at the Fermi level. For $N_0V \ll 1$, the solution for E can be written as

$$E \approx 2E_F - 2\hbar\omega_c e^{-2/N_0V}. \tag{9}$$

That is, the energy for a bound state of two electrons is below the Fermi level, favoring the formation of Cooper pairs. Typically, in 3D, bound states only appear when an attractive interaction is sufficiently strong. On the other hand, due to the Fermi sea blocking states with $k < k_F$, the Cooper problem supports a bound state of two electrons in 3D no matter how weak the attractive interaction V is. This remarkable property implies that even weak attractive interactions can lead to the breakdown of the Fermi sea and the formation of a superconducting state composed of electron pairs, which we describe below.

To imagine how an attractive potential between electrons could arise despite the Coulomb repulsion between them, we must consider the effect of the lattice of ions in the material. In particular, the presence of an electron near positive ions will induce a lattice deformation, leading to a net positive charge in the region. The ion lattice returns slowly to equilibrium compared to other electrons, which are attracted to this region. The net effect is an attraction between electrons which is mediated by phonons induced by the Coulomb interaction.

Since we have shown that the presence of an attractive potential between electrons will lead to Cooper pairs, we now realize that these pairs will continue to form until we reach a new ground state. This state is reached when the binding energy of an additional Cooper pair reaches zero. We will take a second quantization approach to write down the wavefunction for this BCS ground state.

We will use $c_{\mathbf{k},\sigma}$ and $c^\dagger_{\mathbf{k},\sigma}$, the annihilation and creation operators for an electron with momentum $\mathbf{k}$ and spin σ. These operators obey the anticommutation relations

$$\{c_{\mathbf{k},\sigma}, c^\dagger_{\mathbf{k}',\sigma'}\} = \delta_{\mathbf{k}\mathbf{k}'}\delta_{\sigma\sigma'}, \tag{10}$$

$$\{c_{\mathbf{k},\sigma}, c_{\mathbf{k}',\sigma'}\} = \{c^\dagger_{\mathbf{k},\sigma}, c^\dagger_{\mathbf{k}',\sigma'}\} = 0. \tag{11}$$

We will start with the pairing Hamiltonian for the system, expressed as

$$H = \sum_{\mathbf{k},\sigma} \epsilon_{\mathbf{k}} n_{\mathbf{k},\sigma} + \sum_{\mathbf{k},\mathbf{l}} V_{\mathbf{k}\mathbf{l}} c^\dagger_{\mathbf{k},\uparrow} c^\dagger_{-\mathbf{k},\downarrow} c_{-\mathbf{l},\downarrow} c_{\mathbf{l},\uparrow}, \tag{12}$$

where $n_{\mathbf{k},\sigma}$ is the electron number operator. We now define $b_{\mathbf{k}} = \langle c_{-\mathbf{k},\downarrow} c_{\mathbf{k},\uparrow} \rangle$ as the expectation value of $c_{-\mathbf{k},\downarrow} c_{\mathbf{k},\uparrow}$, which due to Cooper pairing may be nonzero (without such pairing, this should average to zero). We will also define the gap energy as

$$\Delta_{\mathbf{k}} = -\sum_{\mathbf{l}} V_{\mathbf{k}\mathbf{l}} b_{\mathbf{l}}. \tag{13}$$

Finally, we will take $H \to H + \mu N$ where μ is the chemical potential (Fermi energy) and N is the particle number operator. Then, we can write the Hamiltonian as

$$H = \sum_{\mathbf{k},\sigma} \xi_{\mathbf{k}} n_{\mathbf{k},\sigma} - \sum_{\mathbf{k}} (\Delta_{\mathbf{k}} c^\dagger_{\mathbf{k},\uparrow} c^\dagger_{-\mathbf{k},\downarrow} + \Delta^\dagger_{\mathbf{k}} c_{-\mathbf{k},\downarrow} c_{\mathbf{k},\uparrow} - \Delta_{\mathbf{k}} b^\dagger_{\mathbf{k}}), \tag{14}$$

where $\xi_{\mathbf{k}} = \epsilon_{\mathbf{k}} - \mu$.

We will now diagonalize the Hamiltonian, which has been shown by Bogoliubov and by Valatin to be possible by implementing the following linear transformation:

$$c_{\mathbf{k},\uparrow} = u_{\mathbf{k}}^{\dagger}\gamma_{\mathbf{k},0} + v_{\mathbf{k}}\gamma_{\mathbf{k},1}^{\dagger} \tag{15}$$

$$c_{\mathbf{k},\uparrow}^{\dagger} = -v_{\mathbf{k}}^{\dagger}\gamma_{\mathbf{k},0} + u_{\mathbf{k}}\gamma_{\mathbf{k},1}^{\dagger}, \tag{16}$$

where $|u_{\mathbf{k}}|^2 + |v_{\mathbf{k}}|^2 = 1$. By this construction, new operator $\gamma_{\mathbf{k},0}$ has components which destroy an electron with $\mathbf{k},\uparrow$ and a component with creates an electron with $-\mathbf{k},\downarrow$, i.e. it decreases momentum of the system by k and decreases S_z by $\hbar/2$. Similar properties hold for $\gamma_{\mathbf{k},1}^{\dagger}$ and conjugates.

We can now write the Hamiltonian as

$$\begin{aligned} H = \sum_{\mathbf{k}} \xi_{\mathbf{k}}[(|u_{\mathbf{k}}|^2 + |v_{\mathbf{k}}|^2)(\gamma_{\mathbf{k},0}^{\dagger}\gamma_{\mathbf{k},0} + \gamma_{\mathbf{k},1}^{\dagger}\gamma_{\mathbf{k},1}) + 2|v_{\mathbf{k}}|^2 + 2u_{\mathbf{k}}^{\dagger}v_{\mathbf{k}}^{\dagger}\gamma_{\mathbf{k},1}\gamma_{\mathbf{k},0} \\ +2u_{\mathbf{k}}v_{\mathbf{k}}\gamma_{\mathbf{k},0}^{\dagger}\gamma_{\mathbf{k},1}^{\dagger}] + \sum_{\mathbf{k}}[(\Delta_{\mathbf{k}}u_{\mathbf{k}}v_{\mathbf{k}}^{\dagger} + \Delta_{\mathbf{k}}^{\dagger}u_{\mathbf{k}}^{\dagger}v_{\mathbf{k}})(\gamma_{\mathbf{k},0}^{\dagger}\gamma_{\mathbf{k},0} + \gamma_{\mathbf{k},1}^{\dagger}\gamma_{\mathbf{k},1} - 1) \\ +(\Delta_{\mathbf{k}}v_{\mathbf{k}}^{\dagger 2} - \Delta_{\mathbf{k}}^{\dagger}u_{\mathbf{k}}^{\dagger 2})\gamma_{\mathbf{k},1}\gamma_{\mathbf{k},0} + (\Delta_{\mathbf{k}}^{\dagger}v_{\mathbf{k}}^{2} - \Delta_{\mathbf{k}}u_{\mathbf{k}}^{2})\gamma_{\mathbf{k},0}^{\dagger}\gamma_{\mathbf{k},1}^{\dagger} + \Delta_{\mathbf{k}}b_{\mathbf{k}}^{\dagger}]. \end{aligned} \tag{17}$$

This Hamiltonian is diagonal when $\gamma_{\mathbf{k},1}\gamma_{\mathbf{k},0}$ and $\gamma_{\mathbf{k},0}^{\dagger}\gamma_{\mathbf{k},1}^{\dagger}$ terms are zero. This is when the coefficients satisfy $2\xi_{\mathbf{k}}u_{\mathbf{k}}v_{\mathbf{k}} + \Delta_{\mathbf{k}}^{\dagger}v_{\mathbf{k}}^2 - \Delta_{\mathbf{k}}u_{\mathbf{k}}^2 = 0$. Or rather,

$$\frac{\Delta_{\mathbf{k}}^{\dagger}v_{\mathbf{k}}}{u_{\mathbf{k}}} = (\xi_{\mathbf{k}}^2 + |\Delta_{\mathbf{k}}|^2)^{1/2} - \xi_{\mathbf{k}} \equiv E_{\mathbf{k}} - \xi_{\mathbf{k}}, \tag{18}$$

where we have implicitly defined $E_{\mathbf{k}} = (\xi_{\mathbf{k}}^2 + |\Delta_{\mathbf{k}}|^2)^{1/2}$. Finally, taking into account the normalization requirement on the coefficients, we have

$$|v_{\mathbf{k}}|^2 = 1 - |u_{\mathbf{k}}|^2 = \frac{1}{2}\left(1 - \frac{\xi_{\mathbf{k}}}{E_{\mathbf{k}}}\right). \tag{19}$$

The phases of $\Delta_{\mathbf{k}}, u_{\mathbf{k}}$, and $v_{\mathbf{k}}$ are related by Eq. (18), while their global phase is arbitrary. We plot $|v_{\mathbf{k}}|^2, |u_{\mathbf{k}}|^2$ in Fig. 1.

We can then consider writing the general BCS ground state as

$$|\psi_G\rangle = \prod_{\mathbf{k},\sigma} \gamma_{\mathbf{k},\sigma}\,|\phi_0\rangle = \prod_{\mathbf{k}} \left(u_{\mathbf{k}} + v_{\mathbf{k}}c_{\mathbf{k},\uparrow}^{\dagger}c_{-\mathbf{k},\downarrow}^{\dagger}\right)|\phi_0\rangle\,, \tag{20}$$

where ϕ_0 is the vacuum state.

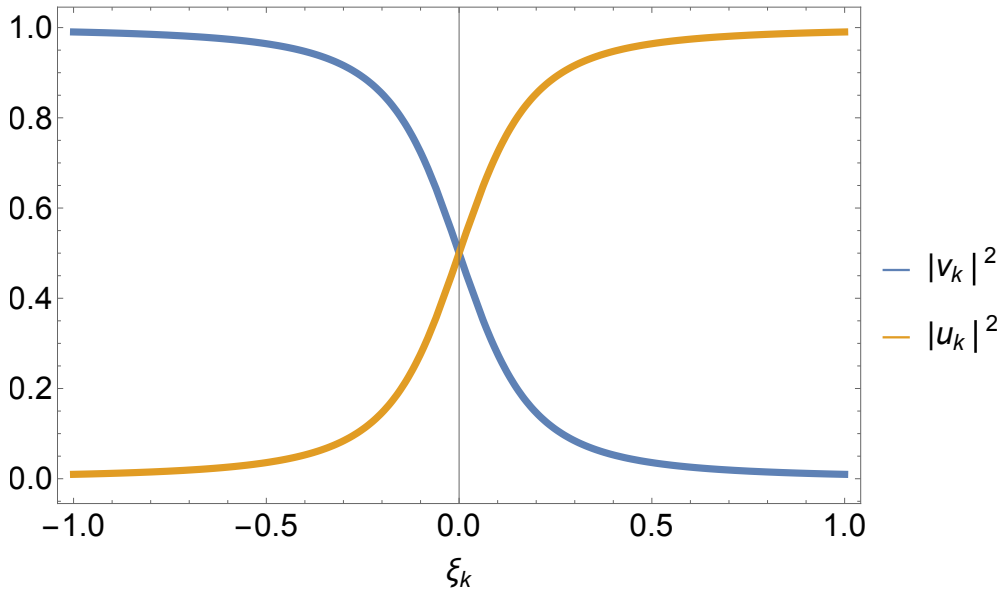

Figure 1: Occupation fraction of Cooper pair states in BCS theory.

With the choice of $u_{\mathbf{k}}$ and $v_{\mathbf{k}}$ to diagonalize the Hamiltonian, what remains is

$$H = \sum_{\mathbf{k}} (\xi_{\mathbf{k}} - E_{\mathbf{k}} + \Delta_{\mathbf{k}} b_{\mathbf{k}}^\dagger) + \sum_{\mathbf{k}} E_{\mathbf{k}} (\gamma_{\mathbf{k}0}^\dagger \gamma_{\mathbf{k}0} + \gamma_{\mathbf{k}1}^\dagger \gamma_{\mathbf{k}1}). \tag{21}$$

Thus, the $E_{\mathbf{k}}$ give the energies of excitations of the quasi-particles given by the $\gamma_{\mathbf{k}}$ operators. Even near the Fermi surface, where $\xi_{\mathbf{k}} = 0$, we have $E_{\mathbf{k}} = |\Delta_{\mathbf{k}}| > 0$, indicating a gap in the energy spectrum for quasi-particles with a minimum excitation energy of $2\Delta_{\mathbf{k}}$, unlike in a normal metal. To see this more concretely, we plot an example energy spectrum in Fig.2. The BCS ground state corresponds to where all the negative energy states are occupied.

1.1.2 Ginzburg-Landau theory of superconductivity

In the previous Section, we have focused on the microscopic theory which underlies superconductivity in conventional, low-temperature superconductors. However, in many scenarios a macroscopic, phenomenological theory is sufficient for describing superconductivity. The

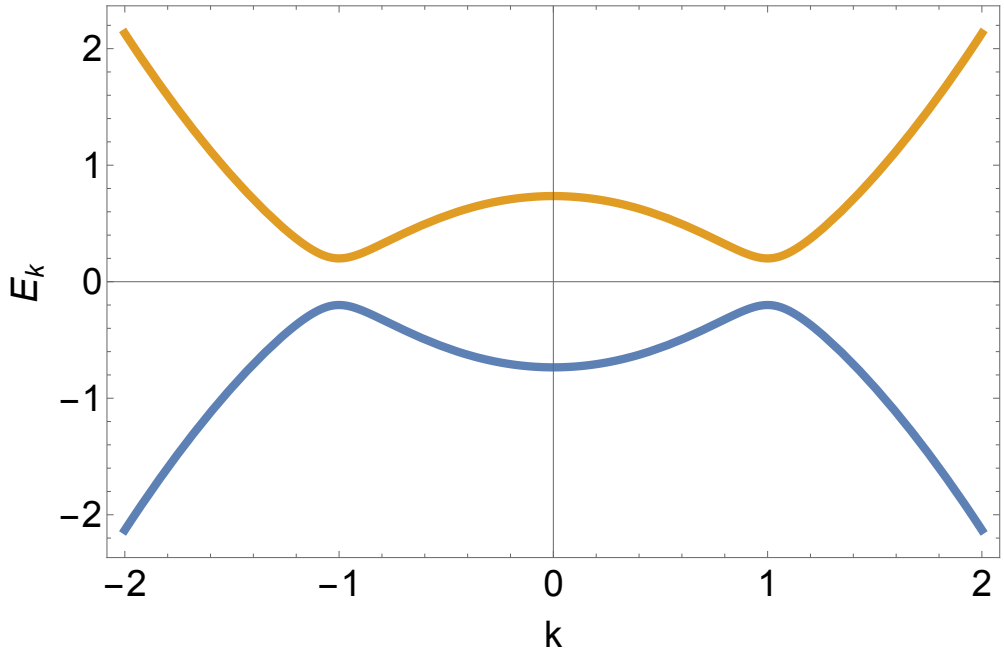

Figure 2: Positive and negative eigenvalues (energies) of Eq. (21).

Ginzburg-Landau theory represents such an approach. This theory, proposed by Ginzburg and Landau in 1950 [43], introduces a pseudowavefunction $\psi(x)$ as an order parameter, where $|\psi(x)|^2$ represents the local density of superconducting charge carriers $n_s(x)$. In this Section, we will introduce the Ginzburg-Landau free energy and consider its important properties. This presentation will follow Chapter 4 of Ref. [109].

The Ginzburg-Landau theory begins with the postulate that for ψ which is small and slowly varying in space, the free energy density can be expanded in $|\psi|^2$ and $|\nabla\psi|^2$ as

$$f = f_{n0} + \alpha|\psi|^2 + \frac{\beta}{2}|\psi|^4 + \frac{1}{2m^*}\left|\left(\frac{\hbar}{i}\nabla - \frac{e^*}{c}\mathbf{A}\right)\psi\right|^2 + \frac{\mathbf{B}^2}{8\pi}, \tag{22}$$

where $\mathbf{A}$ is the magnetic vector potential and $\mathbf{B} = \nabla \times \mathbf{A}$, and f_{n0} is the free energy of the normal state. The terms m^* and e^* are the mass and charge of the superconducting charge carriers. In the original Ginzburg-Landau theory, which predated BCS, it was assumed these terms would be the same as the electron values. However, the microscopic theory shows that the charge carriers are Cooper pairs with values $m^* = 2m$ and $e^* = 2e$.

It is possible to derive the Ginzburg-Landau theory from the microscopic BCS theory, as shown by Gor'kov [80], but we will instead assume the expanded form of f and examine the terms which describe superconducting effects, including the nonlinear effect of $\mathbf{A}$ which can change n_s.

Beginning with the case of no field $\mathbf{A}$ and no gradients of ψ, we have that the free energy of the superconducting condensate is

$$f - f_{n0} = \alpha|\psi|^2 + \frac{1}{2}\beta|\psi|^4. \tag{23}$$

When$\beta > 0$, the above free energy has a well defined minimum for a finite $|\phi|$ and hence we can minimize the free energy. In the case of positive α, the minimum of the free energy occurs when $|\psi|^2 = 0$, i.e. the superconducting electron density is zero and we have the normal state. If α is negative, then the minimum is at $|\psi|^2 = -\alpha/\beta$.

At the transition temperature T_c, α must change sign, so we can Taylor expand it as a function of $t - 1 = T/T_c - 1$ at $t = 1$ to get $\alpha = \alpha'(t - 1)$. Plugging into (23) implies that $|\psi|^2 = n_s \propto (1 - t)$, giving the relation between superconducting electron density and temperature near T_c.

The $1/2m^*$ term in the Ginzburg-Landau theory accounts for fields and gradients. We can write $\psi = |\psi|e^{i\varphi}$ and consider the term as

$$\frac{1}{2m^*}\left[\hbar^2(\nabla|\psi|)^2 + \left(\hbar\nabla\varphi - \frac{e^*\mathbf{A}}{c}\right)^2|\psi|^2\right]. \tag{24}$$

This form gives two terms, where the first is associated with the gradient of the magnitude of the order parameter. The second gives the energy due to supercurrents and variations in superconducting phase in the superconductor. The supercurrent density is given by

$$\mathbf{J} = e^*|\psi|^2\mathbf{v_s} = \frac{e^*}{m^*}|\psi|^2\left(\hbar\nabla\varphi - \frac{e^*}{c}\mathbf{A}\right), \tag{25}$$

where $\mathbf{v_s}$ is the supercurrent velocity. In Chapter 3, we will solve for supercurrents and phase gradients in a 2D superconductor by minimizing this Ginzburg-Landau free energy.

1.1.3 Josephson effect and Josephson junction-based devices

The Josephson junction is a junction of two superconducting electrodes connected by a weak link (e.g. insulating barrier, normal metal, constriction). These junctions have the property that, with zero potential difference between the superconductors, a current I_s will flow between them with

$$I_s = I_c \sin \Delta\varphi, \tag{26}$$

where I_c is the critical current of the junction and $\Delta\varphi$ is the difference in the phase of the Ginzburg-Landau wavefunction ψ between the two superconductors.

Furthermore, if a voltage V is applied across a Josephson junction, $\Delta\varphi$ will follow

$$\frac{d(\Delta\varphi)}{dt} = \frac{2eV}{\hbar} = \frac{V}{\phi_0} \tag{27}$$

such that the current alternates with frequency $2eV/h$ and $\phi_0 = \hbar/2e$ is the reduced flux quantum. These effects, known as the DC and AC Josephson effects, were predicted by Josephson in 1962 [54], and they form the basis for many important superconducting quantum devices.

One class of Josephson junction-based devices is the superconducting quantum interference device (SQUID). We will consider the operation of a DC-SQUID, and we will draw from Chapter 6 of Ref. [109].

The DC-SQUID is composed of a superconducting loop with two junctions (i.e., two Josephson junctions in parallel). This loop will enclose a flux Φ which can be found by integrating $\mathbf{A}$ around a contour through both junctions. Additionally, due to the Meissner effect of superconductors, there is a contour we can choose where the current velocity $\mathbf{v_s} = 0$ around the loop. Using Eq (25), we have $m^*\mathbf{v_s} = \hbar(\nabla\varphi - 2\pi\mathbf{A}/\Phi_0)$ so that $\mathbf{A} = (\Phi_0/2\pi)\nabla\varphi$ in the superconductor. We can write

$$\Phi = \oint \mathbf{A} \cdot ds = (\Phi_0/2\pi) \int_{\text{superconductor}} \nabla\varphi \cdot ds + \int_{\text{weak links}} \mathbf{A} \cdot ds \tag{28}$$

by separating into the superconducting loop and the weak links of the junctions. Here, $\Phi_0 = 2\pi\phi_0$ is the magnetic flux quantum. In order to maintain single-valuedness around the

contour, the value of the phase differences across the weak links $\Delta\varphi_i$ and the integral of $\nabla\varphi$ across the superconductor must be zero (modulo 2π). So,

$$\int_{\text{superconductor}} \nabla\varphi \cdot ds \equiv -\sum \Delta\varphi_i \mod 2\pi. \tag{29}$$

We can take the integral around the loop in two halves of the loop, one through one junction and one through the other. In this case, the sum of the phase differences as computed by these integrals around the loop in the same direction is $2\pi\Phi/\Phi_0$. We want to consider the sum of the phase differences in the same direction around the loop in order to compute the current flowing from one side of the loop to the other, and so we get $2\pi\Phi/\Phi_0 \mod 2\pi$. In other words, flux through the loop is quantized, and the maximum supported supercurrent of the combination of the two paths in parallel is less than the sum of the critical currents in the two paths, except when Φ is a multiple of Φ_0. When this happens, the two phase differences can simultaneously be $\pi/2$, supporting the maximum supercurrent. In the case of two identical junctions, we can write the maximum supported supercurrent as

$$I_{\text{m}} = 2I_c|\cos(\pi\Phi/\Phi_0)|. \tag{30}$$

The maximum supercurrent is twice the critical current of each junction with flux being an integer number of flux quanta, and is zero at half-integer values. In other words, the critical current is at a maximum when there are no screening currents in the SQUID, and is at a minimum when there are maximum screening currents in the SQUID. This relation of critical current to magnetic field provides utility in that we can measure magnetic flux to a fraction of Φ_0.

1.2 Modeling superconducting circuits with cQED techniques

In this Dissertation, we will frequently model systems which contain nonlinear superconducting elements. Circuit quantum electrodynamics, or cQED (which we do not use to refer to cavity QED here), is a framework for modeling such systems. In this Chapter, we will lay the groundwork for using circuit QED in later chapters, and we will start by considering the dynamics of an LC oscillator. We will follow the derivations laid out in Ref. [44][2].

We begin with an LC oscillator with inductance L and capacitance C, whose Lagrangian we write as

$$\mathcal{L} = \frac{1}{2}LI^2 - \frac{1}{2}\frac{q^2}{C}, \tag{31}$$

where I is the current through the circuit and q is the charge on the capacitor. Since $I = \dot{q}$ by charge conservation, we can write this as

$$\mathcal{L} = \frac{1}{2}L\dot{q}^2 - \frac{1}{2C}q^2. \tag{32}$$

This system is dynamically equivalent to a mass on a spring, where here the inductance L plays the role of the mass, and the inverse capacitance $1/C$ plays the role of the spring constant. The frequency of this oscillator is then $1/\sqrt{LC}$.

We can write the conjugate momentum for the charge coordinate in this system, which is the flux through the inductor

$$\Phi = \frac{\partial \mathcal{L}}{\partial \dot{q}} = L\dot{q} = LI. \tag{33}$$

We can then write the Hamiltonian of the system as

$$H = \Phi\dot{q} - \mathcal{L} = \frac{\Phi^2}{2L} + \frac{1}{2C}q^2. \tag{34}$$

[2] A review of key points is available at [12].

This Hamiltonian can be used to give the current through the inductor and the voltage across the inductor and capacitor, as follows:

$$\dot{q} = \frac{\partial H}{\partial \Phi} = \frac{\Phi}{L} = I, \tag{35}$$

$$\dot{\Phi} = -\frac{\partial H}{\partial q} = -\frac{q}{C} = V. \tag{36}$$

We can then write the coordinate q and its conjugate Φ as quantum operators with the commutation relation $[\hat{\Phi}, \hat{q}] = -i\hbar$ so that the Hamiltonian becomes

$$H = \hbar \frac{1}{\sqrt{LC}} \left(\hat{a}^\dagger \hat{a} + \frac{1}{2} \right), \tag{37}$$

with raising and lowering operators

$$\hat{a} = i \frac{1}{\sqrt{2L\hbar\sqrt{LC}}} \hat{\Phi} + \frac{1}{\sqrt{2C\hbar\sqrt{LC}}} \hat{q}, \tag{38}$$

$$\hat{a}^\dagger = -i \frac{1}{\sqrt{2L\hbar\sqrt{LC}}} \hat{\Phi} + \frac{1}{\sqrt{2C\hbar\sqrt{LC}}} \hat{q}, \tag{39}$$

giving the usual form of the quantum harmonic oscillator.

To this point, we have taken the picture that the kinetic energy term of the system is the inductive term, as L is equivalent to a mass, and similarly the capacitive term is the potential energy term. However, we aim to use this formalism to model circuits which include Josephson junctions, which act as nonlinear inductors. Thus, it is ideal to consider the inductive elements as contributing to the potential energy of the system. To do this, we can define the dimensionless node flux (i.e. the superconducting phase) at a point in the circuit as

$$\varphi(t) = \frac{1}{\phi_0} \int_{-\infty}^{t} d\tau V(\tau), \tag{40}$$

which then gives $V(t) = \phi_0 \dot{\varphi}$. This is equivalent to the Josephson relation given in Eq. 27. The capacitive term then becomes

$$\frac{1}{2} C \phi_0^2 \dot{\varphi}^2, \tag{41}$$

which has the form of a kinetic energy. We also have $V = L\dot{I} = \phi_0\dot{\varphi}$, so the inductive term becomes

$$\frac{\phi_0^2}{2L}\varphi^2, \tag{42}$$

which has the form of a potential energy in φ. Now, the Lagrangian of the system is

$$\mathcal{L} = \frac{1}{2}C\phi_0^2\dot{\varphi}^2 - \frac{\phi_0^2}{2L}\varphi^2. \tag{43}$$

We can take the conjugate momentum of the new φ coordinate,

$$Q = \frac{\partial \mathcal{L}}{\partial \dot{\varphi}} = C\phi_0^2\dot{\varphi}. \tag{44}$$

This formalism becomes extremely powerful for modeling nonlinear elements such as Josephson junctions, which have sinusoidal current-phase relations. Many nonlinear devices with applications in quantum computing can be modeled with these techniques, such as the RF-SQUID which we model in Chapter 4, where we derive equations of motion based on Lagrangian mechanics starting from cQED. We then extend this method to model nonlinear superconducting circuits of arbitrary forms. In Chapter 5, we model the transmon qubit and SNAIL devices by writing their Hamiltonians with cQED methods and apply Schrödinger's equation to find eigenstates of each.

It is also important to note that this formalism is relevant to systems which are coupled to a transmission line. A transmission line which is infinite or semi-infinite in fact can act resistively even if it is composed of only reactive elements. This is because energy can propagate down the transmission line and never return. Therefore, a transmission line can have an effective impedance Z, and coupling to a transmission line makes for an open quantum system. We will model the transmission line as having a certain capacitance and inductance per unit length, and define node fluxes along the transmission line so we can model it with the cQED techniques outlined here. We will then see in Sec. 4.2.1 how this gives rise to a characteristic impedance and allows us to write input-output relations for systems coupled to the transmission line.

2.0 Engineering flat bands in graphene using doubly-periodic electrostatic gating

2.1 Introduction

Graphene has been found to exhibit numerous interesting and useful properties. It is a two-dimensional material and a semimetal with zero-gap due to Dirac points in its band structure, as first observed by Novoselov and co-workers [113, 77, 76, 78, 42]. In 2007, dos Santos and co-workers considered the effects of a small twist angle in bilayer graphene, using an effective model to find that the velocity near the Dirac points is reduced [69]. This was further investigated when a tight-binding model also indicated the presence of flat bands [105]. In 2011, Bistritzer and MacDonald found, using a continuum model, that at discrete magic angles, the Dirac velocity approaches zero [11]. More recently, the experimental discovery of superconductivity and correlated insulator phases in twisted bilayer graphene (TBG) near the magic angle [16, 15, 70, 106, 119] has prompted interest in properties which can be induced in graphene, a field that has been named twistronics [17]. This magic angle, at approximately 1.1°, is where band flattening occurs near zero energy. It has since been shown that this band flattening is a fundamental feature of the magic angle [107], which raises the question of the role of flat bands in the phenomena seen with magic angle TBG (MATBG).

It has previously been predicted that applying a potential with periodicity in one direction to graphene would induce band flattening in one direction [82, 117]. More recently, this asymmetric band flattening was realized experimentally in graphene [32, 61]. In particular, it has been shown that band flattening can be induced, for instance, in the k_x direction alone by applying a square wave potential along the y spatial direction. Electrostatic gating of graphene with doubly-periodic potentials, i.e. 2D potentials with periodic structure in two different directions, like triangular and square lattices, has also been considered in the past [88]. Indeed, it has been observed that lithographically defined gates can modify the electronic band structure [83, 38]. Here, inspired by the possibility of using conductive AFM-lithography [51, 53] or ultra-low-voltage electron-beam lithography [118] to define arbi-

trary shaped electrostatic gates at complex-oxide interfaces, we ask whether doubly periodic potentials applied to monolayer graphene can induce symmetric band flattening as seen in twisted bilayer graphene.

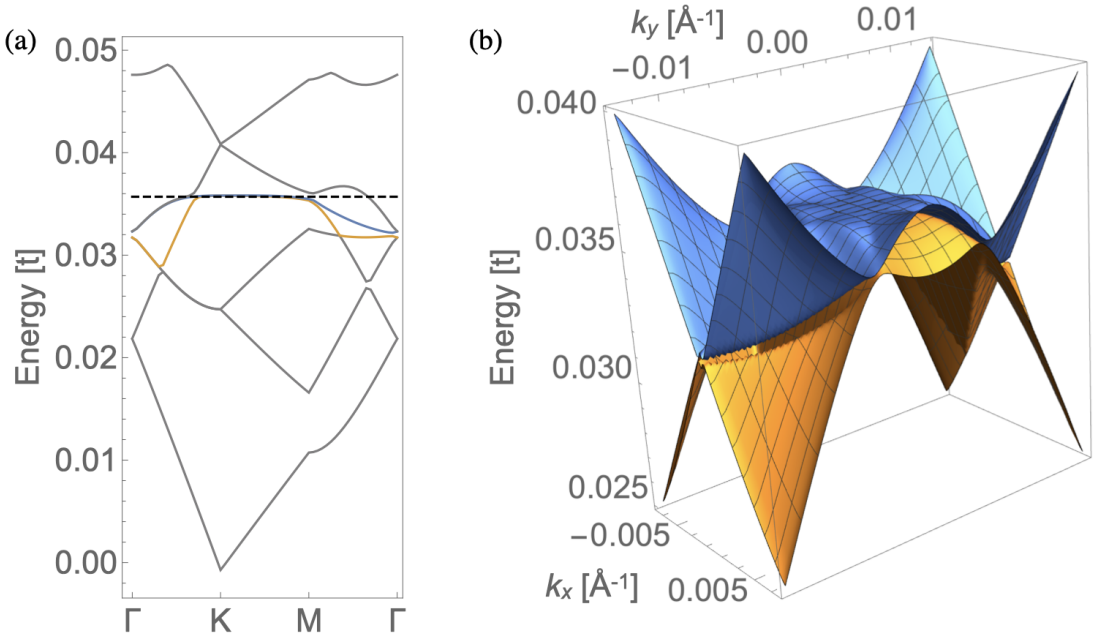

Figure 3: Isotropic band flattening induced by Kagome potential. The figure depicts two bands in the Brillouin zone of the superlattice (applied potential) obtained with the continuum model of gated monolayer graphene. At the point $k_x = k_y = 0$, which corresponds to the location of the Dirac point in the ungated model, the Fermi velocity as well as the band curvature are both essentially zero. In part (a), the black line indicates a constant energy, demonstrating the flat nature of the highlighted bands. Part (b) shows the highlighted bands in both k_x and k_y.

We investigate the band structure of monolayer graphene gated by doubly periodic electrical potentials. In searching for band flattening, we consider three kinds of applied potentials: checkerboard, hexagonal, and Kagome lattice. Consistent with previous work [83, 38], we find that the checkerboard potential can affect the Fermi velocity at the Dirac point, but we do not find strong examples of band flattening among energy bands near zero energy. Next, we consider two members of the wallpaper group 17, which has the same symmetries as those

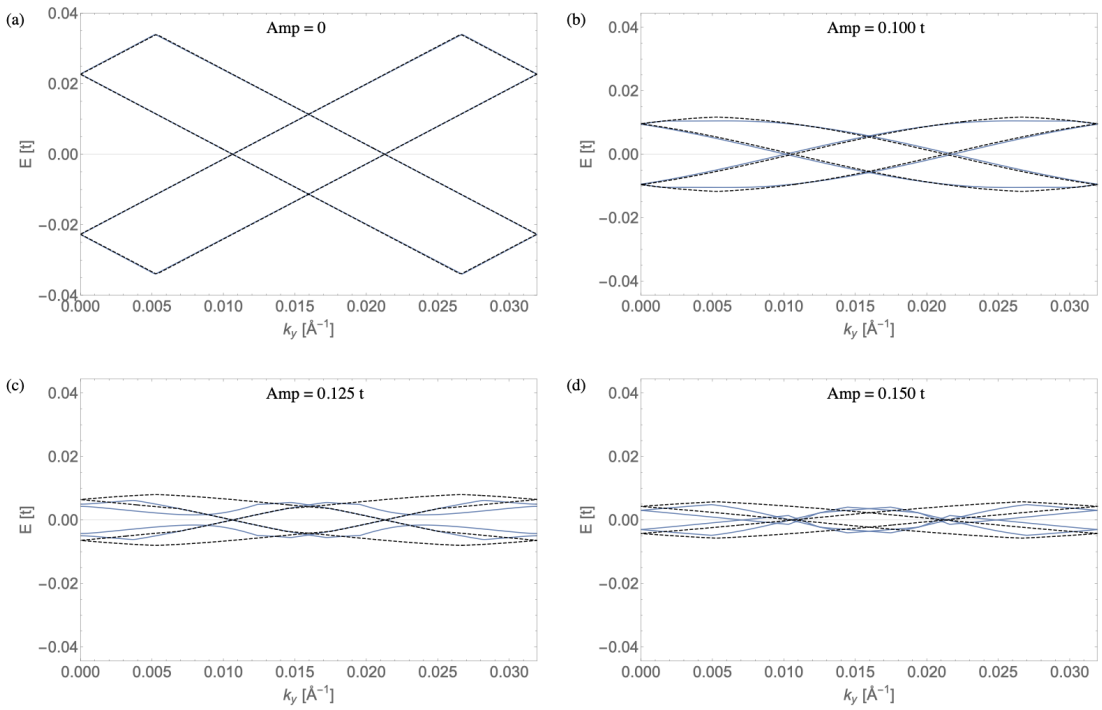

Figure 4: Tight-binding (solid blue) and continuum (dashed black) band structures for a checkerboard potential with periodicity of 204Å $\times$ 197Å, or 48×80 unit cells. (a) shows the case for amplitude of $0.000t$, (b) shows $0.100t$, (c) shows $0.125t$, and (d) shows $0.150t$.

of both monolayer graphene as well as TBG [125]. For the case of a sinusoidal hexagonal potential, we are able to find gating voltages for which this potential induces strongly flattened bands. For the case of the Kagome potential, we find even stronger band flattening, with both the Fermi velocity and band curvature very close to zero in the vicinity of the Dirac point as shown in Figure 3. We also investigate a potential with symmetries of wallpaper group 15, the results of which can be found in appendix 2.6.2.

In our investigation we use both a tight-binding and a continuum model of gated graphene, as in references [75, 20]. These two models agree well within certain ranges of parameters. However, as the gating voltage is increased, the continuum model becomes less applicable as effects of the graphene lattice which cannot be described by physics near the Dirac cone alone become relevant. The tight-binding model considers these effects, but for lattices with larger

periodicity we run into the limits of our computational resources. Further, the tight-binding model has its own pathologies associated with the comensurability of the applied potential lattice and the underlying graphene lattice that is necessary for numerical analysis, which are addressed in appendix 2.6.1. An example of the divergence of the two models can be seen in Figure 4. In this figure, we plot the band structure computed using both models for a checkerboard potential and find that for low amplitudes, the models agree well. However, as the amplitude of the potential increases, the band structure obtained from each model differs more significantly. Therefore, in order to find the most robust band flattening scenario, we specifically look for band flattening that occurs in both the tight-binding and the continuum model at the same time.

Having an experimental knob for tuning band flatness, we propose an experimental investigation of whether band flattening is sufficient to reproduce the properties of MATBG with the use of only a single layer of graphene. This approach would help to experimentally disentangle whether flat bands are the fundamental characteristic that induces correlated insulator and superconducting phases in these systems or whether additional features [3] such as fragile topology [91, 90] are required.

In addition to the search for behavior similar to that of MATBG, our work points to the possibility for band engineering. Our models provide a predictive guide in determining the behavior of electronic band structure under different potentials. By modeling the results of the interplay of the applied potential and the intrinsic electronic properties of graphene, we make strides toward turning graphene into a metamaterial with fine control of velocity near the Dirac point [38, 100]. We expect that continuous tuning of band flatness by electrostatic gating could be a powerful tool for probing fundamental physics of strongly correlated systems. Specifically, band flattening quenches the kinetic energy relative to the interaction energy, thus pushing graphene into the strongly interacting regime. Band structure engineering could also have potential applications in optics and electronics [25].

In this Chapter, we will discuss the model and results from our paper, which is available on the arXiv [49].

2.2 Tight-Binding Model

Tight-binding calculations used here consider the hopping of electrons between neighboring carbon atoms allowing us to derive the electronic band structure of the gated graphene lattice. Our tight-binding Hamiltonian consists of a hopping term that couples neighboring lattice sites and an on-site potential term that describes the action of an electrostatic gate. Here, we consider the nonmagnetic case and hence focus on only one spin species as we expect both to have an identical band structure. Therefore, the Hamiltonian is of the form

$$H = -t\Sigma_{i,j}(c_i^\dagger c_j + \text{h.c.}) + \Sigma_i c_i^\dagger c_i V(\mathbf{r_i}), \tag{45}$$

where i, j index the lattice sites of the honeycomb lattice, $c_i, c_i^\dagger$ are the annihilation and creation operators on site i, t is the hopping term between lattice sites, and $V(\mathbf{r_i})$ is the applied potential at position $\mathbf{r_i}$, or the position of the site i.

We implement this Hamiltonian in Mathematica by writing a matrix which couples neighboring lattice sites with the strength t, where in this matrix the row and column indices represent lattice sites. Then, the diagonal of this square matrix will represent the strength of the potential at each lattice site. The electronic band structure can then be solved by using Mathematica's Eigensystem[] solver, evaluating the allowed energies at each value of $\mathbf{k}$.

However, in order to investigate this model in a computationally tractable way, we must apply some constraints to the choice of potential $V(\mathbf{r})$. The potential must be periodic in both spatial directions in such a way that the graphene lattice can be specified to have the same period in such directions, thus resulting in an extended unit cell that can be specified with finite computational resources. That is, the period of the potential in x and y directions must be an integer multiple of the size of a graphene unit cell. In the armchair configuration of the graphene unit cell as used in this simulation, the size of each cell is $3a \times \sqrt{3}a$, where a is the distance between lattice sites. Only certain potentials at certain orientations relative to the graphene lattice are able to be made compatible with the integer unit cell requirement.

In particular, a square potential cannot be perfectly simulated by this tight-binding method due to the fact that it is not possible to find four points in a hexagonal lattice which

form a square. Therefore, for our checkerboard potential, we use a rectangular potential by choosing the period in each direction to be an arbitrary integer multiple of the size of the graphene unit cell. Hexagonal lattices are possible as the graphene lattice itself is hexagonal in nature, however only certain angles of the potential relative to the graphene are possible. These commensurate angles are further classified into type-I and type-II, which are considered for Moiré lattices in twisted bilayer graphene by Zou and colleagues [125] and are extended here for hexagonal potentials applied to graphene. Type-I lattices are manifested in this simulation by those angles wherein the extended unit cell contains three vertical periods of the potential, whereas Type-II lattices are represented by extended unit cells containing a single period of the potential. Due to phenomena associated with band folding in the tight-binding model, type-I hexagonal lattices are not considered (see appendix 2.6.1).

2.3 Continuum Model

We begin with the effective two-band low-energy Hamiltonian near the K points. In particular, we consider the Hamiltonian of the form

$$H = \begin{pmatrix} -iv_0\boldsymbol{\sigma}\nabla & V(\mathbf{r}) \\ V(\mathbf{r}) & -iv_0\boldsymbol{\sigma}\nabla \end{pmatrix} \tag{46}$$

where v_0 represents the Fermi velocity in graphene, $\boldsymbol{\sigma}$ is the Pauli matrix vector, $\nabla = (\partial_x, \partial_y)$, and $V(\mathbf{r})$ represents the applied potential over the graphene lattice. We write the real-space wave function as in reference [107] in terms of the momentum components, $a_{\sigma,ij}(\mathbf{k})$, as

$$\psi_{\mathbf{k}}(\mathbf{r}) = \Sigma_{i,j} \begin{pmatrix} a_{1,ij}(\mathbf{k}) \\ a_{2,ij}(\mathbf{k}) \end{pmatrix} e^{i(\mathbf{K_{ij}}+\mathbf{k})\mathbf{r}}, \tag{47}$$

where $\mathbf{K_{ij}} = i\mathbf{b_1} + j\mathbf{b_2}$ and $\mathbf{b_1}, \mathbf{b_2}$ are the reciprocal lattice vectors of the extended unit cell of the periodic potential.

We wish to write the Hamiltonian in momentum space, and since the Hamiltonian is periodic in real space, the lattice momentum, which is set by the period of the potential, is a good quantum number. Therefore, the momentum space Hamiltonian is

$$H = \begin{pmatrix} 0 & k_x - ik_y & F_{01} & 0 & \dots \\ k_x + ik_y & 0 & 0 & F_{01} & \dots \\ F_{10} & 0 & 0 & k_x + K_{10,x} - i(k_y + K_{10,y}) & \dots \\ 0 & F_{10} & k_x + K_{10,x} + i(k_y + K_{10,y}) & 0 & \dots \\ \vdots & \vdots & \vdots & \vdots & \ddots \end{pmatrix} \tag{48}$$

where the diagonal 2×2 blocks correspond to the kinetic energy shifted by lattice momentum $\mathbf{K}_{ij}$, while the off-diagonal 2×2 blocks at position $(i_1, j_1)(i_2, j_2)$ correspond to the Fourier transform of the potential energy with the coefficient $F_{(i_2-i_1)(j_2-j_1)}$ where the momentum transfer is $\mathbf{K}_{(i_2-i_1)(j_2-j_1)}$. We write this Hamiltonian as a matrix in Mathematica, and when we perform the numerics, we truncate the Hamiltonian matrix by enforcing $-n \leq i \leq n$ and $-n \leq j \leq n$, and choosing n sufficiently large to ensure the convergence of the bands that we are interested in.

The continuum model is only valid over a range of parameters for which effects far from the Dirac point are negligible, i.e. for momentum close to the Dirac cone center. As the amplitude of the applied potential increases, Eq. (2.3) indicates that scattering between farther away k points becomes more important, and the linear dispersion assumption of the continuum model breaks down. Consequently, the continuum model diverges from the tight-binding model and hence the true behavior of graphene. In particular, the model functions best for potentials with amplitudes less than $\approx 0.1t$, where t is the hopping term between lattice sites, and this term is given by $t = 2\hbar v_0/3a$. In order to gauge the the deviation between the two models, we consider the normalized mean error between the central bands as computed by the two models along k_y, averaged over one Brillouin zone

$$\Delta = \frac{\int_0^{2\pi/a} dk_y |\epsilon^{\mathrm{TB}}_{k_x=0,k_y} - \epsilon^{\mathrm{cont}}_{1,k_x=0,k_y}|}{\int_0^{2\pi/a} dk_y \epsilon^{\mathrm{TB}}_{1,k_x=0,k_y}}. \tag{49}$$

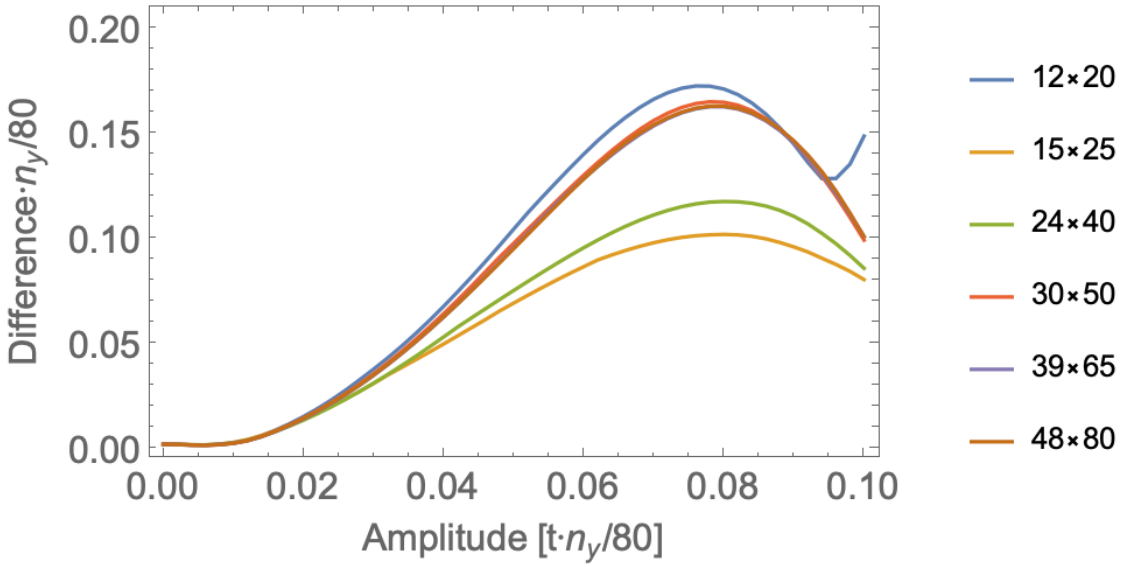

Figure 5: Divergence of tight-binding and continuum models as amplitude of the checkerboard potential is increased. Each curve plots the difference between the two models for a different extended unit cell size. The differences and amplitudes here have been scaled by $n_y/80$, where n_y is the number of graphene unit cells along the y direction in the extended unit cell.

In Figure 5, we plot the difference Δ scaled by $n_y/80$ as a function of the amplitude of the checkerboard potential also scaled by $n_y/80$ for various extended unit cell sizes $n_x \times n_y$. We observe reasonable collapse of the numerical data, indicating that regardless of extended unit cell size, the models diverge at roughly the same rate as amplitude is increased.

2.4 Exploration of electrostatic potentials

We find instances of band flattening which show promise of being experimentally reproducible, with verification of band flattening in both tight-binding and continuum model calculations and for various gating potentials. We use our continuum model to numerically com-

pute band structure and identify band flattening near high-symmetry points ($k_x = 0, k_y = 0$) over regimes spanning a range of amplitudes. We then compute the second derivatives of these bands in order to identify a gating strength with optimal flattening. The tight-binding model provides an additional check on these calculations to ensure we are operating within the applicable regime of parameters of the continuum model. We consider here the results from a checkerboard potential, a sinusoidal hexagonal potential, and a Kagome potential.

In addition to these useful regimes of band flattening, the tight-binding model implies instances of band flattening which occur at very precisely tuned values of applied amplitude, in particular at points wherein the observed Dirac point splits into further Dirac points. However, we note that these cases of band flattening are likely difficult to reproduce experimentally as variations of the extended unit cell size by a single graphene cell will destabilize the flat point. This indicates that experimental realization of checkerboard-based band flattening requires sub-nanometer control of the applied potential as well as fine tuning of the potential amplitude. While these phenomena exist in principle, they do not provide a strong basis for demonstrating flat bands in a lab. See appendix 2.6.1 for more.

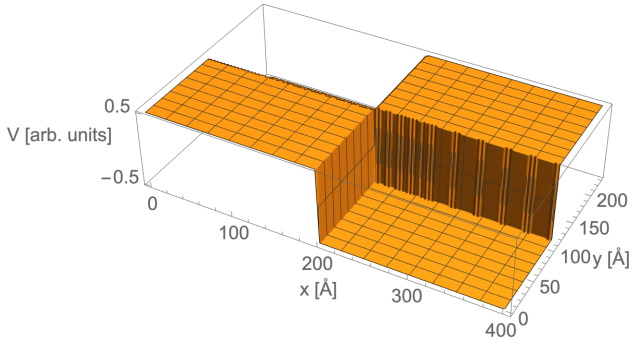

Figure 6: Single extended unit cell of a checkerboard potential with different periodicity in each direction. This potential is used to produce the results in Figure 7, parts (a) and (d).

2.4.1 Checkerboard Potential

The checkerboard potential, a member of wallpaper group 11 (p4mm), pictured in Figure 6, is used as an extension of the 1D case of a square potential as investigated by Li and

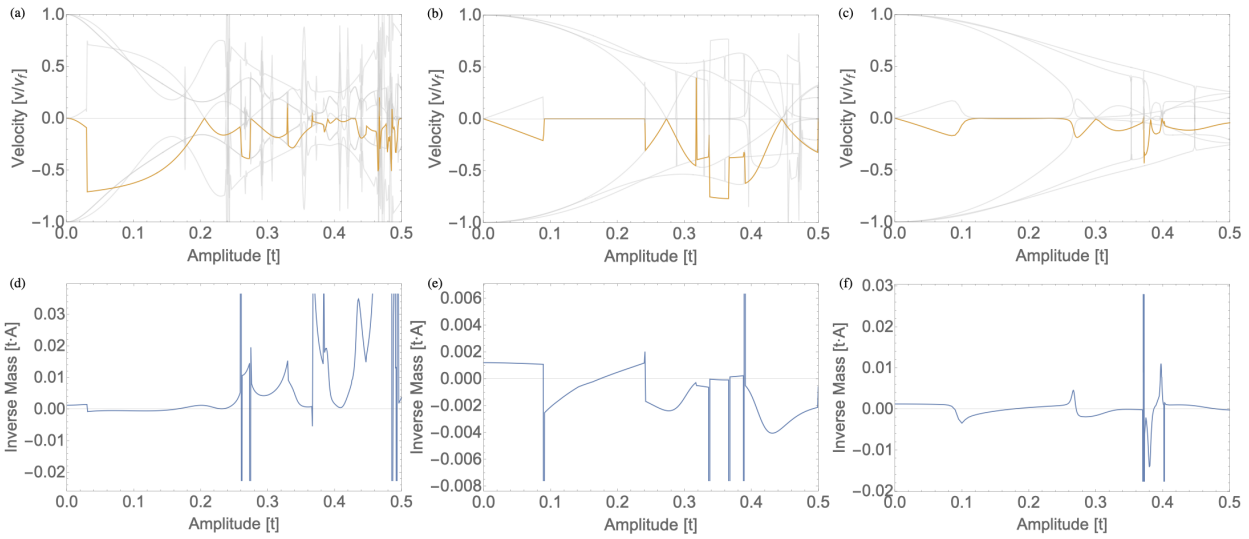

Figure 7: Numerically computed derivatives of the energy bands from the continuum model near Brillouin zone center versus applied potential amplitude. (a),(b), and (c) show a selection of first derivatives for energy bands near the zero energy for the checkerboard, sinusoidal hexagonal, and Kagome potentials, respectively. In each, one energy band is highlighted in orange. (d), (e), and (f) show the second derivative of the energy band whose first derivative is highlighted in (a),(b), and(c), respectively. The amplitude is measured in units of t, the velocity is measured relative to the Fermi velocity of electrons in graphene, v_f, and the inverse mass is measured in units of $t \cdot A$, where A is the extended unit cell area.

colleagues [61], as it is composed of square waves along the x and y directions independently. It is of the form

$$V(x, y) = V_0 \left(\text{IF}((x, y) \in \text{High}, 0.5, -0.5)\right),$$

where V_0 is the amplitude of the potential, the IF function returns the second argument if the first is true and the third argument otherwise, and the set "High" refers to the set of points (x, y) that lie within a tile in the checkerboard with the higher potential. We apply this potential such that the periodicity in each direction is different because of the required periodicity imposed by the graphene lattice. That is, the tight-binding model requires that

an extended unit cell be specified which is doubly periodic, and therefore takes into account the periodicity of both the graphene and the applied potential in both directions. However, the hexagonal lattice of the graphene is not commensurate with a square lattice, and it is not possible to choose 4 graphene sites in a honeycomb lattice such that they form a square. Therefore, the tight-binding model can only provide results for a rectangular potential, where the square potential is slightly stretched to fit the chosen dimensions of the extended unit cell in the model.

In Figure 4, we plot the electronic band structures computed by the tight-binding model and the continuum model at select amplitudes of the checkerboard potential. We observe that both models show band flattening over the range of amplitudes chosen, as the energy levels of the plotted bands decrease toward zero. Additionally, as amplitude is increased, the models begin to disagree.

In Figure 7, we see plotted the derivatives of several energy bands near zero energy over a range of amplitudes for a checkerboard potential with periodicity of 94 graphene unit cells in each direction ($400\text{Å} \times 231\text{Å}$). This checkerboard potential case demonstrates the least band flattening compared to other potentials investigated here, with few regions of amplitude over which any band near the central bands are flattened. That is, band flattening to a velocity of zero occurs only at finely tuned values of gating strength rather than over larger amplitude ranges. This is the case for amplitudes up to half of the coupling energy and for bands near zero energy. Because of this, we do not identify any applied amplitudes wherein the first and second derivatives of the energy bands near the Dirac points are simultaneously nearly zero. Therefore, we do not find the checkerboard potential to be useful in attaining flat bands in graphene for relevant applied potential strengths.

2.4.2 Sinusoidal Hexagonal Potential

This potential, which is a member of wallpaper group 17 (p6mm) and which can be expressed without rotation as

$$V(x,y) = \frac{V_0}{4}\left(\cos\left(\frac{2y}{\sqrt{3}}\right) + \cos\left(\frac{y}{\sqrt{3}} + x\right) + \cos\left(\frac{y}{\sqrt{3}} - x\right)\right),$$

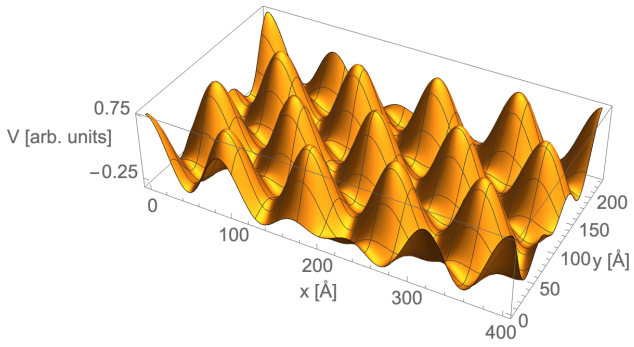

Figure 8: Single extended unit cell of the sinusoidal hexagonal potential with rotation of approximately 10.9° relative to the graphene lattice. This potential is used to produce the results in Figure 7, parts (b) and (e).

where V_0 is the amplitude of the potential, is commensurate with the graphene lattice due to its hexagonal nature, and thus is replicable in the tight-binding model. For example, see Figure 8, which shows a sinusoidal hexagonal potential that is rotated by 10.9° so as to be commensurate with the underlying graphene lattice. In this example, which shows the same potential as used for the simulations in Figure 7, the extended unit cell is composed of 94×94 graphene unit cells, resulting in a size of 400Å $\times$ 231Å. However, the distance between adjacent potential maxima is only 87Å. The extended unit cell size is chosen so as to maintain the required double-periodicity, accounting for both the potential and the graphene lattice.

For this potential, we find that certain bands are flattened for a range of applied gating voltages, as shown in Figure 7. We are able to identify at least one point where both the first and second derivative of one band are simultaneously nearly zero, as highlighted in parts (b) and (e) of the figure. We also identify further points at which the Fermi velocity becomes small for finely tuned values of the applied gating voltage. Therefore, a hexagonal potential is a reasonable choice for exploring phenomena expected of flat bands. In particular, for 400Å $\times$ 231Å extended unit cell size the amplitude of the applied potential should be $0.45t$. If we scale the size of the extended unit cell, while keeping its aspect ratio fixed (i.e.

$L_x/L_y = 400/231$), then the amplitude of the applied potential needed to obtain flat bands scales as $(400\text{Å}/L_x) * (0.45t)$.

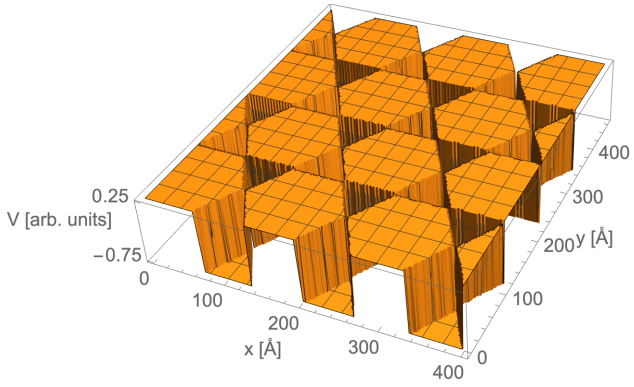

Figure 9: Kagome potential used in this simulation. Here, we plot two copies of the extended unit cell in the y direction, and one copy in the x direction. This potential is used to produce the results in Figure 7, parts (c) and (f).

2.4.3 Kagome Potential

The Kagome potential has a hexagonal lattice and can therefore be represented with tight-binding calculations in a way which is commensurate with the underlying graphene lattice. This potential is a member of wallpaper group 17 (p6mm), which represents the same symmetries as twisted bilayer graphene. Here, we consider a uniform 2-coloring of the Kagome lattice as pictured in Figure 9. In particular, the potential is of the form

$$V(x, y) = V_0 \left(\text{IF}((x, y) \in \text{Hexagon}, 0.25, -0.75)\right),$$

where V_0 is the amplitude of the potential, the IF function returns the second argument if the first is true and the third argument otherwise, and the set "Hexagon" refers to the set of points (x, y) that lie within a hexagonal tile in the Kagome potential. The hexagons are assigned a potential of 0.25 and the triangles a potential of -0.75 in order to set the average potential to be 0.

We show in part (c) of Figure 7 the first derivatives of bands calculated using the continuum model for this potential. We observe significant ranges of applied voltage where bands near zero energy have nearly zero velocity. At the same time, we are able to identify points where the second derivative of a band is zero and coincides with zero velocity, as highlighted in part (f) of the figure. The wide range of amplitudes for which the Kagome potential exhibits flat bands indicates that this potential is the most promising for producing the desired flat band effects in practice, particularly near an applied potential amplitude of $0.177t$. Although it is tempting to ascribe the presence of these flat bands to the effects of a Kagome lattice of sites as found by Bergman and colleagues in [10], we do not expect this is the case as we observe a pair of flat bands in our region of interest rather than a single band as predicted by Bergman's Kagome lattice model.

2.5 Summary

We have shown that it is possible to induce band flattening in gated graphene through the application of doubly periodic potentials. We have also identified a range of potential amplitudes over which this is possible, and our results indicate that the Kagome potential shows the most robust band flattening. In particular, a Kagome potential with spacing between hexagon centers of, for instance, 11.6 nm requires a gating potential of 5.5 eV to get flat bands, while one with 50 nm spacing requires 1.3 eV (where we use $v_f \approx 10^6$ m/s [20]). Electronically reprogrammable complex oxide heterostructures, in particular $LaAlO_3/SrTiO_3$ interfaces [22], can potentially be used to produce these doubly periodic potentials. Graphene/$LaAlO_3/SrTiO_3$ heterostructures can be programmed using conductive atomic force microscope (c-AFM) lithography [51, 53]; however, this technique is not amenable to van der Waals stacks containing hexagonal boron nitride. A more recently developed approach, which uses ultra-low-voltage electron beam lithography (ULV-EBL) to achieve nanoscale control of the metal insulator transition at buried $LaAlO_3/SrTiO_3$ interfaces [118], can realize sub-10-nm resolution conductive nanostructures that are reprogrammable, and thus provide a pathway toward a more general approach to analog quantum

simulation. The theoretical results described here offer guidance and insight into the families of doubly periodic potentials that are likely to induce strong electron-electron interactions due to ultraflat electronic dispersion.

2.6 Appendix

2.6.1 Pathologies of the tight-binding model

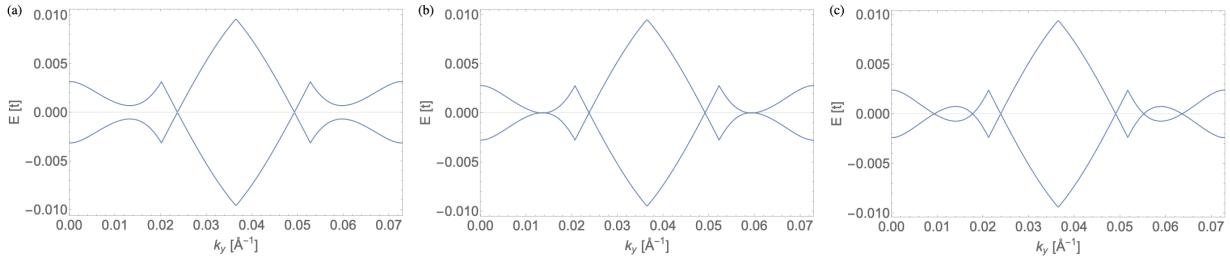

Figure 10: Band structure for checkerboard potential with extended unit cell size 85Å$\times$86Å, or 20×35 graphene unit cells. In (a), the potential has an amplitude of $0.2850t$, and the central bands approach each other with a point of minimum separation at $k_y =$ and $k_y =$. In (b), at an amplitude of $0.2874t$, the two bands touch and form a flat region at $k_y =$ and $k_y =$. In (c), with a potential amplitude of $0.2900t$, the flat region has split into two distinct Dirac points.

Due to the discrete nature of the tight-binding model and its underlying lattice, we note that the model predicts various phenomena which one would not reasonably expect to be replicable in a laboratory setting. There are two important classes of such spurious phenomena. The first is band flattening which occurs only at precise, finely tuned values of the applied potential. We observe this at transitionary points where the band touching point metamorphoses into a pair of Dirac points as the amplitude is tuned. The second occurs when the number of simulated graphene cells in the vertical direction, i.e. the direction in which the graphene unit cell has length $\sqrt{3}a$, is a multiple of 3. In this case, band folding

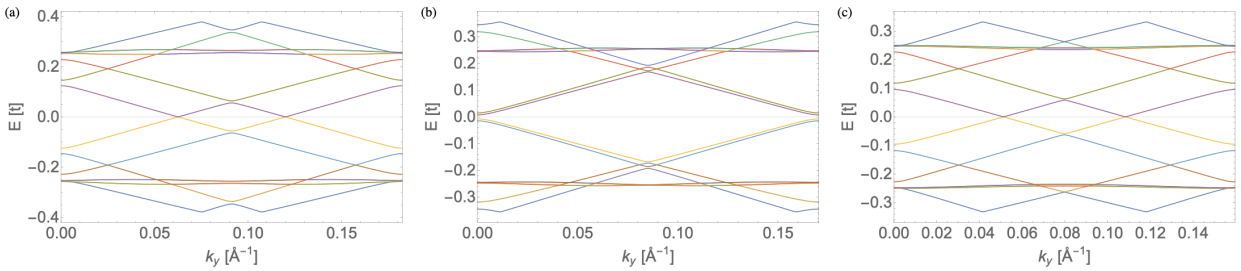

Figure 11: Example of band folding effects at certain unit cell sizes for a 1D square wave which is periodic along the y direction. In (a), we have a 10×14 unit cell potential, in (b), a 10×15 unit cell potential, and in (c), a 10×16 unit cell potential. All three have an applied potential of amplitude $0.3t$. The band folding in (b) produces an electronic band structure wherein the two Dirac points in the Brillouin zone are mapped to the same point, $(k_x, k_y) = (0, 0)$, so that the Dirac point is split. Due to the precise unit cell size needed to realize this, we expect that this effect is difficult to reproduce in a laboratory setting.

will perfectly map the two Dirac cones in a unit cell to the same point in the Brillouin zone associated with the potential, resulting in an electronic band structure that is very sensitive to the commensurability of the graphene and the electrostatic potential lattices.

Here, we note that our tight-binding model can demonstrate band flattening at finely tuned values of the potential which, while plausible in theory, are unlikely to be accessible via experiment. These occur as the amplitude is tuned such that two bands approach each other until they touch at a point, and then split into two Dirac points, as shown in Figure 10. This process can also happen in reverse order with amplitude tuning. Additionally, as the periodicity of the applied potential is varied by a single graphene unit cell (on the order of 5Å), the necessary applied amplitude to see band flattening varies significantly. Therefore, experimental realization of these modes of band flattening would require precise control of both the amplitude of the applied potential and the length scale over which the potential is applied. As demonstrated by Barbier and colleagues, a continuum model of graphene can predict the emergence of extra Dirac points at certain applied potential strengths in the case

of a one-dimensional potential [84, 81, 14, 6, 33]. However, these additional Dirac points are not analogous to the anomalous Dirac points we see in our tight-binding model. Rather, these Dirac points, which are predicted by a continuum model, are stable over a range of applied potential amplitudes. The anomalous Dirac points discussed here are predicted only by our tight-binding model for two-dimensional potentials and are not stable under changes to the applied potential.

Band folding effects are responsible for the second type of anomaly of the tight-binding model discussed here. This effect, which can be seen in Figure 11, occurs when the size of the chosen extended unit cell is such that the two distinct Dirac points are mapped to the same point in k-space. In particular, this occurs when the number of graphene unit cells in the super cell in the y direction is divisible by 3. This is because for a single graphene unit cell, Dirac points occur along the k_y direction at exactly thirds of the size of the Brillouin zone. Therefore, when the number of unit cells is such that the Brillouin zone is reduced by a factor divisible by 3, both of the Dirac points will all be mapped to the zone center. In practice, these effects are unlikely to be detectable experimentally as they require the precise alignment of the periodic potential to the graphene lattice with precision of better than one graphene lattice spacing. Consequently, we consider only cases where the period of the applied potential in the vertical direction is not precisely a multiple of three graphene unit cells.

This second effect prevents useful simulation of type-I hexagonal lattices, i.e. those where the chosen rectangle of lattice sites is such that the number of vertical graphene unit cells is a multiple of three. This limits the set of angles at which we can simulate hexagonal lattices to those for which a type-II lattice can be constructed.

2.6.2 Wallpaper group 15

In addition to the three potentials outlined above, we consider an additional gating potential which is a member of wallpaper group 15 (p3m1). This potential consists of a

3-coloring of a hexagonal lattice, with a potential expressed by

$$V(x,y) = V_0 \begin{cases} 0.5 & (x,y) \in \text{Hex1} \\ 0 & (x,y) \in \text{Hex2} \\ -0.5 & (x,y) \in \text{Hex3} \end{cases},$$

where "Hex1", "Hex2", and "Hex3" are the sets of points such that each set represents hexagons at one of the assigned potential levels. This regular coloring of a hexagonal grid is pictured in Figure 12. We find that this potential results in band flattening similar to that which is seen with the Kagome potential. These results, shown in Figure 13, demonstrate that we are able to find bands which exhibit flatness for a range of gating amplitudes for the wallpaper group 15 potential.

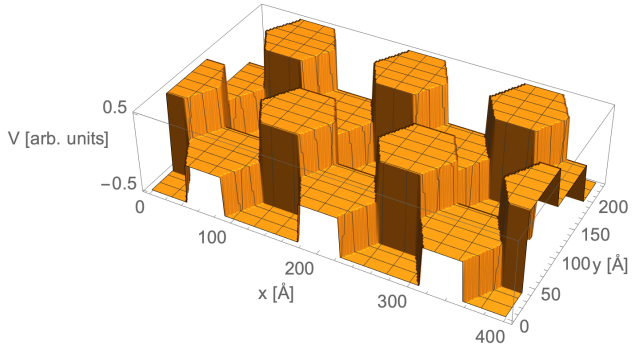

Figure 12: Single extended unit cell of a wallpaper group 15 potential. This potential is used to produce the results in Figure 13.

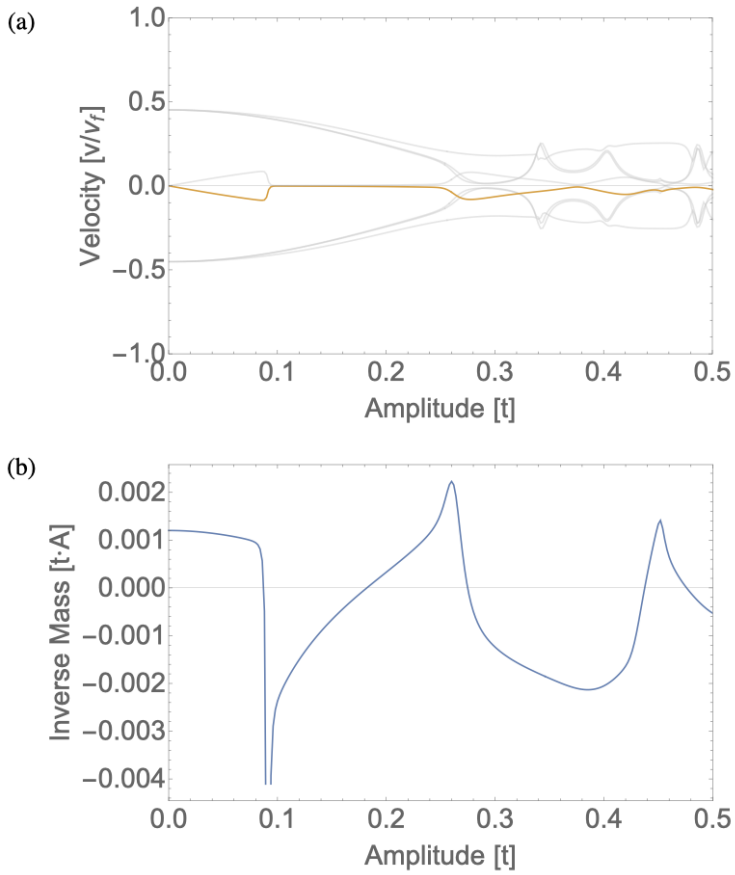

Figure 13: Numerically computed derivatives of the energy bands from the continuum model near Brillouin zone center versus applied potential amplitude for the wallpaper group 15 potential. (a) shows a selection of first derivatives for energy bands near zero energy. One energy band with a region of flatness over a range of amplitudes is highlighted in orange. (b) shows the second derivative of the highlighted energy band.

3.0 LAO/KTO DC-SQUID

3.1 Introduction

The platform of complex oxide heterointerfaces raises interest in the possibilities of designing superconducting devices with great precision. One such complex oxide, strontium titanate ($SrTiO_3$), or STO, was found to be superconducting in 1964, an early example of superconductivity identified in a semiconducting material [98]. Decades later, it was shown that a 2 dimensional electron gas (2DEG) forms at the interface of STO with lanthanum aluminate ($LaAlO_3$), or LAO [79]. This 2DEG becomes superconducting at low temperatures (100s of mK) with similar properties as in bulk STO [94, 41]. The LAO/STO interface has given rise to a technique for fabricating reconfigurable superconducting nanoscale devices called conductive atomic force microscope (c-AFM) lithography [22, 27].

In the c-AFM lithography technique, which is used by the LevyLab, a c-AFM tip with a positive applied voltage is used to induce the formation of a 2DEG between the two complex oxide layers. The formation of conducting regions at the interface can be reversed to form insulating regions by applying a negative c-AFM tip voltage. This allows us to implement arbitrary designs constructed from this 2D superconductor, with fine control over the geometries of the defined devices [23, 60]. However, previous attempts by the LevyLab to use this method to demonstrate the DC-SQUID effect have failed.

More recently, superconductivity has been discovered at the interface of LAO with potassium tantalate ($KTaO_3$), or KTO [66, 28]. Much like LAO/STO, the LAO/KTO interface has been introduced as a candidate for novel device manufacturing via c-AFM. However, there are various important material differences between KTO and STO. For instance, superconductivity has never been observed in bulk KTO [108], but rather only at interfaces, unlike STO. Specifically, at interfaces of LAO and KTO, the bulk of the oxides is not superconducting, but a 2DEG at the interface becomes a 2 dimensional superconductor. The critical temperature of superconductivity in these interfaces with KTO is, however, much higher than in STO interfaces, up to 2 K [66]. Also of note is that the critical temperature in

KTO interfaces depends on crystallographic orientation, suggesting that the pairing mechanism for superconductivity may be unconventional, i.e. a p-wave superconductor [67, 124].

In this chapter we analyze and model LAO/KTO DC-SQUID that have been investigated experimentally by the LevyLab. This is of particular interest since this is the first time that DC-SQUID effect has been observed in complex oxide heterointerface device made at the nanoscale by c-AFM. Previously, DC-SQUIDs have been made at the LAO/STO interface by conventional lithography [45], but all attempts to make one by c-AFM have, as far as we know, failed to work.

Using c-AFM lithography, the LevyLab manufactured two devices, SQUID A and SQUID B, by "sketching" weak links between bulk superconducting areas at the LAO/KTO interface with the geometry shown in Fig. 14. When measuring these DC-SQUIDs, the LevyLab found some peculiar properties, and that is how I became involved in the investigation. Based on the combined experimental and theory results, we wrote a joint paper (Ref. [120]) with the LevyLab in which I contributed the theoretical model. Next, I will set the stage by discussing the peculiar properties of LAO/KTO DC-SQUID devices. In the following sections, I will introduce a theoretical model for describing LAO/KTO nanodevices that explains the key experimental observations.

3.1.1 Device geometry and properties

SQUID A is composed of a square annular area where a 1.2 μm by 1.2 μm region was written via c-AFM. A square of size 0.4 μm by 0.4 μm in the center of the region is erased, forming the annulus. SQUID B is geometrically similar, but with outer dimensions of 1.02 μm by 1.02 μm and an inner hole measuring 0.34 μm by 0.34 μm. The annulus of each is split into two half-annuli by erasing a strip through the center of the square. Dayem bridge weak links are then written between the halves, forming the DC-SQUIDs. The corners of the SQUIDs are connected to leads which can be used for current-voltage measurements and for current sources to the device.

The LevyLab performed four-probe measurements of the differential resistance dV/dI of the SQUIDs for varying bias current and external magnetic field, which reveal properties

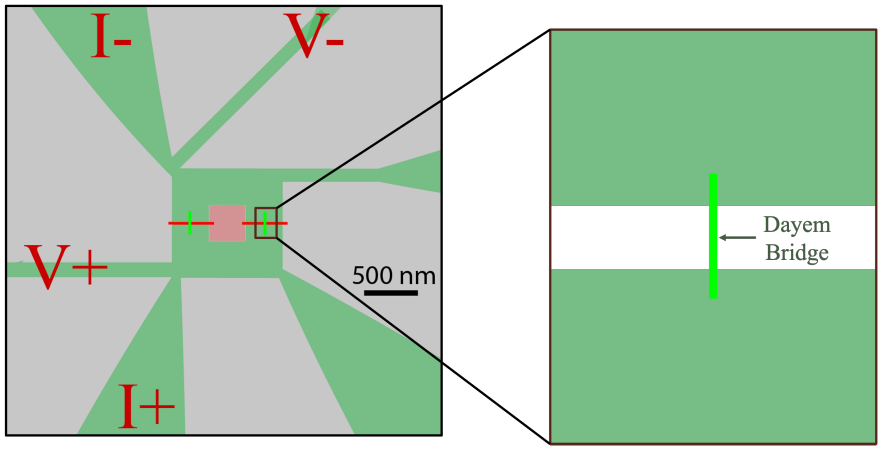

Figure 14: Geometry of the SQUIDs which are discussed in this Chapter. The green regions are those which are written with a c-AFM tip, and the red regions are erased. The light green lines represent the Dayem bridge weak links which function as the junctions in the SQUIDs. The right expanded view shows the Dayem bridge between the two half-annuli. The figure is adopted from Ref. [120].

of the devices' transitions between the superconducting and normal states. In Fig. 15, we see the results of this measurement for SQUID A. We see that the devices' resistance exhibits two transitions as current is increased, which we refer to as $I_{\mathrm{c,in}}$ and $I_{\mathrm{c,out}}$. We associate these transitions with the transitions of the Dayem bridges and of the half-annuli from superconducting to normal states, respectively. These critical currents demonstrate a few important properties. In particular, the inner critical current $I_{\mathrm{c,in}}$ exhibits periodic oscillations with applied magnetic field, and $I_{\mathrm{c,in}}$ for positive and negative currents are not in phase with each other. In the regime between the two critical currents, we see a periodic dependence of the resistivity of the material on B in both SQUIDs. This implies coherence around a contour which crosses the weak links and encircles the hole of the annulus, and so phase slips in the two bridges are correlated in this regime. $I_{\mathrm{c,out}}$, however, does not oscillate with B, which indicates that phase coherence is disrupted by fluctuation superconductivity.

In a conventional DC-SQUID, the critical current is a periodic function of the magnetic

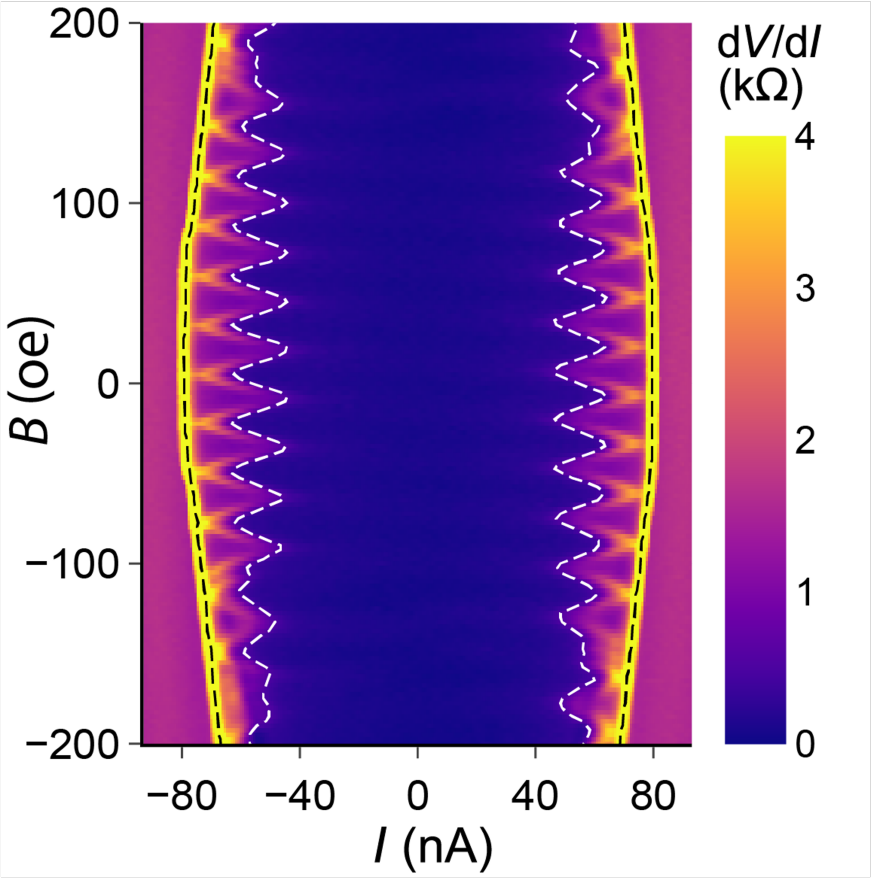

Figure 15: Device resistance versus external magnetic field and current through the device for SQUID A. The white dashed line represents $I_{\mathrm{c,in}}$ and the black dashed line represents $I_{\mathrm{c,out}}$. This measurement was performed at $T = 50$ mK. The figure is adopted from Ref. [120].

field, with the period ΔB set by the area A of the non-superconducting "hole" in the device

$$\Delta B = \Phi_0 / A, \tag{50}$$

where Φ_0 is the magnetic flux quantum. In SQUID A, the experimentally observed period of oscillation of $I_{\mathrm{c,in}}$ is $\Delta B = 2.74$ mT. Using Eq. (50), we can extract the effective area of the SQUID based on the observed period of oscillation. For SQUID A, the effective area of the hole is approximately 0.75 μm^2. This is significantly greater than the actual area of the

hole, which is only 0.16 μm^2. The situation in SQUID B is similar, with $\Delta B = 3.26$ mT, or an effective area of 0.63 μm^2, versus the actual area of 0.12 μm^2.

The comparison between the Pearl length in LAO/KTO and the SQUID size was an important clue for us in resolving the discrepancy between the actual and the effective area of the hole. The Pearl length is the characteristic length over which magnetic field is screened in thin film superconductors, and it is defined as $2\lambda_L^2/d$, where λ_L is the London penetration depth and d is the thickness of the film [87]. In the case of these devices, their size is significantly smaller than the Pearl length, and so magnetic fields penetrate them with very little attenuation.

This is very different from conventional DC-SQUIDs where magnetic field is almost completely expelled from the superconducting device by generated screening currents. In that case, as the magnetic flux through the hole is increased, it eventually reaches half a flux quantum, at which point the screening currents will prefer a flux of Φ_0. That is, the current through the device will reverse with period Φ_0, which can be exploited to create a magnetometer which converts flux to voltage with this same period. However, in the SQUIDs in this paper, the penetration of magnetic field into LAO/KTO devices means that the period of oscillation is significantly shorter since flux is not quantized, which is equivalent to a larger effective area. In this Chapter, we provide a model of this phenomenon which better explains the observed periodicity.

We also aim to explain other important properties of LAO/KTO SQUIDs and extract properties of superconductivity in LAO/KTO. Of note, the oscillations of the positive and negative inner critical currents, $I_{\mathrm{c,in}}$, are not in phase with each other. Moreover, the phase of these oscillations depends on the position of the leads that are used to source current through the SQUID. In order to explain this phenomenon, as well as derive important parameters of the SQUIDs, we couple our model of supercurrents in the devices to a Ginzburg-Landau model of the Dayem bridges as short superconducting nanowires. Among the parameters derived by this model is the kinetic inductance, which we find to be very high in this material.

In the remainder of this Chapter, we will describe our model of supercurrents in the SQUIDs given that they are penetrated by applied magnetic fields, and we will extract the periodicity of such a device's critical current with magnetic field. We will then introduce a

model of the Dayem bridges which link the two half-annuli, which are equivalent to short superconducting nanowires. We will then present results from fitting our experimental data to these models, including physical device parameters. Finally, we will provide details on the methods we used in coupling and fitting these two models.

3.2 Model of supercurrents coupled with Ginzburg-Landau weak bridges

Here we describe the theoretical model for the DC-SQUID which we use to understand the magnetic field period and to fit critical current oscillations and extract device parameters. We model the two half-annuli of the SQUID as uniform 2D superconductors. As the annuli are much smaller than the Pearl length, external magnetic fields penetrate them almost without attenuation. However, such fields generate screening currents and associated phase gradients. We model the two Dayem bridges as short superconducting nanowires. Oscillations of the device critical current with magnetic field result from phase quantization around a contour that encircles the inner square of the annulus, as opposed to magnetic flux quantization through the hole in a conventional SQUID described previously. We model the free energy in the KTO annulus due to the screening supercurrents, as shown in Sec. 1.1.2, as

$$F = \int \frac{1}{2m^*}|\Psi|^2|\hbar\nabla\varphi - \frac{e^*}{c}A|^2 dx^2, \tag{51}$$

where A is the magnetic vector potential, φ is the phase of the superconducting order parameter, $e^* = 2e, m^* = 2m$, and $|\Psi|^2 = n_s$, the superconducting electron density. We supplement this equation by Neumann boundary conditions which prevent supercurrents from leaving the annuli, except at the points where the leads and Dayem bridges are attached, where the boundary conditions specify the currents. An example of the resulting superconducting phase and supercurrents from this calculation are given in Fig. 16. We relate the current across the Dayem bridges to the phase differences that appear across the half-annuli using the current-phase relationship for short superconducting nanowires [63, 62, 89]. This current-phase relationship depends on the length of the Dayem bridge, exhibiting Josephson

junction-like behavior for short lengths and linear behavior for longer bridges, as observed in [48] and specified in Sec. 3.3.

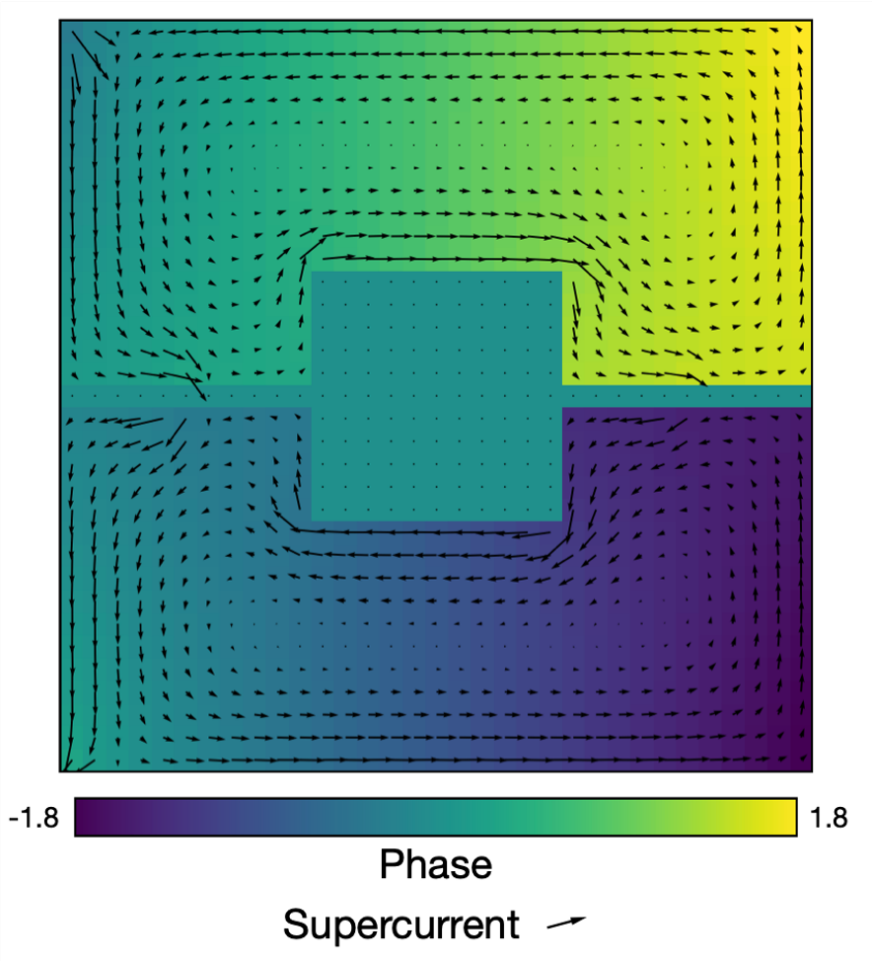

Figure 16: Map of supercurrents and phase differences across the half-annular regions.

We start by finding the magnetic field period by minimizing the free energy given by (51) and applying phase quantization around the annulus. Specifically, we run a successive over-relaxation algorithm (details in Appx. 3.5.1) on a grid representing the half-annuli with fixed critical currents for the Dayem bridges between them. Then, by computing the supercurrents and phase differences in the half-annuli for various input currents at the leads, we can determine the critical current of the device by when the critical current of either bridge is exceeded. We do this for a range of magnetic field values to determine the oscillation period of the critical currents. We also do this for different choices of fixed critical currents of the

bridges in order to match the phase offset between the positive and negative critical currents.

Table 1 compares the experimentally determined periodicity of critical current oscillations versus magnetic field to the estimated periodicity from our model of the superconducting half-annuli, as well as the naïve estimate from the area of the hole in the annulus. The naïve estimate exceeds the observed periodicity by a factor of roughly 4. Our model, which accounts for the penetration of the SQUID by external magnetic field and resulting phase variation across the annular regions of the device, determines this periodicity to within approximately 30% for SQUID A and 50% for SQUID B. We ascribe these discrepancies to the nonuniform superconductivity and imperfect knowledge of the device geometry resulting from the method in which the devices were fabricated. For example, some regions within the annulus of the SQUID are sketched twice, while other regions are sketched and then erased, which may result in spatial variations of the device's superconducting properties.

Periodicity of $I_{\mathrm{c,in}}$ vs B	SQUID A	SQUID B
Experiment	2.74 mT	3.26 dBm
Flux through hole	12.9 mT	17.9 mT
Our theory	3.59 mT	4.88 mT

Table 1: The period of $I_{\mathrm{c,in}}$ vs B oscillation of SQUIDs A and B (experiment), along with the naïve prediction from flux through hole, and the prediction from our theory.

In this paragraph, we describe how we fit out model parameters to the critical current oscillations in each SQUID, as in Fig. 17 and Fig. 18(i)-(l). For each device, we use our model of the half-annuli coupled to our model of the Dayem bridges to fit $I_{\mathrm{c,in}}(B)$ by setting the critical currents and lengths of the bridges as well as the superfluid density of the half-annuli. As we do not know how much magnetic flux is trapped in the external magnet that is used to apply magnetic field to the device, we also fit an overall magnetic field offset. This model replicates the size of $I_{\mathrm{c}+}$ and $I_{\mathrm{c}-}$ oscillations with magnetic field, as well as their mutual phase offset. In particular, we are able to adjust the bridge critical current and length in order to tune these characteristics. Additionally, we find that our model provides a range of values of superfluid density n_s which give physically similar results. That is, we

are able to reduce the superfluid density while maintaining nearly identical results down to a minimum density, at which point the model no longer finds agreement with the remaining fitting parameters. We are also able to extract the critical phase and kinetic inductance from the current-phase relationship which is fitted for each Dayem bridge. In Table 2, we provide the length, critical current, critical phase, and kinetic inductance of each bridge as determined by our model, as well as the minimum possible superfluid density for SQUID A with different applied backgate voltages. For the case of $V_{\mathrm{bg}} = 0$ V, we provide a plot of the $I_{\mathrm{c,in}}$ fit versus magnetic field in Fig. 17. Similarly, in Table 3 we provide these parameters for SQUID B with currents applied at different leads. We provide a fit in each case since we find that the critical current of the device, and consequently of its Dayem bridges, varies depending on the orientation of the leads with applied current. In Fig. 18, we provide the fits for each lead orientation to demonstrate the differences in each case.

SQUID A	$V_{\mathrm{bg}} = -80$ V	$V_{\mathrm{bg}} = 0$ V	$V_{\mathrm{bg}} = +70$ V
$l_{\mathrm{l}}/\xi_{\mathrm{GL}}$	6.0	6.0	6.0
$l_{\mathrm{r}}/\xi_{\mathrm{GL}}$	8.7	8.9	8.9
$I_{\mathrm{c,l}}$ (nA)	18.2	26.4	26.6
$I_{\mathrm{c,r}}$ (nA)	25.5	34.0	34.1
$\varphi_{\mathrm{c,l}}$ (rad)	3.50	3.50	3.39
$\varphi_{\mathrm{c,r}}$ (rad)	4.68	4.81	4.83
$L_{\mathrm{k,l}}$ (nH)	44.6	30.7	30.6
$L_{\mathrm{k,r}}$ (nH)	43.7	33.6	33.5
Min. annulus n_{s} (10^{11} cm^{-2})	8.6	14	14
$n_{\mathrm{s,l}}$ (10^{11} cm^{-2})	3.18	4.61	4.82
$n_{\mathrm{s,r}}$ (10^{11} cm^{-2})	4.82	6.44	6.41

Table 2: Length $l_{\mathrm{l(r)}}$, critical current $I_{\mathrm{c,l(r)}}$, critical phase $\varphi_{\mathrm{c,l(r)}}$, and kinetic inductance $L_{\mathrm{k,l(r)}}$, of each bridge in SQUID A, determined by theoretical fit. Minimum n_{s} in the annulus given by theory model, and n_{s} in the bridges calculated from I_{c}, are also listed. Different columns represent different backgate voltages applied.

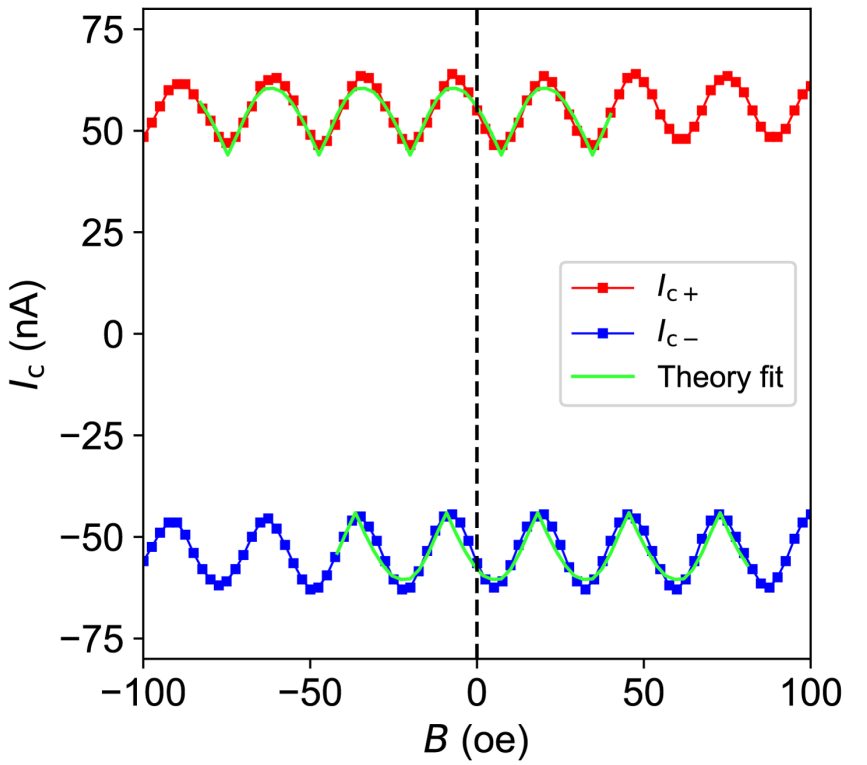

Figure 17: Fit of $I_{c,in}$ versus external magnetic field overlaid on data for SQUID A with $V_{bg} = 0$ V. The figure is adopted from Ref. [120].

As our Dayem bridges are equivalent to superconducting nanowires with width w, we can extract their superfluid density n_s from their critical currents I_c. In this calculation of n_s, we assume $w = 20$ nm, which is the resolution of c-AFM writing [121]. This value of n_s is largely independent of the theory model described above, depending primarily on the measured values of I_c, B_{c2}, and w. This derivation also relies on the value of l/φ_c which we extract from the theory model, but this parameter does not vary significantly since the bridge lengths are generally around 100 nm and the critical phases are largely between π and 2π. We find that n_s of the bridges tends to be slightly lower than the minimum n_s of the annulus given by the theory model, which is on the order of 10^{12} cm^{-2}. This is consistent with weak links being written by lower c-AFM tip voltage compared to the annulus. We also note that

SQUID B	$I+$ left, I_- left	$I+$ right, I_- right	$I+$ right, I_- left	$I+$ left, I_- right
$l_{\mathrm{l}}/\xi_{\mathrm{GL}}$	10.2	5.1	12.0	10.6
$l_{\mathrm{r}}/\xi_{\mathrm{GL}}$	10.5	8.8	8.7	4.9
$I_{\mathrm{c,l}}$ (nA)	40.8	19.3	22.0	25.3
$I_{\mathrm{c,r}}$ (nA)	46.5	24.3	27.8	35.1
$\varphi_{\mathrm{c,l}}$ (rad)	5.68	3.13	6.52	5.76
$\varphi_{\mathrm{c,r}}$ (rad)	5.83	4.73	4.72	3.04
$L_{\mathrm{k,l}}$ (nH)	32.3	36.3	49.5	54.1
$L_{\mathrm{k,r}}$ (nH)	29.1	46.5	40.2	19.4
Min. annulus n_{s} (10^{11} cm^{-2})	22	3.2	2.5	6.7
$n_{\mathrm{s,l}}$ (10^{11} cm^{-2})	7.49	3.18	4.14	4.56
$n_{\mathrm{s,r}}$ (10^{11} cm^{-2})	8.57	4.62	5.24	5.73

Table 3: Length $l_{\mathrm{l(r)}}$, critical current $I_{\mathrm{c,l(r)}}$, critical phase $\varphi_{\mathrm{c,l(r)}}$, and kinetic inductance $L_{\mathrm{k,l(r)}}$, of each bridge in SQUID B, determined by theoretical fit. Minimum n_{s} in the annulus given by theory model, and n_{s} in the bridges calculated from I_{c}, are also listed. Different columns represent different lead orientations, with fits shown in Fig. 18.

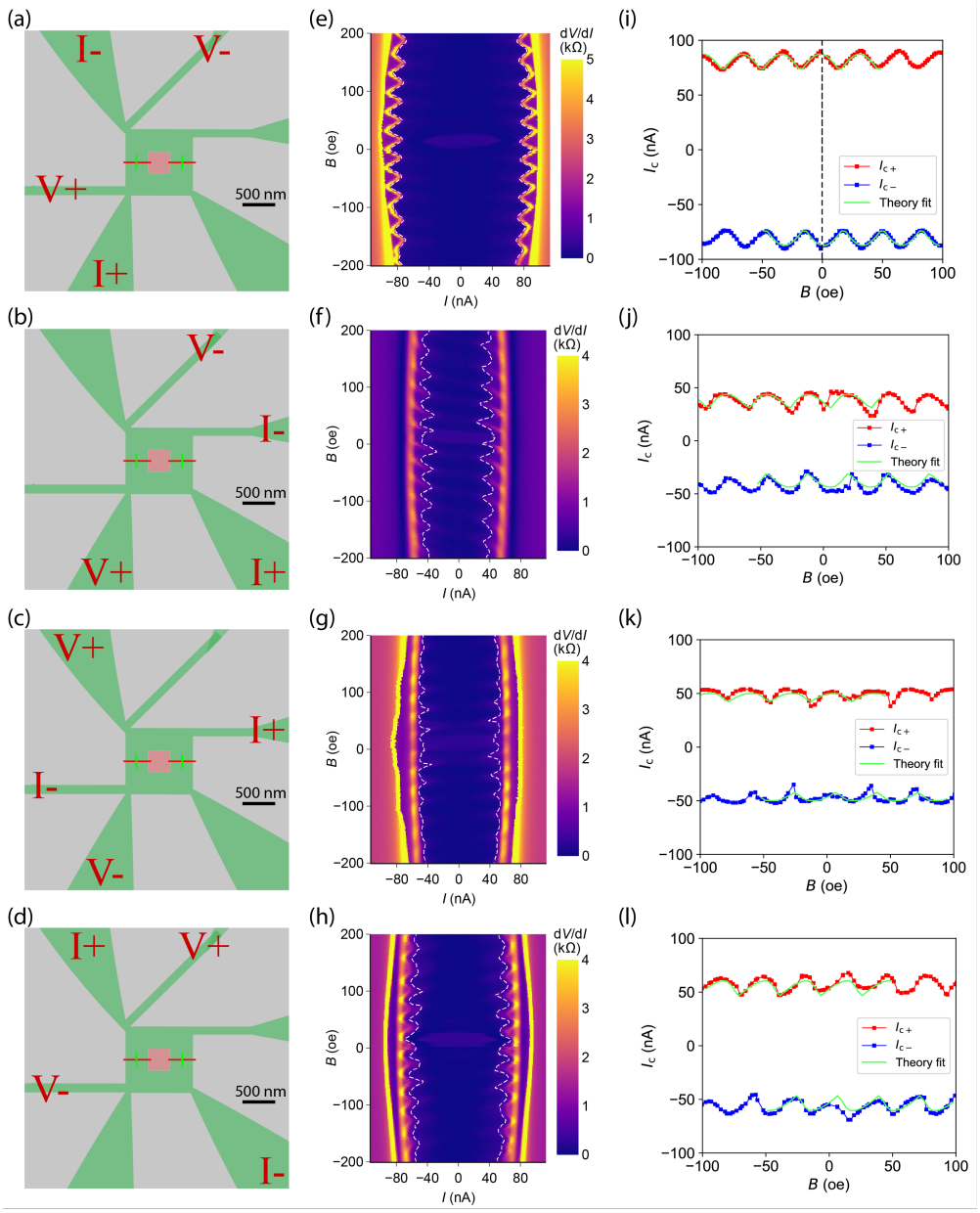

Figure 18: Lead configurations and resistance of SQUID B, with fits for each case. (a)-(d) Lead configurations (e)-(h) Resistance of the SQUID versus external magnetic field and current through the device (i)(l) Fit of $I_{c,in}$ versus external magnetic field overlaid on data for each configuration. The figure is adopted from Ref. [120].

n_s 10^{12} cm^{-2} is much lower than the total carrier density ($n_2D = 5.410^{13}$ cm^{-2}) as obtained from Hall measurement. To our knowledge there is no other report on the superfluid density or kinetic inductance on the KTO (110) 2DEG. Ref. [72] reports a superfluid density of $n_s = 1.810^{12}$ cm^{-2} (which corresponds to kinetic inductance per square area of 1.1 nH/sq) and a total carrier density $n_2D = 7.510^{13}$ cm^{-2} in KTO (111) 2DEG. These values are on the same order as what we observe in KTO (110), but we note these are two different KTO systems with different T_c.

3.3 Coupling of current-phase relations of half-annuli and Dayem bridges

Solving for the current density in the annulus entails minimizing the energy and therefore solving

$$\hbar\nabla^2\varphi = \frac{e^*}{c}\nabla \cdot A. \tag{52}$$

We use the Landau gauge $A = By\hat{x}$ with magnetic field $B = B\hat{z}$ which is perpendicular to the plane of the device, and therefore $\nabla \cdot A = 0$. We supplement the Laplace equation with the Neumann boundary condition that $(\hbar\nabla\varphi - \frac{e^*}{c}A) \cdot \hat{n} = j$. The boundary normal current j is selected to be 0 such that no current penetrates the boundaries of the device, except at the Dayem bridges and the current source leads where we specify j. We discretize the resulting Laplace equation and solve it by successive over-relaxation on one half-annulus of the device. This is implemented in Python by defining a NumpPy array that represents a 2-dimensional grid of cells of the phase across the half-annular regions. The details of implementing the successive over-relaxation algorithm are given in Appendix 3.5.1. In order to derive a current-phase relation for the device, we consider the phases at the two Dayem bridges, φ_1 and φ_2, and the phase at the lead attachment point, θ. Solving the Laplace equation relates these phases and the magnetic field to the currents j_1 and j_2 at the bridges. In particular,

$$j_1 = M_{11}(\theta - \varphi_1) + M_{12}(\theta - \varphi_2) + K_1B \tag{53}$$

$$j_2 = M_{21}(\theta - \varphi_1) + M_{22}(\theta - \varphi_2) + K_2B \tag{54}$$

where we fit the constants $M_{11}, M_{12}, M_{21}, M_{22}, K_1, K_2$ to solutions of the Laplace equation. We do this fitting procedure with LinearModelFit[] in Mathematica, where we have imported the current, phase, and external field data generated by our model in Python. We incorporate the Dayem bridges using their current-phase relation $J_i\ (\Delta\varphi_i)$, where $\Delta\varphi_i$ is the phase difference across the i-th bridge. To obtain relation $J_i\ (\Delta\varphi_i)$, we start with the Ginzburg-Landau free energy

$$F = \int_{-b/2}^{b/2} \alpha|\Psi|^2 + \frac{\beta}{2}|\Psi|^4 + \frac{\hbar^2}{2m}|\nabla\Psi|^2 dx \tag{55}$$

subject to the following conditions:

$$|\Psi(x = \pm\frac{b}{2})|^2 = \frac{\alpha}{\beta} \tag{56}$$

$$\Psi^*\nabla\Psi + \Psi\nabla\Psi^* = J. \tag{57}$$

Taking $\Psi = fe^{-i\varphi}$ and following the derivation in Ref. [89], we arrive at an expression for the phase across a wire carrying a current J. In particular,

$$\Delta\varphi = \int_{-b/2}^{b/2} \frac{J}{f^2(x)} dx. \tag{58}$$

$J(\Delta\varphi)$ calculated for bridges with different lengths l (sampled from l_l and l_r in Table 2 and 3) are plotted in Fig. 20. When l is greater than the Ginzburg-Landau coherence length ξ_{GL}, $J(\Delta\varphi)$ deviates from the sinusoidal relation of typical Josephson junctions, and its critical phase φ_c increases with l. For the modeling in this Chapter, we needed to be able to obtain the current across the Dayem bridges given any phase difference across it, modulo 2π. We also needed to be able to get this current-phase relation for a range of bridge lengths, from around 1 coherence length to around 20 coherence lengths. We accomplished this by using Mathematica's FindRoot[] to solve for the current at discrete values of the phase and for discrete values of the length of the bridge. We then produced an interpolation function of two variables (phase and length) which can closely approximate the current-phase relation at any phase value for any bridge length in the range.

For each bridge in the SQUID, we set $j_i = J_i(\Delta\varphi_i)$ to find the current-phase relationship of the SQUID. Using the derived relationships, we can relate the current into the device,

$j_1 + j_2$, to the phase difference across the whole device, which we extract from the phase across both the bridges and the half-annuli. See Fig. 19 to reference the origin of the phase differences internal to the device and how they are derived. We then determine the critical current at a particular magnetic field by finding the maximum current supported at any phase difference across the entire SQUID.

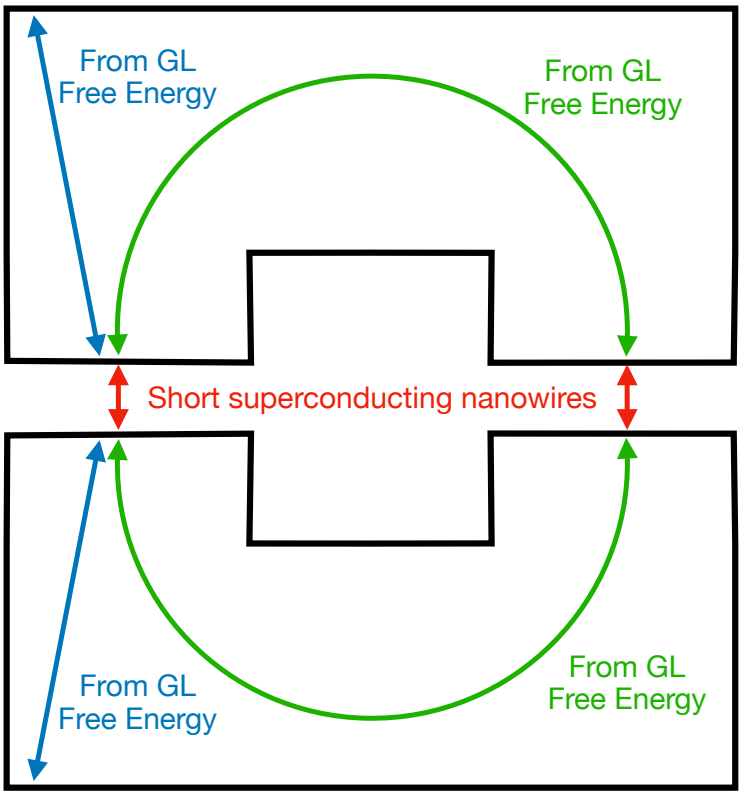

Figure 19: Schematic of a SQUID with current injection leads at the top and bottom left. Arrows indicate relevant phase differences to the model. Phase differences internal to the half-annuli are derived via our successive over-relaxation solution of the GL free energy model of supercurrents and phase gradients. Phases across the Dayem bridges come from the $J(\Delta\varphi)$ relations for short superconducting nanowires specified in this chapter.

The critical current of the bridges can be used to extract their superfluid density n_s, as follows

$$\frac{I_c}{w} = \frac{e^*\hbar}{m^*} n_s \frac{\varphi_c}{l} \tag{59}$$

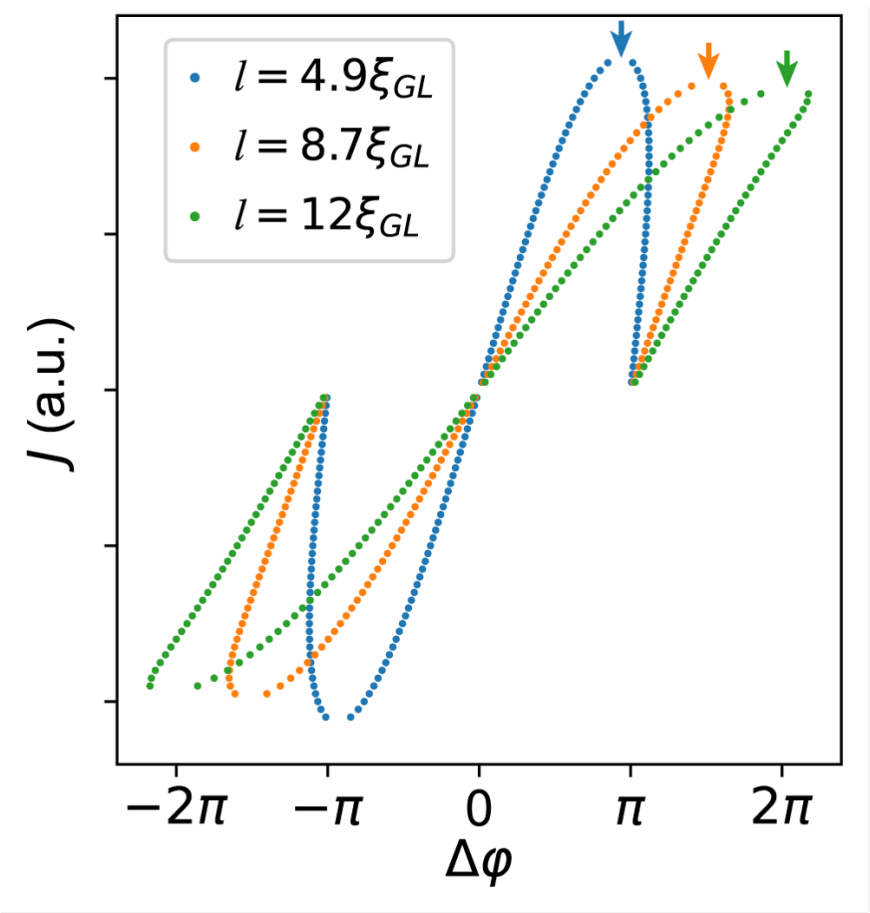

Figure 20: Current-phase relations of bridges of varying length as a multiple of coherence length. Shorter bridges behave sinusoidally, while longer bridges reach closer to a linear current-phase relation.

where φ_c is the critical phase of the bridge while l and w are its length and width, respectively. Our model provides a fit for l/ξ_{GL}, and so we can use this combined with the fact that $\xi_{GL} = \sqrt{\frac{\varphi_0}{2\pi B_{c2}}}$ to find l, where the upper critical field $B_{c2} = 0.23\ T$. Combining the experimental parameters I_c and B_{c2} with the theory fit parameters l/ξ_{GL} and φ_c, we compute n_s for each bridge.

3.4 Summary

In this Chapter, we derived important parameters for the LAO/KTO DC-SQUID by fitting experimentally observed critical current oscillations with magnetic field to our model. We showed that the significantly lower period of oscillation of critical current can be broadly explained by the presence of supercurrents induced by external magnetic fields which penetrate these devices. We then determined that an asymmetry between the left and right bridges in our devices could cause the phase offsets seen between positive and negative critical currents in the device. In particular, for SQUID A, we found an approximate 22% mismatch in critical current and 25% mismatch in critical phase between the left and right bridges. In SQUID B, the mismatch was less pronounced, being about 13% in critical current and about 2% in critical phase.

We determined the kinetic inductance of the bridges to be on the order of 100 nH/μm, or about 2 orders of magnitude higher than in nanowires made of Niobium or other common materials. By demonstrating the high kinetic inductance of these devices, we have established further interest in the material since these material properties make it a candidate for superconducting nanoinductor applications, or in various applications in superconducting circuits. The material could possibly be explored in the context of topological superconductivity due to the combination of its properties, as the mechanism of superconductivity in LAO/KTO remains unknown.

3.5 Appendix

3.5.1 Solving the Laplace equation using successive over-relaxation

In our model of supercurrents and superconducting phase in each half-annulus, we use the method of successive over-relaxation (SOR) in order to minimize the free energy for a grid of points which discretize the system. In particular, we are solving for $\nabla^2\varphi = 0$ in the interior of the device, which equates to current conservation into and out of each unit cell. In

order to discretize the system, we use a finite differences approach. The following is adapted from the derivations in Refs. [46, 26].

Consider a particular cell with phase φ_c with four neighbors, having phases $\varphi_u, \varphi_d, \varphi_r, \varphi_l$ (for up, down, right, and left, respectively). Then, expanding to second order, we have

$$\varphi_r = \varphi_c + h\frac{\partial\varphi}{\partial x} + \frac{1}{2}h^2\frac{\partial^2\varphi}{\partial x^2} \tag{60}$$

$$\varphi_l = \varphi_c - h\frac{\partial\varphi}{\partial x} + \frac{1}{2}h^2\frac{\partial^2\varphi}{\partial x^2}, \tag{61}$$

where h is the grid spacing. Taken together, we have

$$\varphi_r + \varphi_l = 2\varphi_c + h^2\frac{\partial^2\varphi}{\partial x^2}, \tag{62}$$

and analogously in the y direction,

$$\varphi_u + \varphi_d = 2\varphi_c + h^2\frac{\partial^2\varphi}{\partial y^2}. \tag{63}$$

Combining, we have

$$\nabla^2\varphi = (\varphi_r + \varphi_l + \varphi_u + \varphi_d - 4\varphi_c)/h^2, \tag{64}$$

which we can use to solve for φ_c given the value of its neighbors. For interior points, $\nabla^2\varphi = 0$, so φ_c is dependent on only its neighbors. In particular, it is the average of the neighboring phases, and does not depend on h. On the boundaries, we use Neumann boundary conditions as described in Sec. 3.3.

In order to converge on a solution for the phases at all points on the grid, we update the phases at grid points iteratively. First, we assign a parity to each point in the grid in a checkerboard pattern, so that half of the points can be updated based on the other half, independently. At each step, a new value for the phase at each grid point is computed to replace that value. In the interior of the grid, our finite differences analysis shows that the new phase at a given grid point should be the average of the surrounding points (modulo the grid spacing). Updating the grid points via this relaxation process will lead to convergence

to a solution eventually, but is not the fastest approach. Instead, consider updating to $\varphi_{c,\text{new}}$ as follows:

$$\varphi_{c,\text{new}} = (1 - f)\varphi_c + f * \varphi_{\text{update}}, \tag{65}$$

where φ_{update} is the phase computed via our finite differences method. Here, f is known as a relaxation factor, and can be adjusted so that the new values of φ are updated more slowly or quickly to their new values. For $f = 1$, the system is relaxed such that only the new finite-differences value is considered. With $f < 1$, the system is under-relaxed, so that the phases are updated more slowly. However, it has been shown that in 2D systems, there is an optimal relaxation factor to improve convergence time. This factor is $f = 2 - 2\pi/n$, where n is the size of the grid. This factor is generally greater than 1, representing over-relaxation. We use this over-relaxation factor to converge more quickly to the equilibrium phase distribution.

Updating with over-relaxation may be better understood when considering the residual, which is the difference between the newly computed phase value and the original phase value φ_c at the grid cell. Then, we have

$$\varphi_{c,\text{new}} = \varphi_c + f * \text{res}, \tag{66}$$

where res is the residual.

In our particular system, we model the SQUIDs with a 135 by 135 grid for both half-annuli. That is, a half-annulus is 135 cells wide and 67 cells top to bottom (since there is one cell reserved for the space between the two). The hole in the center is then a 45 by 45 cell space. Here, we will list the residual which is computed for each kind of grid point before considering the Neumann boundary conditions for currents at the boundary. These residuals are computed similarly to the above for interior points, but since one of the neighbors does not exist, we must take a first derivative with finite differences to see how to replace this value. For example, for a point on the left boundary, we have that

$$\frac{\varphi_r - \varphi_l}{2h} = A, \tag{67}$$

which enforces that the current normal to the boundary is zero. We have the factor of A since we are actually solving for $\nabla\cdot(\nabla\varphi - A) = 0$. Our choice of gauge dictates that $A = By\hat{x}$ and so has an effect in the x direction. Then, we can solve for $\varphi_l = \varphi_r - 2hBy$. This replaces the left phase as compared to the case for interior points. This extends to all boundaries, as shown for the residuals listed in Eq. (68).

$$\begin{aligned}
\text{res}_{\text{interior}} &= (\varphi_r + \varphi_l + \varphi_u + \varphi_d)/4 - \varphi_c \\
\text{res}_{\text{left}} &= (2\varphi_r + \varphi_u + \varphi_d - 2hBy)/4 - \varphi_c \\
\text{res}_{\text{right}} &= (2\varphi_l + \varphi_u + \varphi_d + 2hBy)/4 - \varphi_c \\
\text{res}_{\text{top}} &= (2\varphi_d + \varphi_l + \varphi_r)/4 - \varphi_c \\
\text{res}_{\text{bottom}} &= (2\varphi_u + \varphi_l + \varphi_r)/4 - \varphi_c \\
\text{res}_{\text{top left}} &= (2\varphi_r + 2\varphi_d - 2hBy)/4 - \varphi_c \\
\text{res}_{\text{top right}} &= (2\varphi_l + 2\varphi_d + 2hBy)/4 - \varphi_c \\
\text{res}_{\text{bottom left}} &= (2\varphi_r + 2\varphi_u - 2hBy)/4 - \varphi_c \\
\text{res}_{\text{bottom right}} &= (2\varphi_l + 2\varphi_u + 2hBy)/4 - \varphi_c
\end{aligned} \tag{68}$$

Then, for boundary points where current perpendicular to the boundary is not zero, we apply Neumann boundary conditions. These points are the top and bottom current injection areas (where the leads of the device meet the half-annuli), and the point where the Dayem bridges connect to each half-annulus. The additional contribution is computed by considering that the current perpendicular to the boundary is no longer zero, but a fixed value. For the case of the current at the top lead,

$$\frac{\varphi_u - \varphi_d}{2h} = j_{\text{in}}, \tag{69}$$

where j_{in} is the current injected at the lead. Since there is no cell above the top lead, we solve for $\varphi_u = 2hj_{\text{in}} + \varphi_d$. When adding this contribution to the residual in Eq. 68, the

additional contribution is $\frac{1}{2}hj_{\text{in}}$. So, for all points with Neumann conditions, we have the corrections

$$\begin{aligned}
\text{res}_{\text{top lead}} &+= \frac{1}{2}hj_{\text{in}} \\
\text{res}_{\text{bottom lead}} &+= -\frac{1}{2}hj_{\text{in}} \\
\text{res}_{\text{left bridge top}} &+= \frac{1}{2}hj_1 \\
\text{res}_{\text{left bridge bottom}} &+= -\frac{1}{2}hj_{\text{in}} \\
\text{res}_{\text{right bridge top}} &+= \frac{1}{2}hj_2 \\
\text{res}_{\text{right bridge bottom}} &+= -\frac{1}{2}hj_2
\end{aligned} \tag{70}$$

where += refers to adding this to the residual based on the specifications in Eq. (68) according to the geometry of the grid cell. Here, j_1, j_2 are the currents through the bridges, and we enforce that $j_{\text{in}} + j_1 + j_2 = 0$ (the currents could also be current densities in the case of the leads/bridges being wider than one cell, but we use a single cell here. Can multiply by width to account for number of cells if necessary). We provide a depiction of the grid with cells colored to indicate each type of boundary in Fig. 21.

Note that while here we have given the list of Neumann conditions for both half-annuli, it is only necessary to simulate one of the half-annuli in order to obtain the relation between phase differences across the annulus and the currents at the bridges/leads, as well as external magnetic fields.

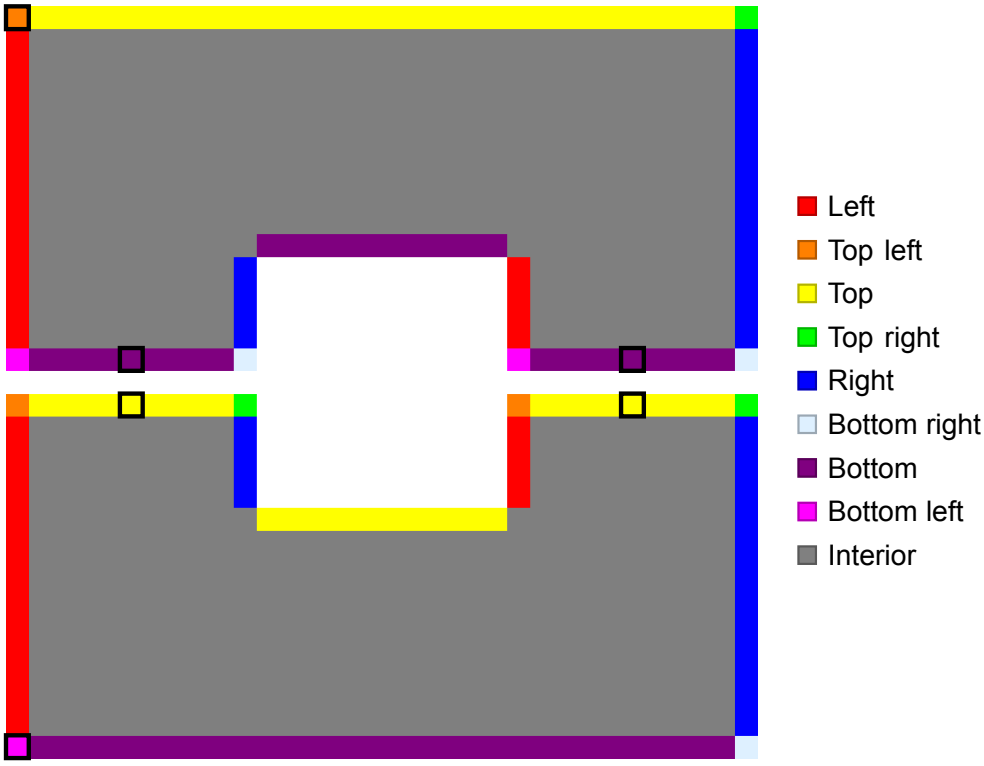

Figure 21: Map of the two half-annuli as simulated by SOR with 33 grid cells in each direction. Boundary points are color coded based on the type of boundary. Interior cells are in gray and white areas represent regions which are not superconducting. Cells with a black border are those where Neumann conditions are applied for nonzero currents into/out of the cell, e.g. at the leads and Dayem bridges.

4.0 Pump-efficient Josephson parametric amplifiers with high saturation power

4.1 Introduction

The Josephson parametric amplifier (JPA), which has been extensively studied for its low noise profile [36, 35, 123, 18], plays an important role in superconducting quantum computing. It uses the Josephson junction to amplify weak microwave signals with nearly quantum-limited added noise. Due to its ultralow-noise performance, the JPA is vital for qubit state readout [110, 64, 47, 56] for applications such as quantum state tomography [71], and, crucially, quantum error correction [74, 58, 29, 101].

JPAs rely on parametric amplification, which occurs when the amplifier circuit's parameter (e.g., inductance) is varied periodically at a specific frequency. In a microwave-pumped JPA, the periodic variation is achieved by using the nonlinearity of the Josephson junction to couple in a strong pump wave. Specifically, the nonlinearity mixes different frequency components of microwave signals. In particular, we consider the three-wave mixing case, where the pump wave at frequency ω_p and the signal wave at frequency ω_s mix and generate an idler wave at frequency $\omega_\mathrm{i} = \omega_\mathrm{p} - \omega_\mathrm{s}$. The parametric process transfers energy from the pump wave to the signal and idler waves and thus amplifies the incoming signals [9, 8, 95].

Based on signal and idler frequencies, parametric amplifiers are classified into phase-sensitive and phase-preserving amplifiers [4]. The phase-sensitive amplifier is also called the degenerate amplifier because its signal and idler frequencies coincide and are hosted in the same physical mode. Since the pump frequency is exactly twice the mode center frequency in this case, the power gain of the degenerate amplifier is sensitive to the relative phase between the pump and signal waves near the center of the amplifier's mode frequency. In contrast, the phase-preserving amplifier, also known as the nondegenerate amplifier, has different signal and idler frequencies. In this case, the amplitude and phase information of the signal wave is maintained during the amplification process.

As JPAs are crucial for their low noise profile, it is necessary to quantify how much noise

they add to an amplified signal. A linear amplifier with power gain G will amplify a signal such that if the input consists of n_{s} photons, the output has photon number Gn_{s}. The output signal of this amplification process will have noise due to vacuum fluctuations of the input and any noise added by the amplifier, which we can call n_{A}. The noise of an amplifier is usually referred to in terms of its quantum efficiency, which is defined as

$$\mathrm{QE} = \frac{1}{1 + 2n_{\mathrm{A}}}. \tag{71}$$

Since a nondegenerate amplifier will generate a tone at the idler frequency, this channel will also introduce noise, which at a minimum is equal to zero-point quantum fluctuations of half a photon. I.e. $n_{\mathrm{i}} \geq \frac{1}{2}$, where n_{i} is the noise of the idler channel. At the output, this will result in $n_{\mathrm{i}}(G-1)$ photons of noise, and so referencing the input, we have

$$n_{\mathrm{A}} = n_{\mathrm{i}} \frac{G-1}{G} \tag{72}$$

of noise. Since n_{i} is at least half a photon, we have a limit of $(1 - 1/G)/2$ added noise, which in the limit of large gain, is half a photon. If we consider our definition of quantum efficiency, we see that $\mathrm{QE} \leq \frac{1}{2}$ in the large gain limit [21, 93, 30].

JPAs are able to add this minimum noise throughout the parametric amplification process with a power gain of around 20 dB [122, 4]. In particular, they are operated such that $k_B T \ll hf$, i.e. the thermal noise of the system is less than the zero-point quantum fluctuations of the environment. These noise and gain characteristics at low temperature make JPAs ideal as the first stage of an amplifier chain in superconducting quantum computing applications where the input signal is on the order of only a few photons. In this case, the JPA need only provide sufficient gain to saturate the excess noise of commercial cryogenic high electron mobility transistor (HEMT) amplifiers [4, 2].

Other amplifier technologies are also used in similar applications, but with a different set of trade-offs. One example is the Josephson traveling-wave parametric amplifier (JTWPA), which is composed of a transmission line containing Josephson junctions in series. Pumping these Josephson junctions varies their inductance nonlinearly, amplifying the signal across the JTWPA's length. These devices vary from JPAs in that they are not simple resonators, and so have characteristics such as gain and bandwidth which depend only on the nonlinear

transmission line. These devices can be very broad bandwidth, and also have the advantage of being directional amplifiers, since amplification only occurs in the direction of propagation of the pump wave. These devices are not, however, able to achieve the same low noise of the JPAs, usually imparting around four times the standard quantum limit. They also require a larger number of Josephson junctions, which can make them more difficult to manufacture [4, 114].

Besides added noise and gain, input saturation power and pump efficiency are also essential characteristics of the performance of parametric amplifiers [19, 34, 40, 102, 56]. The saturation power, P_{sat}, is defined as the smallest signal power at which the gain varies from the target gain G_{t} by more than ± 1 dB. As quantum computing systems scale up with more qubits, we need to process a greater number of signals simultaneously. Such multiplexed applications are possible for amplifiers with a large saturation power and low intermodulation product, since it enables us to read more qubit states over a wider range of input powers without distortion.

Older amplifier designs like Josephson parametric converters had relatively low saturation power. Surprisingly, the saturation power of these amplifiers was not limited by pump depletion. Instead, these amplifiers used a small number of Josephson junctions and, therefore, relatively small signal powers caused them to leave the desired nonlinear regime [68]. The newer generation of amplifiers splits the signal amplitude across many more Josephson junctions, thus resulting in a much larger saturation power [40, 56].

Another class of amplifiers called kinetic inductance parametric amplifiers (KIPAs) exist which also address the issue of saturation power by forgoing amplification by Josephson junctions, instead taking advantage of nonlinearities due to the kinetic inductance of a superconducting material [24, 85, 39]. In Ref. [68], it was shown that higher order nonlinearities intrinsic to Josephson-based amplifiers are the dominant factor in limiting saturation power. The KIPA, while addressing this problem, is still not broadly manufactured and is still being actively researched. Additionally, it may be difficult to tune the KIPAs nonlinearities in order to improve amplifier performance. The ability to engineer nonlinearities is key to the work in this Chapter, and we will address how higher order nonlinearities affect amplifier performance in JPAs in Section 4.3.

The subject of this Chapter is pump efficiency, which characterizes the capacity of an amplifier to convert input power from the pump to output signal power without distorting the signal. Specifically, we use the power added efficiency (PAE) as given on page 597 in Ref. [92], which is defined as

$$\eta_{\mathrm{PAE}}(A_{\mathrm{s}}) = \frac{P_{\mathrm{out}} - P_{\mathrm{in}}}{P_{\mathrm{pump}}} = \frac{(G(A_{\mathrm{s}}) - 1)\omega_{\mathrm{s}}^2 A_{\mathrm{s}}^2}{\omega_{\mathrm{p}}^2 A_{\mathrm{p}}^2}, \tag{73}$$

where $G(A_{\mathrm{s}})$ is the power gain as a function of the input signal amplitude A_{s}, A_{p} is the amplitude of the pump, and ω_{s} and ω_{p} refer to the signal and pump frequencies, respectively. Here, P_{in} is the power of the input signal and P_{pump} is the power of the pump wave. We note that P_{out} consists only of the power being converted as output at the signal frequency, while ignoring the power at the idler frequency. Therefore, for nondegenerate amplifiers, but not degenerate amplifiers, approximately half of the output power, which comes out at the idler frequency, is not accounted for in the PAE. We choose this definition because we expect that only the signal frequency will be used downstream. We also note that in this Chapter, we will focus on amplifiers with a target gain of $G_{\mathrm{t}} = 20$ dB.

We define the PAE of an amplifier, η_{PAE}, to be the maximum value of $\eta_{\mathrm{PAE}}(A_{\mathrm{s}})$ in the range of A_{s} below saturation amplitude, A_{sat}. A higher PAE is desirable in JPAs used in large scale quantum computing applications to minimize heat load on the fridge. However, modern JPA designs tend to have pump efficiencies ($P_{\mathrm{out}}/P_{\mathrm{pump}}$) of less than $\sim$0.1% [102], indicating a huge gap between desired and actual performance levels. The performance of previous amplifiers can be seen in Fig. 22, which shows that most designs have low PAE.

In this Chapter, we will investigate the ultimate limit on the PAE of a class of parametric amplifiers illustrated in Fig. 23. We will show that amplifiers within this class can have a PAE orders of magnitude higher than typical JPA designs. Specifically, this is the class of amplifiers that consist of a capacitor (denoted by C) in parallel with a nonlinear inductive block with energy $E[\phi]$. This inductive block will be composed of inductors and Josephson junctions, and generally will take advantage of the previously identified technique of using repeating identical elements in order to improve saturation power. We will focus on two specific circuits, which we call the RF-SQUID amplifier and the extended RF-SQUID amplifier. The RF-SQUID amplifier, shown in Fig. 24, has an inductive block with a chain of

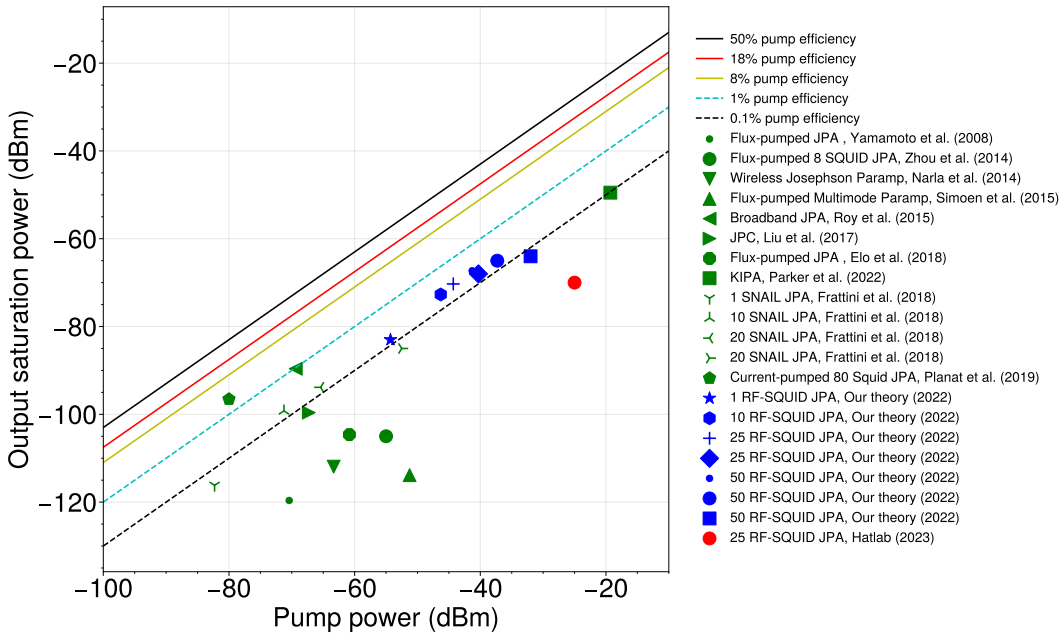

Figure 22: Output saturation power versus cold pump power for various amplifier designs. Each diagonal line indicates a constant pump efficiency. The green points represent previous physical amplifiers, with PAEs mostly on the order of 0.1%. The blue points represent theoretical amplifiers with improved saturation power through repeating identical RF-SQUIDs. The red point represents an attempt to experimentally realize this performance. The figure is adapted from Ref. [102].

RF-SQUIDs. It is currently in use by our Hatlab collaborators, and so we aim to show how its circuit parameters can be tuned to improve PAE. The extended RF-SQUID amplifier, shown in Fig. 25, adds circuit complexity by shunting the RF-SQUIDs with three Josephson junctions with current bias, with the benefit of a more tuneable energy $E[\phi]$ which could allow for higher PAE. Note that we do not consider a coupling capacitor to the transmission line, as is commonly used in experiment. This is because coupling capacitors reduce effective PAE and we are interested in the PAE of the amplifier after the plane of the coupling capacitor.

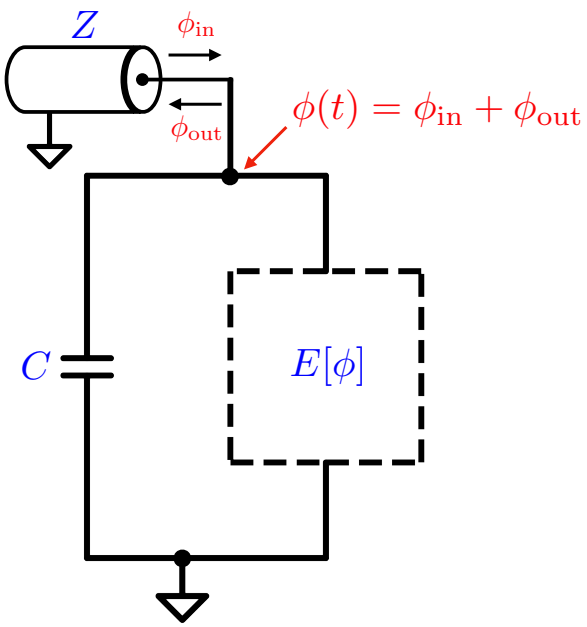

Figure 23: Generic amplifier circuit coupled to a transmission line with impedance Z. The circuit is composed of a capacitor C and an inductive block with energy $E[\phi]$. The amplifier phase $\phi(t)$ is coupled to the transmission line via the input/output relation as indicated.

4.1.1 Amplifiers with arbitrary inductive blocks

We would like to begin by establishing a benchmark for our ability to improve PAE by tuning an amplifier's inductive block. My colleague, Zhuan Li, has established such a benchmark and explored the ultimate limit on PAE by writing the energy of the inductive block of the amplifier as a generic polynomial

$$E[\phi] = \frac{1}{2L_{\text{eff}}}\phi^2 + g_3\phi^3 + g_4\phi^4 + \cdots , \tag{74}$$

where L_{eff} is the effective inductance of the inductive block. He optimized these amplifiers by tuning the g_i coefficients in this polynomial amplifier in order to maximize saturation power and, consequently, PAE. Searching through the space of polynomial amplifiers sets a bound on what level of efficiency is achievable given a certain order of nonlinearity, i.e.,

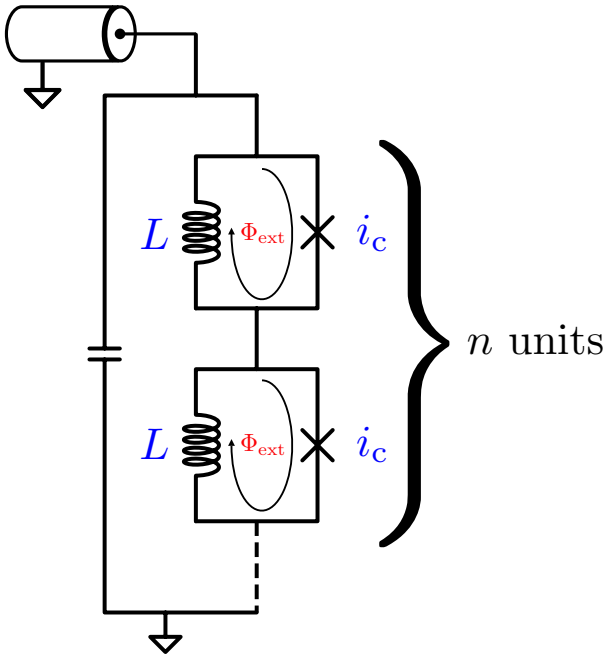

Figure 24: Amplifier circuit with an inductive block composed of a chain of n-many RF-SQUIDs.

we can increase the PAE by adding further terms to $E[\phi]$. Li explored up to tenth order polynomial amplifiers i.e., including terms up to $g_{10}\phi^{10}$, and found that the PAE tends to saturate at around sixth order, where the maximum achievable PAE is at least 63% for degenerate amplifiers with $G_{\mathrm{t}} = 20$ dB. See Table 4 for the PAE of optimized degenerate amplifiers to different polynomial orders.

4.2 Modeling and simulating amplifiers via cQED and direct time integration of equations of motion

In this Section, we lay out the model for a class of parametric amplifiers composed of a capacitor shunted by a nonlinear inductive block and coupled to a transmission line (shown in Fig. 26), derive the classical input-output relation, and obtain the equation of motion

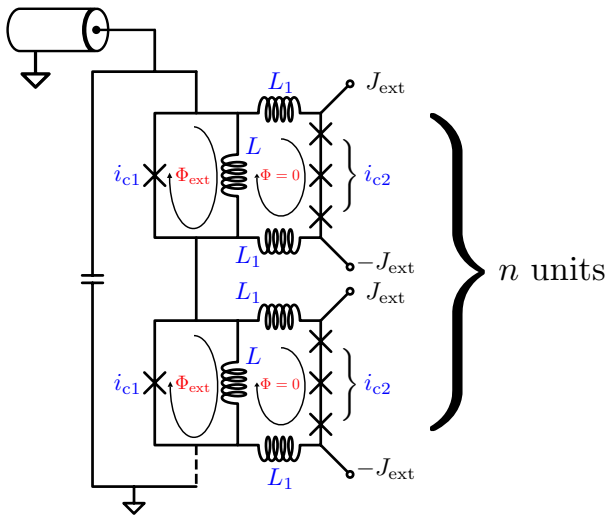

Figure 25: Amplifier circuit design which gives highest PAE. The circuit is composed of n-many RF-SQUIDs, each shunted by 3 current-biased Josephson junctions.

(EOM). Our derivations mainly follow Ref. [112].

Here, the amplifier is made of a capacitor and a nonlinear inductive block whose energy is $E[\phi]$. The Lagrangians of the amplifier, $\mathcal{L}_{\text{s}}$, and the transmission line, $\mathcal{L}_{\text{tl}}$, are

$$\mathcal{L}_{\text{s}} = \frac{C\dot{\phi}^2}{2} - E[\phi], \tag{75}$$

$$\mathcal{L}_{\text{tl}} = \sum_{i=1} \left(\frac{C_l\,\Delta x\,\dot{\phi}_{i+1}^2}{2} - \frac{(\phi_{i+1}-\phi_i)^2}{2L_l\,\Delta x} \right). \tag{76}$$

To couple the transmission line with the amplifier, we set $\phi_1 = \phi$.

4.2.1 Equations of motion and input-output relations

We first consider the transmission line except for the last node ϕ_1. For $i > 1$, the equation of motion for ϕ_i is given by

$$C_l\,\Delta x\,\ddot{\phi}_i + \frac{\phi_i - \phi_{i-1}}{L_l\,\Delta x} - \frac{\phi_{i+1} - \phi_i}{L_l\,\Delta x} = 0, \tag{77}$$

polynomial order	dimensionless $A_{\rm sat}$	PAE
4	0.0783	48.0%
6	0.0845	63.3%
8	0.0894	62.6%
10	0.0895	62.7%

Table 4: Saturation amplitude $A_{\rm sat}$ and PAE of optimized 20 dB polynomial amplifiers with different orders of nonlinearity.

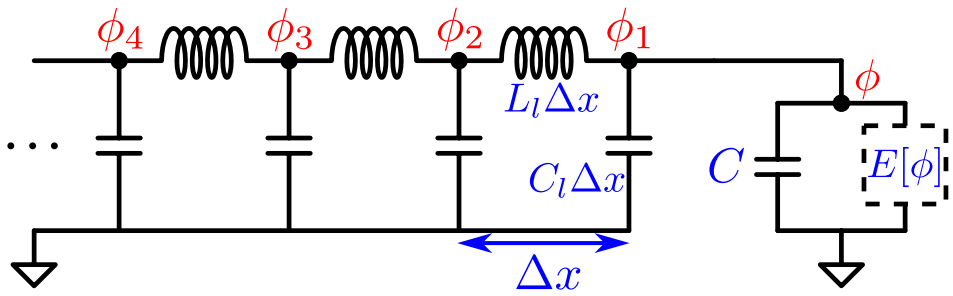

Figure 26: Schematic of the parametric amplifier with an explicit model for the transmission line, which we use to illustrate the origin of the input/output relations. Here, $\phi, \phi_1, \phi_2, \cdots$ are node fluxes in the transmission line; C_l, L_l are capacitance and inductance per unit length, respectively; Δx is the cell length. The figure is adopted from Ref. [50].

which in the continuum limit, $\Delta x \to 0$, becomes the wave equation,

$$\ddot{\phi} + \frac{\phi''}{C_l L_l} = 0, \tag{78}$$

where $'$ denotes the spatial derivative. We define the incoming and outgoing waves $\phi_{\rm in}$ and $\phi_{\rm out}$ such that

$$\left(\frac{\partial}{\partial t} + \frac{1}{\sqrt{C_l L_l}}\frac{\partial}{\partial x}\right)\phi_{\rm in} = 0, \tag{79}$$

$$\left(\frac{\partial}{\partial t} - \frac{1}{\sqrt{C_l L_l}}\frac{\partial}{\partial x}\right)\phi_{\rm out} = 0. \tag{80}$$

Then we have

$$\phi(x,t) = \phi_{\text{in}}(x,t) + \phi_{\text{out}}(x,t). \tag{81}$$

Next, we consider the boundary node flux $\phi_1 = \phi$, which gives the input-output relation

$$\phi(t) = \phi(0,t) = \phi_{\text{out}}(0,t) + \phi_{\text{in}}(0,t). \tag{82}$$

We can also consider the relation of currents at the boundary node. In particular, if the current at the node ϕ is I, then

$$I = I_{\text{in}} - I_{\text{out}}, \tag{83}$$

where $I = \dot{\phi}/Z, I_{\text{in}} = \dot{\phi}_{\text{in}}/Z, I_{\text{out}} = \dot{\phi}_{\text{out}}/Z$ where $Z = \sqrt{L_l/C_l}$ is the characteristic impedance of the transmission line. From Eq. (82), we can write that $\dot{\phi}_{\text{out}} = \dot{\phi} - \dot{\phi}_{\text{in}}$. Then, plugging into the above, we have that

$$I = \frac{2\dot{\phi}_{\text{in}}}{Z} - \frac{\dot{\phi}}{Z}. \tag{84}$$

Coupling the transmission line to the amplifier, this current must be equal to the current given by the EOM of the amplifier, which is given by Lagrangian mechanics for our $\mathcal{L}_{\text{s}}$, resulting in the relation

$$C\ddot{\phi} + J[\phi] = \frac{2\dot{\phi}_{\text{in}}}{Z} - \frac{\dot{\phi}}{Z}, \tag{85}$$

where $J[\phi] = dE/d\phi$ is the current through the inductive block as a function of the phase across the block, ϕ. Finally, we can write the evolution of the nonlinear system as

$$\ddot{\phi} + K\dot{\phi} + \frac{J[\phi]}{C} = 2K\dot{\phi}_{\text{in}}, \tag{86}$$

where $K = \frac{1}{CZ}$ is the damping rate of the amplifier from its coupling to the transmission line.

For a polynomial amplifier with energy as in Eq. (74), the equation of motion is then

$$\ddot{\phi} + K\dot{\phi} + \omega_0^2\phi + 3g_3\phi^2 + \cdots + ng_n\phi^{n-1} = 2K\dot{\phi}_{\text{in}}, \tag{87}$$

where $\omega_0 = 1/\sqrt{CL_{\text{eff}}}$ and we have rescaled the g_i coefficients appropriately on division through by C.

4.2.2 Equations of motion of Josephson parametric amplifiers

In this Subsection, we will discuss how to construct the inductive block $E[\phi]$ from linear inductors and Josephson junctions. We start from the Lagrangian description of inductors and Josephson junctions. The contributions of these elements to the energy $E[\phi]$ are

$$E_L = \frac{\phi_0^2}{2L}(\varphi_1 - \varphi_2)^2, \tag{88}$$

$$E_J = -\phi_0 i_c \cos(\varphi_1 - \varphi_2), \tag{89}$$

where E_L, E_J are the contributions of inductors and Josephson junctions, respectively. Here, L is inductance, i_c is Josephson critical current, and ϕ_0 is the reduced magnetic flux quantum. Here we use dimensionless fluxes $\varphi_i = \phi_i/\phi_0$. In addition, we consider both current and flux biases in these circuits.

We represent the inductive block $E[\varphi]$ by a network of internal inductive components which make up our circuit design. Specifically, the circuit is composed of a set of internal nodes φ_i that are connected by the inductive components. In Ref. [96], it was shown that stray capacitances could have important effects. We discuss the effect of capacitive terms within the inductive block in Subsec. 4.4.2.

For each node φ_i, we write that $\frac{1}{\phi_0}\frac{\partial \mathcal{L}}{\partial \varphi_i} = J_i = J_{\text{ext},i}$ where $J_{\text{ext},i}$ is the current bias at node φ_i. Typically, nodes are not current biased and thus have $J_i = 0$. From here we proceed as in Ref. [68].

We also bias the circuit by applying external magnetic flux through closed loops in the circuit. Without loss of generality, we model magnetic flux bias by describing it as a phase offset across one of the Josephson junctions in the loop. In particular, a Josephson junction in a loop with an applied external flux of Φ_{ext} will have a contribution of $\frac{\phi_0^2}{2L}(\varphi_1 - \varphi_2 + \varphi_{\text{ext}})^2$ to the Lagrangian, where $\varphi_{\text{ext}} = \Phi_{\text{ext}}/\phi_0$.

To make these considerations concrete, we examine the case of a JPA with an inductive block composed of n-many radio frequency superconducting quantum interference devices (RF-SQUIDs) [115, 56, 55] as shown in Fig. 24. In this case, we will for now describe only a single RF-SQUID making the assumption that the flux φ across the inductive block is divided equally among the n-many identical SQUIDs, and therefore each SQUID experiences a flux

of $\frac{\varphi}{n}$. In Subsec. 4.4.2, we investigate this assumption and show that it holds in the case that the RF-SQUIDs have a monotonic current-phase relation. The resulting equation of motion is

$$\ddot{\varphi} + K\dot{\varphi} + \frac{\varphi}{nLC} + \frac{i_\mathrm{c}}{\phi_0 C}\sin\left(\frac{\varphi}{n} + \varphi_\mathrm{ext}\right) = 2K\dot{\varphi_\mathrm{in}}, \tag{90}$$

where L, i_c, and φ_ext are the linear inductance, Josephson critical current, and dimensionless external flux through each RF-SQUID, respectively. In general, we can construct the current-phase relation $J[\varphi]$ for the designed amplifier circuit and apply it to the EOM specified in Eq. (86).

4.2.3 Numerical solutions of EOM and optimization algorithm for PAE

In this section, we provide the optimization algorithm that we use to maximize the PAE of an amplifier with the equation of motion

$$\ddot{\varphi} + K\dot{\varphi} + \frac{\partial_\varphi E[\varphi]}{C\phi_0} = 2K\dot{\varphi_\mathrm{in}}, \tag{91}$$

where $E[\varphi]$ is the energy of the inductive block in the JPA circuit. The amplifier's equation of motion will be solved with the incoming wave

$$\varphi_\mathrm{in} = A_\mathrm{s}\sin(\omega_\mathrm{s}t) + A_\mathrm{p}\sin(\omega_\mathrm{p}t + \delta), \tag{92}$$

where $\omega_\mathrm{s}, \omega_\mathrm{p}$ are the signal and pump frequencies, $A_\mathrm{s}, A_\mathrm{p}$ are the signal and pump amplitudes, and δ is the phase difference between the signal and pump wave. Because the differential equation is in general nonlinear, inhomogeneous, and non-autonomous, obtaining analytical solutions is (almost always) not possible. Thus, we make use of the the direct time integration (DTI) numerical method to solve this differential equation.

The DTI method is based on numerical integration techniques that approximate the differential equation by using finite differences. The DTI method uses function values and finite differences at current and previous time intervals to find the value at the next interval. In our calculation, we use the Python method *scipy.integrate.odeint* [111] to solve the nonlinear differential equation. For a chosen integration time, we build an array of time values at

which we will solve for $\varphi(t)$, where we specify the number of sample points based on the frequency of the signal wave. Since we want to obtain a steady-state solution, we choose our integration time to be at least 2000 periods of the signal wave. Then, to remove the initial transient, we only analyze the data from the last quarter of the integration time. For systems with both differential and algebraic equations, i.e. those with intermediate nodes φ_i, we solve the algebraic portion of the system before integrating by using *fsolve*, a method provided in *scipy.optimize*. After obtaining the solution in the time domain, we apply the discrete Fourier transform (DFT) as implemented in *scipy.fft* to isolate the outgoing wave at the signal frequency from the rest of the solution. This requires that the last quarter of the integration time is a multiple of $T_{\min} = \mathrm{lcm}(\frac{2\pi}{\omega_\mathrm{s}}, \frac{2\pi}{\omega_\mathrm{p}})$, where lcm is a function giving the least common multiple of its inputs, which dictates our choice of $\omega_\mathrm{p}/\omega_\mathrm{s}$. Finally, the PAE is determined by calculating both the saturation power gain and the amplitude of the signal wave at that gain.

While we wish to maximize the PAE of the amplifier directly, this is difficult, and therefore we use a proxy. Specifically, we minimize the difference between the amplifier gain and G_t over the largest possible range of A_s. To do this, we define a cost function f which sums the square differences between the target gain and the amplifier gain from our circuit parameters. We minimize this difference using *scipy.optimize.minimize*, which offers several algorithms to find minima. Some of these methods, such as the conjugate gradient method, rely on taking gradients to determine which direction the optimization should move so as to reach a gradient of zero, indicating an extremum. Alternatively, the package offers direct methods such as Nelder-Mead, which relies on only direct function evaluations rather than computing derivatives, with a heuristic algorithm to search the space for minima.

After optimizing the amplifier's gain, we define the highest PAE below the saturation power of the amplifier as the amplifier's PAE. This maximum PAE typically occurs at or near the saturation power of the amplifier (see Fig. 27). The optimization variables we use are the damping rate and other circuit parameters for the particular circuit we are optimizing. In the RF-SQUID amplifier case, the parameters are $K, L, i_\mathrm{c}, \Phi_\mathrm{ext}$. In the extended RF-SQUID amplifier case, the parameters are $K, L, L_1, i_{\mathrm{c}1}, i_{\mathrm{c}2}, \Phi_\mathrm{ext}, J_\mathrm{ext}$. In the remainder of this section, we will present the algorithm step by step with necessary explanations. A

pictorial demonstration of the algorithm is also provided in Fig. 28.

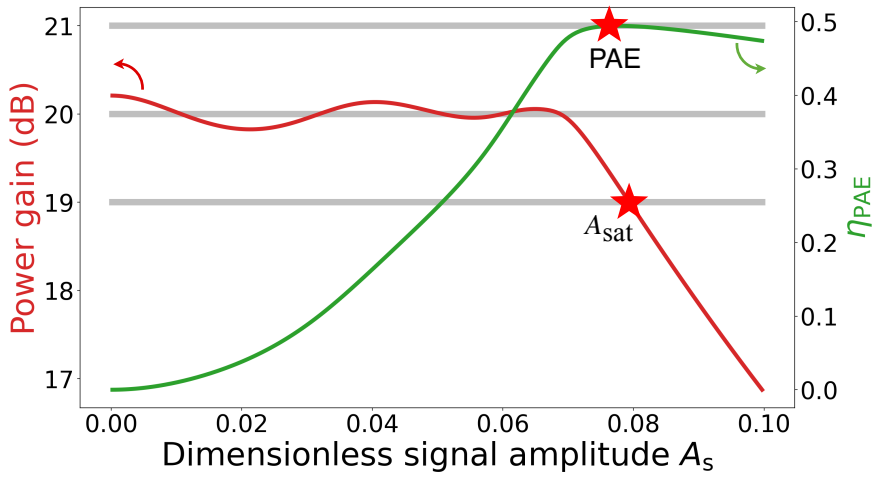

Figure 27: Power gain and PAE versus dimensionless signal amplitude A_{s} of a 6-th order 20 dB degenerate amplifier. The saturation amplitude A_{sat} is the signal amplitude where the gain curve intersects the $G_{\mathrm{t}} \pm 1$ dB lines. The PAE of an amplifier is defined to be the maximum PAE below the saturation power, which typically appears at or around A_{sat}. The figure is adopted from Ref. [50].

Step 1. Choose an initial range $[0, R]$ for A_{s}, and a set of initial optimization parameters. This set of parameters generates an initial gain curve as shown in Fig. 28(a).

Step 2. Divide the region $[0, R]$ into N sub-intervals and define the cost function f as the sum of the squared distance (illustrated in Fig. 28(b)) plus the penalty to enforce requirements on the current-phase relation of our inductive block (further discussed in Sec. 4.4.2).

$$\begin{aligned} & f\left(K^{(0)}, L^{(0)}, \cdots\right) \stackrel{\text{def}}{=} \\ & \sum_{m=1}^{N}\left(G\left(A_{\mathrm{s}}=\frac{mR}{N}, K^{(0)}, L^{(0)}, \cdots\right)-G_{\mathrm{t}}\right)^2+\text{penalty} \end{aligned} \tag{93}$$

For finer optimization, we use an alternative cost function,

$$f\left(K^{(0)}, L^{(0)}, \cdots\right)=\sum_{m=1}^{N} \exp\left\{-1500 /\left(G\left(A_{\mathrm{s}}=\frac{mR}{N}, K^{(0)}, L^{(0)}, \cdots\right)-G_{\mathrm{t}}\right)^2\right\}+\text{penalty} \tag{94}$$

where, if $G = G_t$ for any value of m, then the contribution of that point to the cost is 0.

Step 3. Minimize the cost function f using the gradient descent algorithm. By doing so, we will get a new collection of coefficients $\{K^{(1)}, L^{(1)}, \cdots\}$.

Step 4. Calculate the saturation point for the new curve, which is shown in Fig. 28(d), and reset the new range to be $[0, A_{\text{sat}}]$ if A_{sat} exceeds the previous range R; otherwise, stop the optimization.

Step 5. Redefine the cost function f within the new range as depicted in Fig. 28(e), and repeat steps 3 to 5 until the optimization stops.

Step 6. Record the optimized values of the amplifier parameters $K, L, \cdots$.

We provide further details of this procedure in Appendix 4.7.1.

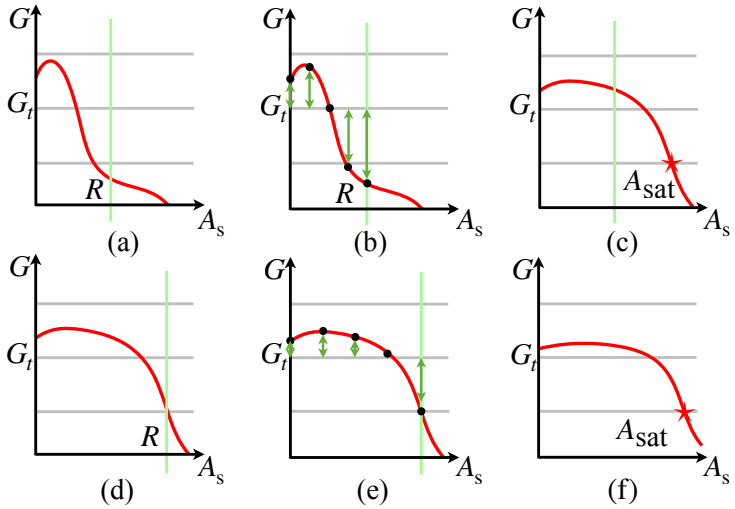

Figure 28: Schematic of optimization algorithm steps. (a) Start from an initial optimization range $[0, R]$ and a set of initial variables $\{K^{(0)}, L^{(0)}, \cdots\}$. (b) Calculate the cost function corresponding to the green arrows. (c) Minimize the cost function. (d)-(e) Update the optimization range $[0, R]$ and re-optimize the amplifier's coefficients until the optimization process stops. (f) Record the optimal values of the amplifier parameters $\{K, L, \cdots\}$. The figure is adopted from Ref. [50].

4.3 Dynamically generated nonlinearities and intermodulation distortion with multiple signals

In this section, we will consider the output of an amplifier with a generic output response to an input signal, and then determine the products of such an amplifier in the case of a two-tone input. We will follow the derivation on pages 511-518 in Ref. [92]. In general,the amplifier's output response can be written as

$$\varphi_{\text{out}} = a_0 + a_1\varphi_{\text{in}} + a_2\varphi_{\text{in}}^2 + a_3\varphi_{\text{in}}^3 + \cdots , \tag{95}$$

where the coefficients a_i give the i-th order response of the amplifier to an input φ_{in}.

If we have $\varphi_{\text{in}} = A(\cos\omega_1 t + \cos\omega_2 t)$, then we have

$$\varphi_{\text{out}} = a_0 + a_1 A(\cos\omega_1 t + \cos\omega_2 t) + a_2 A^2(\cos\omega_1 t + \cos\omega_2 t)^2 + a_3 A^3(\cos\omega_1 t + \cos\omega_2 t)^3 + \cdots . \tag{96}$$

which is equivalent to

$$\begin{aligned}
&a_0 + a_1 A\cos\omega_1 t + a_1 A\cos\omega_2 t \\
&+ \frac{1}{2}a_2A^2(1+\cos 2\omega_1 t) + \frac{1}{2}a_2A^2(1+\cos 2\omega_2 t) + a_2A^2\cos(\omega_1+\omega_2)t + a_2A^2\cos(\omega_1-\omega_2)t \\
&+ a_3A^3\left(\frac{9}{4}\cos\omega_1 t + \frac{1}{4}\cos 3\omega_1 t\right) + a_3A^3\left(\frac{9}{4}\cos\omega_2 t + \frac{1}{4}\cos 3\omega_2 t\right) \\
&+ a_3A^3\left(\frac{3}{4}\cos(2\omega_1+\omega_2)t + \frac{3}{4}\cos(2\omega_1-\omega_2)t\right) + a_3A^3\left(\frac{3}{4}\cos(2\omega_2+\omega_1)t + \frac{3}{4}\cos(2\omega_2-\omega_1)t\right) \\
&+ \cdots ,
\end{aligned} \tag{97}$$

where we have used trigonometric identities to write terms which variously mix ω_1 and ω_2 to different orders.

Here, we see that the third order terms with response a_3 are responsible for the nonlinearity of the amplifier at the signal frequencies as power increases. That is, amplifier performance rolls off from the linear regime in general because a_3 is negative, and so as A increases, the A^3 terms grow and distort the response at ω_1 and ω_2. For two signals nearby in frequency, the third order terms $2\omega_1 - \omega_2$ and $2\omega_2 - \omega_1$ fall near the signals as well, and so

they are third order intermodulation products which disrupt amplifier performance. Since these terms grow cubically and the signal terms grow linearly with amplitude A, it is possible to consider when these terms would be of equal magnitude when ignoring other, higher order corrections. This point is the third order intercept point, or IP3, and we discuss IP3 for our amplifiers in Sec. 4.5.3.

Our approach to improving amplifier performance, including PAE and IP3, relies tuning the inductive block of an amplifier such that its higher order terms, such as a_3 and beyond, are reduced. In order to do so, we must understand the origin of these higher order terms. In many amplifiers, these higher order terms are dynamically generated by intrinsic lower order terms in the equations of motion of the amplifier.

Let us consider the amplifier gain perturbatively for small input signal amplitudes. Here, we will solve the equations of motion of the device at multiples of the signal frequency in the case of a degenerate amplifier with the signal frequency at the amplifier's natural frequency ($\omega_0 = \omega_\mathrm{s}$). We will determine corrections to the amplifier's output at the signal frequency order by order in the input signal amplitude A_s. This analysis forms the basis for the harmonic balance (HB) method of computing amplifier output at the signal frequency, which can be used an alternative to the DTI method outlined in Subsec. 4.2.3.

We will consider the equation of motion $\ddot{\varphi} + K\dot{\varphi} + \omega_\mathrm{s}^2\varphi + 3g_3\varphi^2 = 2K\dot{\varphi_\mathrm{in}}$. The input is $\varphi_\mathrm{in} = A_\mathrm{s}\sin\omega_\mathrm{s}t + A_\mathrm{p}\sin(2\omega_\mathrm{s}t + 3\pi/2)$. In the following analysis, we will consider corrections to the total phase across the amplifier φ as identified by frequency and order. The frequency, as a multiple of the signal frequency, will be indicated by a subscript, while the order of the correction will be indicated as a superscript in parentheses. For example, the second order correction to the $-2\omega_\mathrm{s}$ component will be indicated as $\varphi_{-2}^{(2)}$.

To zeroth order in the signal amplitude, the pump is present at twice the signal frequency, and so we need only consider frequencies $2\omega_\mathrm{s}, 0, 2\omega_\mathrm{s}$. So, we have $\varphi^{(0)} = \varphi_2^{(0)}e^{2i\omega_\mathrm{s}t} + \varphi_0^{(0)} + \varphi_{-2}^{(0)}e^{-2i\omega_\mathrm{s}t}$. Then, the equations of motion are

$$\begin{aligned}
&-4\omega_\mathrm{s}^2\varphi_2^{(0)}e^{2i\omega_\mathrm{s}t} + 2i\omega_\mathrm{s}K\varphi_2^{(0)}e^{2i\omega_\mathrm{s}t} + \omega_\mathrm{s}^2\varphi_2^{(0)}e^{2i\omega_\mathrm{s}t} = -2i\omega_\mathrm{s}KA_\mathrm{p}e^{2i\omega_\mathrm{s}t} \\
&\omega_\mathrm{s}^2\varphi_0^{(0)} + 3g_3(2\varphi_2^{(0)}\varphi_{-2}^{(0)}) = 0 \\
&-4\omega_\mathrm{s}^2\varphi_{-2}^{(0)}e^{-2i\omega_\mathrm{s}t} - 2i\omega_\mathrm{s}K\varphi_{-2}^{(0)}e^{-2i\omega_\mathrm{s}t} + \omega_\mathrm{s}^2\varphi_{-2}^{(0)}e^{-2i\omega_\mathrm{s}t} = 2i\omega_\mathrm{s}KA_\mathrm{p}e^{-2i\omega_\mathrm{s}t},
\end{aligned} \tag{98}$$

where the pump component of φ_{in} is broken up into exponential terms and the equations of motion are split by component frequency since the $2\omega_{\text{s}}, 0, -2\omega_{\text{s}}$ equations are independent. In each of these equations, the exponential terms can be canceled, and so they will be excluded from further analysis in this section. The result of solving these equations gives the value of the $\varphi_2^{(0)}, \varphi_0^{(0)}, \varphi_{-2}^{(0)}$ coefficients. In particular, we get

$$\begin{aligned}\varphi_2^{(0)} &= \frac{-2A_{\text{p}}K}{2K - 3i\omega_{\text{s}}} \\ \varphi_0^{(0)} &= \frac{-24A_{\text{p}}^2 g_3 K^2}{\omega_{\text{s}}^2(4K^2 + 9\omega_{\text{s}}^2)} \\ \varphi_2^{(0)} &= \frac{-2A_{\text{p}}K}{2K + 3i\omega_{\text{s}}}.\end{aligned} \tag{99}$$

We can then continue the process to a first order, which determines the linear relationship between the amplitude of the signal frequency internal to the amplifier and the input signal amplitude. We will compute $\varphi_1^{(1)}, \varphi_{-1}^{(1)}$, and now $\varphi = \varphi^{(0)} + \varphi^{(1)}$. For the $3g_3\varphi^2$ term, we will consider only terms which contribute to $\omega_{\text{s}}, -\omega_{\text{s}}$ and which are linear in the $\varphi^{(1)}$ correction. We solve

$$\begin{aligned}i\omega_{\text{s}}K\varphi_1^{(1)} + 3g_3(2\varphi_2^{(0)}\varphi_{-1}^{(1)} + 2\varphi_0^{(0)}\varphi_1^{(1)}) &= -i\omega_{\text{s}}KA_{\text{p}} \\ -i\omega_{\text{s}}K\varphi_{-1}^{(1)} + 3g_3(2\varphi_{-2}^{(0)}\varphi_1^{(1)} + 2\varphi_0^{(0)}\varphi_{-1}^{(1)}) &= -i\omega_{\text{s}}KA_{\text{p}},\end{aligned} \tag{100}$$

where here the terms originating from $\ddot{\varphi}$ and $\omega_{\text{s}}^2\varphi$ cancel. Solving this, we can find linear relations between $\varphi_1^{(1)}, \varphi_{-1}^{(1)}$ and A_{s}

We can then proceed in a similar manner with second order corrections, which will provide corrections proportional to A_{s}^2 at $2\omega_{\text{s}}, 0, -2\omega_{\text{s}}$. These are generated by the sum of two components at the signal frequency adding to the pump frequency and from coupling of ω_{s} to $-\omega_{\text{s}}$. Finally, we can get third order corrections at $\omega_{\text{s}}, -\omega_{\text{s}}$ from coupling between $2\omega_{\text{s}}$ and $-\omega_{\text{s}}$ and between $-2\omega_{\text{s}}$ and ω_{s}. We also get coupling between the second order $\varphi_0^{(2)}$ term and the $\omega_{\text{s}}, -\omega_{\text{s}}$ terms which also contribute to the third order signal frequency terms. These third order signal frequency corrections will be of order A_{s}^3, which represents dynamically generated nonlinearity due to coupling between the signal and pump, as well as signal with itself. The goal of this research is to extend the Hamiltonian (and thus the equation of motion) of the amplifier by inserting g_4, g_5, and higher order intrinsic nonlinearities in order to cancel

these dynamically generated nonlinearities. These intrinsic nonlinearities are engineered to ensure the linearity of the amplifier output over the greatest possible range of input signal amplitude.

4.4 JPA circuit design rules and limitations

Previous JPA designs have various circuits for their inductive blocks, including single JJs, SNAILs, and other designs as discussed in Sec. 4.1. We start with RF-SQUID based designs shown in Fig. 24, since these are in use by our experimental collaborators in the Hatlab. Our motivation is to improve the PAE of JPA circuits by designing the inductive block $E[\phi]$ so as to convert the greatest possible fraction of pump power to signal power. We expect it is possible to engineer higher PAE by tuning higher order intrinsic nonlinearities in the inductive block in order to cancel higher order, dynamically generated nonlinearities. In particular, the analysis in Sec. 4.3 shows that the linear regime of the amplifier at signal frequencies ends when third order (and higher order) nonlinearities grow sufficiently such that gain deviates from the target by more than 1 dB, i.e. the 1 dB compression point.

The goal of this Chapter is to use the optimization algorithm described in Sec. 4.2.3 to arrive at an amplifier whose nonlinearities maximize PAE. However, there are restrictions on the circuits and parameters which result in stable amplification. In this Section, we will explore design rules which limit the set of amplifiers we can consider in the class of JPAs we have chosen to study.

4.4.1 Vorticies and phase slips in loops consisting of multiple Josephson junctions

In order to add tunability to our RF-SQUID design, we have proposed circuits with the design shown in Fig. 25, which includes an additional branch with three Josephson junctions. These three junctions are biased via an injected current, rather than a flux bias through the loop containing the junctions and the linear inductor. That is, one could consider circuits of

the form in Fig. 29, which would be a natural extension of the simpler RF-SQUID design.

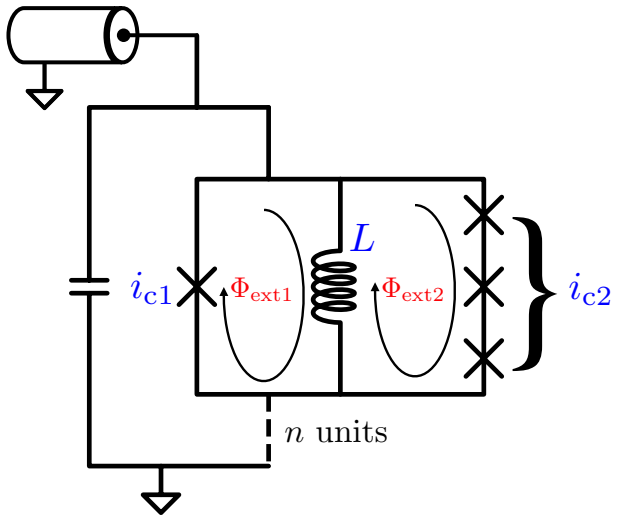

Figure 29: JPA circuit consisting of a chain of repeating RF-SQUIDs shunted by three Josephson junctions in series, with a second flux bias. This circuit is susceptible to phase slips that result in undesirable amplifier performance.

We do not use this design due to the risk of phase slips, which can adversely affect amplifier performance. In the case of this circuit, we anticipate that the phase across the three identical junctions is split equally among them, such that the energy of each junction in that branch is

$$-\phi_0 i_{c2} \cos \frac{\varphi/n + \Phi_{ext2}}{3}, \tag{101}$$

where i_{c2} is the critical current of the three junctions in the additional branch. This energy, however, does not have a period of 2π in phase. Instead, it has a period of 6π, such that slips by 2π or 4π (one or two vorticies crossing a junction) change the energy of the amplifier. Therefore, the true performance of the amplifier will be determined by which of three possible states has the lowest energy.

We have optimized a circuit of this design and plotted its energy-phase relation in the case of a 2π and 4π phase slip in a junction in Fig. 30. We see that the lowest energy solution in this case is not the desired zero phase slip state. The performance of the amplifier with the

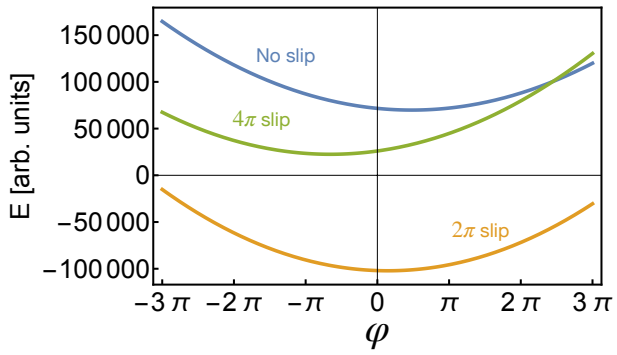

Figure 30: Energy of an optimized JPA circuit of the form in Fig. 29. The energy-phase relation is shown for the case of no phase slip, a 2π phase slip, and a 4π phase slip. Here the lowest energy solution is that of a 2π phase slip.

phase slip will not be equivalent to that of the designed amplifier with no phase slip, since they have different energies. Therefore, we consider only circuits whose design precludes this issue. Our extended RF-SQUID design accomplishes this with current bias in order to tune the Josephson junctions in this branch. This method fixes the phase across the junctions, avoiding phase slips.

4.4.2 Local energy minima and coupling of low- and high-frequency modes in JPA circuits

We must also ensure that our amplifiers are not susceptible to unexpected performance due to the nature of their energy-phase relations. In general, unstable amplification is possible if the energy $E[\phi]$ of the amplifier's inductive block has more than one local minimum. In this case, the amplifier may "jump" to a different minimum if the signal amplitude is sufficiently large. That is, for small signals, the amplifier may oscillate in one local minimum, but then as the signal becomes large enough, the oscillations reach another minimum, which may then become the center of oscillation. In all cases, we would like to ensure that the amplifier has only one minimum, which is a global minimum at $\phi = 0$ (we can assign the global minimum to be at $\phi = 0$ without loss of generality).

This restriction is true for all $E[\phi]$ including arbitrary polynomial amplifiers, not just circuit amplifiers. However, this Chapter focuses on amplifier circuits which are generally composed of n-many identical repeating elements. In this specific case, we will introduce a new design rule with is more strict than the single energy minimum restriction described above.

In this work, we assume that the phase across the amplifier is equally divided across repeating inductive elements, as described in Eq. (90) for the case of the RF-SQUID amplifier. However, this assumption does not hold in some cases. This framework for modeling the behavior of these circuits does not consider the intermediate nodes between each pair of RF-SQUIDs, and so ignores the effects of stray capacitances at these nodes which will be present in physical circuits. The introduction of these stray capacitances allows for dynamic instability of the phase at these intermediate nodes, which can excite high-frequency plasma-like modes.

In particular, this problem arises when the current-phase relation of the repeating element in the amplifier is nonmonotonic. In this case, there may be values of the total phase across the amplifier for which multiple divisions of the phase across the n-many elements are allowed. With the introduction of dynamic effects at the intermediate nodes between these blocks, we are able to determine how this effect disrupts amplifier performance. To model this behavior, we extend the framework for describing amplifier circuit dynamics in Subsec. 4.2.2 by considering intermediate phases φ_i between each of the n repeating elements, with φ_1 representing the phase at the port and φ_{n+1} representing the phase below the bottom element, i.e. connected to ground. At the intermediate nodes, we apply a capacitor and resistor in parallel to ground which provide dynamics and damping. This is shown in the inset in panel (a) of Fig. 31, where we display the two RF-SQUID circuit with an intermediate node. For the case of a circuit with n RF-SQUIDs, we can write the EOM for the intermediate

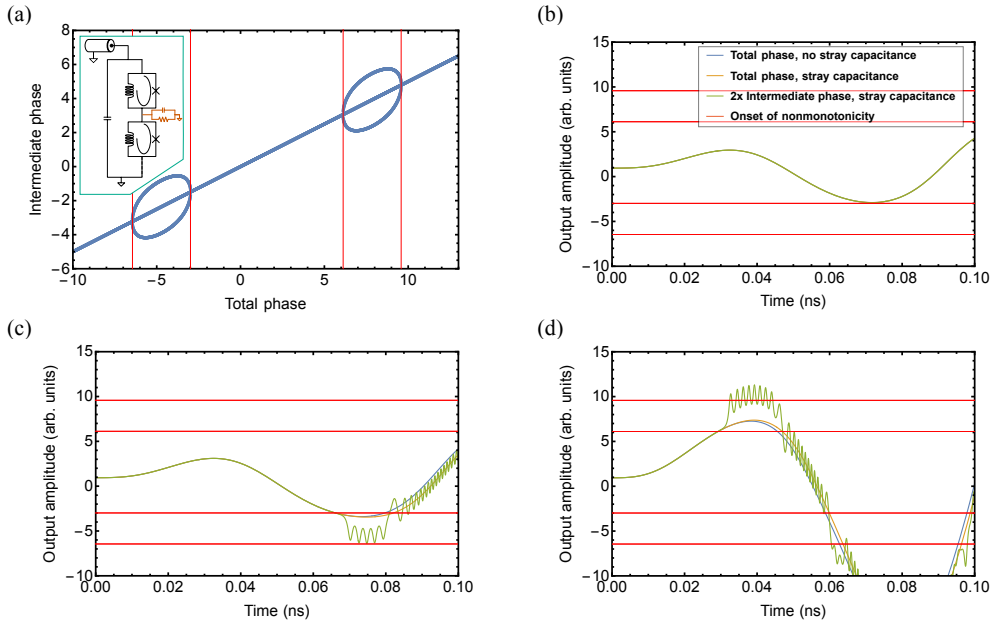

Figure 31: Coupling of low- and high-frequency modes induced by nonmonotonic current-phase relation of constituent RF-SQUIDs. (a) Intermediate phase (i.e. the phase difference across the bottom RF-SQUID, see inset) as a function of the phase difference across both RF-SQUIDs. At the points where the current-phase relation of the RF-SQUID becomes non-monotonic (indicated by the thin red lines), the solution of the intermediate phase equation trifurcates. Inset: circuit diagram of the amplifier with two RF-SQUIDs. Stray capacitance and damping are indicated in orange. (b-d) Real time dynamics of the amplifier with two RF-SQUIDs depicted in the inset of panel (a) for different pump strength. Panel (b) depicts the weak pump case, where the total phase narrowly avoids the nonmonotonic regime and hence the high-frequency mode of the intermediate phase is not excited. Panel (c) depicts a slightly stronger pump, where the total phase narrowly hits the nonmonotonic regime, which results in the ringing up of the high-frequency mode of the intermediate phase. As the high-frequency mode rings up the dynamic solution with the stray capacitor starts to diverges from the dynamic solution without the stray capacitor. Panel (d) depicts an even stronger pump, where the total phase hits the nonmonotonic regime earlier.

nodes as

$$
\begin{aligned}
0 = &\left(\frac{\varphi_i - \varphi_{i-1}}{LC} + \frac{i_\mathrm{c}}{\phi_0 C}\sin\left(\varphi_i - \varphi_{i-1} + \varphi_\mathrm{ext}\right)\right) \\
&- \left(\frac{\varphi_{i+1} - \varphi_i}{LC} + \frac{i_\mathrm{c}}{\phi_0 C}\sin\left(\varphi_{i+1} - \varphi_i + \varphi_\mathrm{ext}\right)\right) \\
&+ \frac{C_s}{C}\ddot{\varphi} + K_s\dot{\varphi}_i,
\end{aligned}
\tag{102}
$$

and for the two boundary nodes as

$$
\begin{aligned}
\ddot{\varphi}_1 + K\dot{\varphi}_1 + \frac{\varphi_1 - \varphi_2}{LC} + \frac{i_\mathrm{c}}{\phi_0 C}\sin\left(\varphi_1 - \varphi_2 + \varphi_\mathrm{ext}\right) \\
= 2K\dot{\varphi_\mathrm{in}}
\end{aligned}
\tag{103}
$$

$$
\varphi_{n+1} = 0 \tag{104}
$$

where C_s is the stray capacitance to ground and K_s is the damping rate at the intermediate nodes.

In Fig. 31, we demonstrate how the time-domain output from an amplifier composed of two RF-SQUIDs is disrupted when the current-phase relation is nonmonotonic. As shown in panel (a), multiple solutions for the phase across each RF-SQUID are allowed when a certain value of the total phase is reached, at which point the solutions for the intermediate phase trifurcate. We see that until the nonmonotonic regime of the RF-SQUIDs is reached, the amplifier behaves as predicted by ignoring intermediate nodes. In order to consider the intermediate nodes, we add a stray capacitance and damping with $C_s = 0.001C$ and $K_s = 0.01K$. In panel (b), we see the time-domain trace resulting from amplifying with a weak pump such that the total phase never reaches the trifurcation point. Here, the total phase as predicted without stray capacitances matches the phase when considering stray capacitances, and the intermediate phase between the RF-SQUIDs is half the total phase as expected. In panel (c), a stronger pump causes the total phase to pass into the trifurcated regime, and at this point the high-frequency mode of the amplifier is excited. Here, the trace predicted by neglecting stray capacitances drifts from the trace considering stray capacitances. Finally, in panel (d), the pump is increased further and the trifurcation is reached sooner, again causing the high-frequency mode to be excited as soon as the amplifier

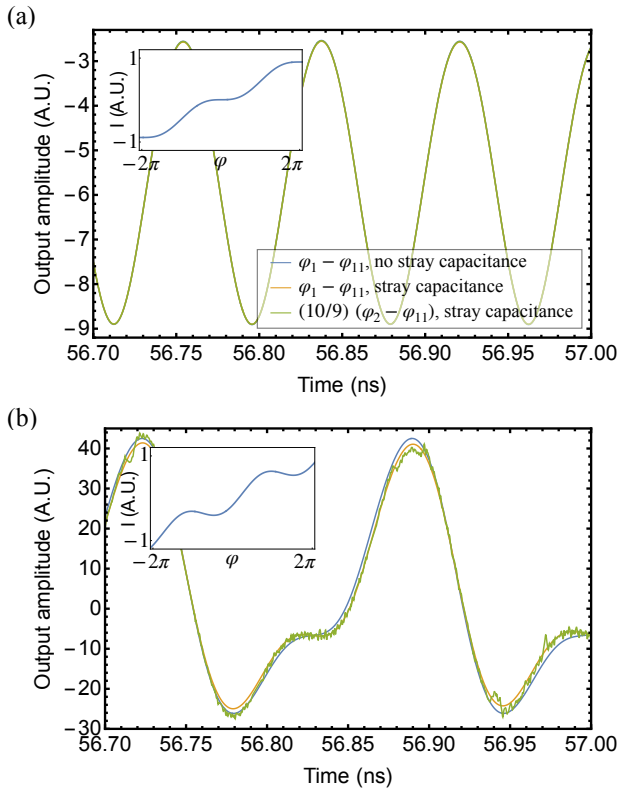

Figure 32: Long-time behavior of amplifiers with inductive blocks with differing current-phase relations. A.U. indicates arbitrary units. (a) Dynamics for an amplifier composed of 10 RF-SQUIDs with monotonic current-phase relation (see inset). The time-domain trace indicates that the phase below the first RF-SQUID and above the following 9 is nearly exactly 9/10 the total phase. Or rather, the phase is divided equally among the RF-SQUIDs and the amplifier is well modeled without stray capacitances. (b) Dynamics for an amplifier composed of 10 RF-SQUIDs with nonmonotonic current-phase relation (see inset). The time-domain trace indicates that the phase below the first RF-SQUID and above the following 9 is unstable, since the nonmonotonicity allows for several ways to divide the phase among the RF-SQUIDs. The amplifier is not well modeled when neglecting stray capacitances since the traces do not agree.

enters this regime. Beyond this point, the traces obtained by considering and by ignoring

stray capacitances do not agree.

This behavior persists in the long-time regime for amplifiers with nonmonotonic current-phase relations and many RF-SQUIDs, as shown in Fig. 32. We simulate the behavior with an inductive block composed of 10 RF-SQUIDs with dynamics at each intermediate node as specified by Eq. (102). We do this for RF-SQUIDs with both monotonic and nonmonotonic current-phase relations, and we find that in the monotonic case the solution converges to the solution with no stray capacitances. Conversely, in the nonmonotonic case, high-frequency modes are always excited and the solution never converges to the no stray capacitance case. We provide additional traces in short- and long-time regimes for varying degrees of monotonicity in Appendix 4.7.1.

Evidence presented in this Section indicates that we should focus on amplifiers with monotonic current-phase relations. This monotonicity implies that the energy-phase relation has only one global minimum, since a monotonic function can only be equal to 0 at one point, and so the energy can have only one extremum. We use monotonicity of the current-phase relation as a design rule for amplifier circuits in the remainder of the Chapter. For RF-SQUID amplifiers, we can impose this requirement analytically. Considering the EOM in Eq. (90), the current-phase relation is monotonic when the oscillations of the sin term are smaller than the slope of the linear term. That is, we enforce that $i_c L/\phi_0 < 1$. In this case, the penalty is

$$\text{penalty} = \lambda\big(\tanh(\ 20\ (i_c L/\phi_0 - 1.15)) + 1\big), \tag{105}$$

where λ is a scaling factor determining the size of the penalty.

However, we also consider circuits which are more complex than the RF-SQUID circuit, but still contain repeating elements. In this case, we check that the current increases between any two successive points with increasing phase, guaranteeing monotonicity. Using the EOM for our circuit, we compute a grid of current values at 100 points for phase values between -6π and 6π. The penalty which enforces this is

$$\text{penalty} = \lambda\big(\tanh(-\Delta \mathrm{I}_{\mathrm{min}} - 0.1) + 1\big), \tag{106}$$

where ΔI_{min} is the minimum difference between sequential current values in the grid. This penalty varies smoothly from 0 to the maximum penalty λ, and it enforces the penalty when the minimum difference is negative, therefore favoring current-phase relations which are strictly increasing.

4.5 Performance of optimized JPA circuits

In this Section, we will examine JPA circuits which are optimized to a target gain of $G_{\text{t}} = 20$ dB, which is a common target in quantum computing applications. We will do so in both the degenerate and nondegenerate cases. In both cases, we optimize with a pump frequency $\omega_{\text{p}} = 12\ (2\pi)$ GHz, with $\omega_{\text{s}} = 0.5\,\omega_{\text{p}} = 6\ (2\pi)$ GHz in the degenerate case and $125/249\,\omega_{\text{p}}$ in the nondegenerate case. In optimizing our amplifiers, we treat pump power as a hyperparameter which is fixed for each optimization, and we adjust it to achieve the highest possible PAE. We will first investigate amplifiers whose inductive blocks are composed of RF-SQUIDs, where all circuit parameters as well as the damping rate K are optimized. Then, we investigate amplifier designs with higher PAE by shunting the RF-SQUIDs with three Josephson junctions with an applied current bias. This extended RF-SQUID circuit offers higher PAE at the expense of additional complexity, which may prove impractical to build. In addition to amplifier gain, we provide bandwidth and third order intercept point (IP3) characteristics for our nondegenerate amplifier designs.

4.5.1 RF-SQUID amplifiers

We find that by tuning the parameters of an amplifier composed of a chain of identical RF-SQUIDs as in Fig. 24, we can achieve a PAE which is a substantial fraction of the PAE of polynomial amplifiers. In Table 5, we list the circuit parameters for our optimized amplifiers. In particular, we tune the Josephson critical current i_{c}, the inductance L, the applied flux bias Φ_{ext}, and the damping rate K. In the degenerate case, we also tune the relative phase offset δ between the signal and pump.

parameter	degenerate RF-SQUID	nondegenerate RF-SQUID	degenerate extended RF-SQUID	nondegenerate extended RF-SQUID
P_{pump}	-72.3 dBm	-72.4 dBm	-72.2 dBm	-72.1 dBm
n	10	10	10	10
K	2.42 (2π) GHz	2.36 (2π) GHz	2.50 (2π) GHz	2.57 (2π) GHz
C	0.5 pF	0.5 pF	0.5 pF	0.5 pF
Z	131 Ω	135 Ω	127 Ω	124 Ω
i_{c}	18.8 μA	18.1 μA	–	–
i_{c1}	–	–	21.4 μA	20.3 μA
i_{c2}	–	–	-0.921 μA*	-3.32 μA*
L	17.5 pH	18.1 pH	15.3 pH	15.0 pH
L_1	–	–	399 pH	66.5 pH
Φ_{ext}	3.09 ϕ_0	3.09 ϕ_0	3.03 ϕ_0	3.09 ϕ_0
J_{ext}	–	–	4.65 μA	0.133 μA
δ	0.799π	–	0.876π	–
PAE	37.9%	8.9%	42.6%	14.2%

Table 5: Optimized amplifier circuit parameters. Degenerate RF-SQUID and nondegenerate RF-SQUID columns refer to circuits as shown in Fig. 24 and described in Subsec. 4.5.1, while degenerate extended RF-SQUID and nondegenerate extended RF-SQUID columns refer to circuits as shown in Fig. 25 and described in Subsec. 4.5.2.

*Junctions with negative Josephson critical currents should be replaced with DC-SQUIDs with appropriate flux bias which produce this equivalent negative i_{c}.

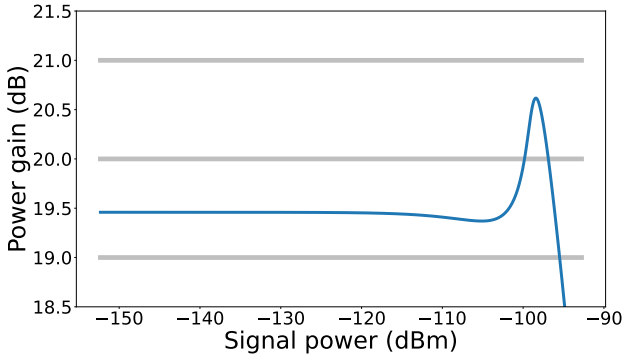

Figure 33: Gain versus input signal power of the degenerate RF-SQUID amplifier shown in Fig. 24, with optimized circuit tuned to 20 dB gain. Parameters for this amplifier are listed in Tab. 5.

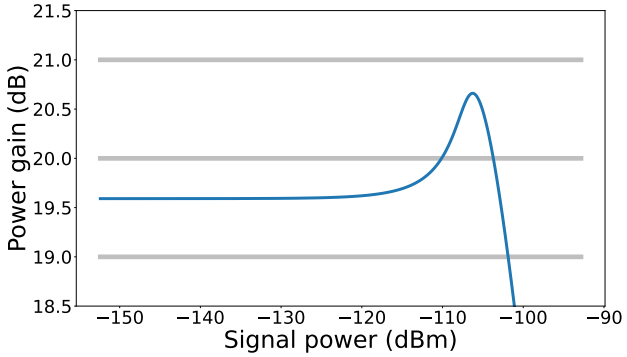

Figure 34: Gain versus input signal power of the nondegenerate RF-SQUID amplifier shown in Fig. 24, tuned to 20 dB gain. Parameters for this amplifier are listed in Tab. 5. The signal frequency is $\omega_s = 125/249\,\omega_p$.

In the degenerate case, we were able to optimize our amplifiers to a PAE of 37.9%. We plot the gain of this amplifier as a function of signal power in Fig. 33. In the nondegenerate case, we get a PAE of approximately 8.9%, with the gain curve shown in Fig. 34. These circuits have parameters as listed in Tab. 5. We note that our optimization is independent of the choice of capacitance C, and so our circuit elements, pump power, and characteristic

impedance Z can be rescaled by a different choice of C. In particular, inductances (e.g., L) are inversely proportional to C, while currents (e.g., i_c) and pump power, P_{pump}, are directly proportional to C. Here, we choose $C = 0.5$ pF and provide device parameters based on this choice. Our amplifiers are optimized with a low relative pump power (such that $(P_{\text{pump}})/(n^2 C K \phi_0^2 \omega_{\text{p}}^2)$ is small), as we find this improves PAE. Higher output saturation power can be achieved without changing PAE by rescaling parameters as described above.

4.5.2 Extended RF-SQUID amplifiers

Here, we investigate amplifiers with inductive blocks composed of RF-SQUIDs shunted by three Josephson junctions in series with an applied current bias, as well as a separate flux bias through the RF-SQUID loop, as shown in Fig. 25. With these extended RF-SQUID designs, we can achieve a PAE which is higher than that of the RF-SQUID amplifiers above by more carefully tuning higher order terms in the current-phase relation of the inductive block of the amplifier. This is possible due to the introduction of three new tuning parameters, $J_{\text{ext}}, i_{\text{c2}}$, and L_1 (where here the single Josephson junction's critical current is renamed from i_{c} to i_{c1}).

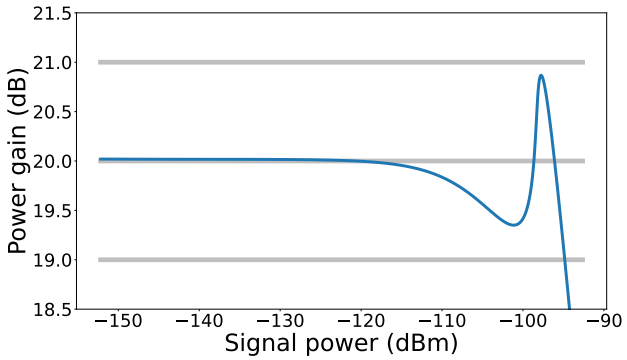

Figure 35: Gain versus input signal power of the degenerate extended RF-SQUID amplifier shown in Fig. 25, with optimized circuit tuned to 20 dB gain. Parameters for this amplifier are listed in Tab. 5.

Parameter values that optimize this circuit for 20 dB gain can be found in Tab. 5. We provide parameters for both the degenerate and nondegenerate cases, with their respective

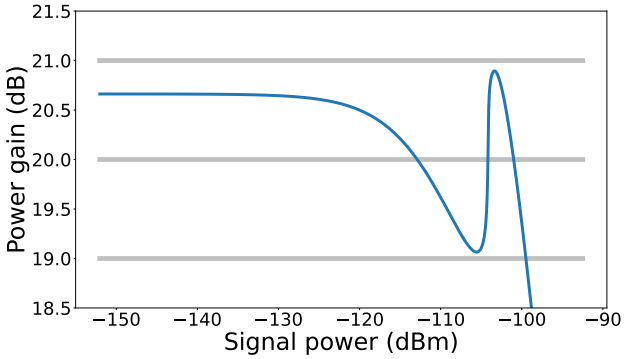

Figure 36: Gain versus input signal power of the nondegenerate extended RF-SQUID amplifier shown in Fig. 25, with optimized circuit tuned to 20 dB gain. Parameters for this amplifier are listed in Tab. 5. The signal frequency is $\omega_s = 125/249\,\omega_p$.

gain curves plotted in Fig. 35 and Fig. 36. The PAE of the degenerate amplifier is approximately 42.6%, while that of the nondegenerate amplifier is 8.9%.

4.5.3 Bandwidth and third order intercept point

Bandwidth is an important measure of amplifier performance due to the need to amplify signals over a range of frequencies. For the amplifiers in Subsec. 4.5.1, we find a bandwidth of 327 MHz. The large bandwidth is a consequence of the high damping rate of about 2.5 (2π) GHz. We plot the gain of the nondegenerate amplifier over a range of frequencies in Fig. 37(a), demonstrating this bandwidth. The gain versus signal frequency plot for the nondegenerate amplifier described in Subsec. 4.5.2 is shown in Fig. 37(b), with a bandwidth of 375 MHz.

Another measure of amplifier performance is IP3, which indicates the range of signal power over which intermodulation products between two distinct signal frequencies remain small. Here, we compute the output power of third order intermodulation products resulting from the amplification of two similar but distinct signal frequencies within the amplifier bandwidth. We note that in order to reduce computation run time, we slightly modify the procedure in Subsec. 4.2.3 to use the last half of the DTI solution rather than the last quarter,

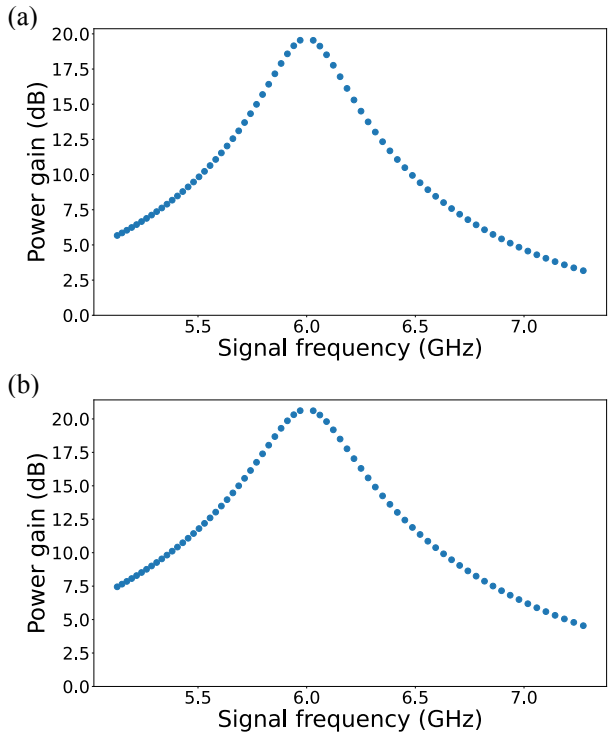

Figure 37: Amplifier bandwidth: gain of the nondegenerate amplifier versus signal frequency. (a) Amplifier in Subsec. 4.5.1. (b) Amplifier in Subsec. 4.5.2.

while ensuring the integration time remains at least 2000 periods of the signal frequencies. This allows us to choose an integration time which is twice T_{min} rather than 4 times T_{min}. This reduced integration time does not affect our solution since for the two similar signal frequencies used in IP3 analysis, the integration time is very long and transient solutions die out far before half the integration time.

We provide a diagram of the output power of our two signals as well as third order products in Fig. 38(a), which demonstrates the IP3 performance of the amplifier in Subsec. 4.5.1. As anticipated, the output signal power grows linearly with input signal power, while the third order terms grow cubically until the saturation point. We find input third order intercept point (IIP3) of -95.0 dBm and output third order intercept point (OIP3) of -78.9 dBm. Similarly, in Fig. 38(b), we provide the IP3 performance of the amplifier in

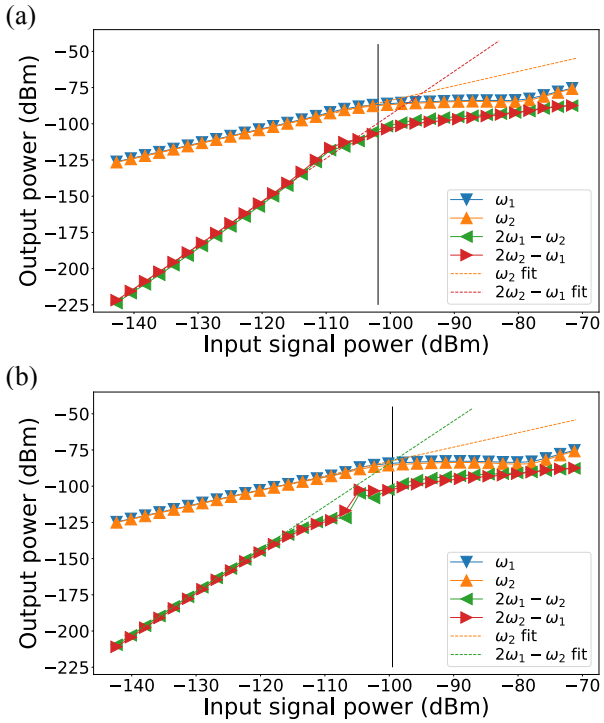

Figure 38: IP3: output power of signal frequencies as well as their third order intermodulation products, plotted in dBm units. Input signal power refers to the total input power from both signals. Here we have $\omega_1 = 101/201\,\omega_\mathrm{p}$ in blue and $\omega_2 = 101/200\,\omega_\mathrm{p}$ in orange. The third order term $2\omega_1 - \omega_2$ is in green and $2\omega_2 - \omega_1$ is in red. We include fits for ω_2 (dashed orange, which is the lower of the linear components), and $2\omega_2 - \omega_1$ (dashed red, panel (a), which is the higher of the cubic components) and $2\omega_1 - \omega_2$ (dashed green, panel (b), which is the higher of the cubic components) which demonstrate the intercept points. These fits take into account the 3rd through 10th points of each data set. The black lines represent the input saturation power as determined by our requirement that the input signal be amplified by 20 dB $\pm$ 1 dB. (a) Amplifier in Subsec. 4.5.1. (b) Amplifier in Subsec. 4.5.2.

Subsec. 4.5.2, where we find IIP3 of -99.2 dBm and OIP3 of -82.2 dBm. In each diagram, the black vertical line represents the input saturation power, demonstrating that the third order intermodulation products remain substantially smaller than the output signals up to this point. For further analysis of intermodulation products and a full power spectrum near

the saturation point, see Appendix 4.7.2.

4.6 Summary

Due to the limited power added efficiency of modern JPAs and the need for low noise, efficient amplifiers in quantum computing applications, we have explored optimizing JPA designs by finely tuning the amplifier's inductive block. We find that with the freedom to more carefully define the inductive block, we can design amplifiers with a PAE orders of magnitude higher than that of modern JPAs. In particular, modern JPAs currently in use are tuned so as to optimize third order nonlinearity. These intrinsic third order terms dynamically generate higher order nonlinearities, which shift signal and idler modes off resonance [68]. For example, the g_3 term in Eq. (87) generates a response at zero frequency and twice the signal frequency which is quadratic in signal amplitude. This in turn generates a cubic response at the signal frequency, which looks like the g_4 term of Eq. (87). Here, we counter this effect by tuning intrinsic higher order nonlinearities in order to cancel the dynamically generated nonlinearities.

Considering inductive blocks composed of linear inductors and Josephson junctions, we identify a rule for designing JPAs. In particular, we find that the inductive block should have a monotonic current-phase relation to avoid issues with how phase divides among elements in the block. Further, considering inductive blocks consisting of circuits extending previous RF-SQUID designs with monotonic current-phase relations, we still realize a significant improvement in PAE. We are able to design JPA circuits with high PAE, large bandwidth, and limited intermodulation distortion. In particular, we provide designs for amplifiers based on chains of RF-SQUIDs with high PAE, and provide designs with chains of extended RF-SQUIDs with even higher PAE at the expense of manufacturing complexity. In Appendix 4.7.3, we discuss the robustness of these designs to small manufacturing imperfections.

These amplifiers could prove to be useful in quantum computing applications which require the amplifier to be located in proximity to qubits at millikelvin temperatures, where

minimizing heat dissipation is a priority. Recent implementations of low PAE, high saturation power amplifiers are problematic [85, 55] due to the extremely high pump powers utilized in these experiments, which in turn generate excessive heat in the cryostat. Compared to those previous JPA designs, the amplifiers in this Chapter are able to provide similar output signal power while requiring a substantially weaker pump, thereby reducing heat load. These high saturation power and high PAE amplifiers may be particularly advantageous in scenarios where simultaneous multiplexed qubit readout is necessary, as the power requirement scales with the number of qubits. Additionally, these amplifiers demonstrate low distortion at low signal power, which provides a significant benefit in using high saturation power amplifiers as compared to low saturation power amplifiers [13, 102]. We anticipate many, or at least several, of these devices to be mounted in a single dilution refrigerator, which would help to scale up superconducting quantum computing systems which may otherwise be limited to a relatively small number of qubits. We have published the results in this Chapter, which can be referred to in Ref. [50].

In the future, this work could serve as a basis on which to explore circuits which may more easily be manufactured and used in superconducting quantum computing systems. In particular, these optimizations can be performed on circuits which account for realities of manufacturing such as parasitic inductances and variation of parameters associated with the fabrication of physical circuits. We are currently working in conjunction with the Hatlab to design circuits of this kind. Specifically, we are re-optimizing our RF-SQUID amplifiers with the modification that the branch with the Josephson junction also has a linear inductance in it which accounts for the parasitic inductance present in real circuits. This inductance would not be an optimization parameter, but would affect the optimized values of the remaining circuit elements which are again found via our optimization algorithm to maximize PAE. We are also taking into account tolerance to fabrication variability right at the design stage. We hope this effort will result in buildable circuits which can be used by the Hatlab.

Even beyond quantum computing, low-noise amplification has many applications in science and engineering. Low-noise amplifiers are useful in radio astronomy as the signals being detected are often very small [104]. Similar constraints on amplifier noise exist in applications such as communication [73], sensing [31], and spectroscopy [57]. The work in this Chapter

lays a foundation for designing efficient, low-noise amplifiers in the microwave domain which could be useful for applications in these fields, or any field where there is a need to amplify small signals while adding little noise.

Beyond small modifications to the circuits laid out in the Chapter, further improvements to JPAs may be possible based on this work. We could consider adjusting the cost function used to optimize these circuits in order to identify a broader local maximum of PAE in the space of circuit parameters. I.e., we could design a circuit which has high PAE and is more resilient to manufacturing offsets in the targeted circuit parameters. Alternative amplifier designs are also possible, and could include amplifiers with power gain of 30 dB or higher, which may obviate the need for later-stage amplification with a HEMT at higher temperature. The platform for optimizing JPAs laid out in this Chapter open the possibility for more careful design of amplifier circuits, with many viable design goals.

4.7 Appendix

4.7.1 Numerical solution and optimization of JPA circuits

In solving the EOMs for a circuit of the form described in Fig. 23, we use the DTI method described in Section 4.2.3 to compute the output signal from the amplifier. We use a total integration time that is commensurate with the period of the pump and signal frequencies. That is, we enforce that the integration time must be a multiple of $T_{\min} = \mathrm{lcm}(\frac{2\pi}{\omega_\mathrm{p}}, \frac{2\pi}{\omega_\mathrm{s}})$. We choose an integration time of $4n_cT_{\min}$ since we wish to isolate the steady-state solution to the equations of motion, while at time near $t = 0$ we see a transient solution to the differential equations. We choose n_c such that the integration time represents at least 2000 periods of both the signal and pump. We take only the last quarter of the DTI solution, which we find is sufficient to remove transient effects from the output signal. To see that the transient solution quickly dissipates, we provide examples of the time-domain output signal computed via DTI for amplifiers with inductive blocks composed of a chain of 10 RF-SQUIDs. These examples, shown in Fig. 39, demonstrates that the transient solution gives

way to the steady-state in the long-time regime for amplifiers with inductive blocks with monotonic current-phase relations. For those with nonmonotonic current-phase relations, the integrated solution does not become periodic. Since we only select the last quarter of our DTI solution, and only propose amplifiers with inductive blocks monotonic current-phase relations, we avoid including transient effects in analyzing the output of these amplifiers. In order to extract the power of the amplified signal frequency, we use the DFT with 50 samples of the DTI solution per signal period.

In order to begin the optimization procedure, we must choose initial parameters for the JPA circuit elements and for ϕ_{in}. Initial amplifier designs were based on the RF-SQUID design shown in Fig. 24, for which L and i_{c} were chosen in order to design a $\omega_{\text{s}} = 6\ (2\pi)$ GHz amplifier. Then, the pump amplitude A_{p} is chosen such that for small signal amplitude, the gain of the amplifier is 20 dB. Our circuit designs all represent extensions of this RF-SQUID design with additional shunting with Josephson junctions and with applied current bias.

We then apply the optimization procedure described in Section 4.2.3 with circuit parameters and damping rate K, as variables. With this procedure, we find optimal circuit parameters which minimize deviations of the gain from 20 dB, and which consequently improve the PAE.

4.7.2 Power Spectrum of Nondegenerate Amplifier Near Gain Compression Point

Here we investigate the power spectrum of the nondegenerate RF-SQUID amplifier when used to amplify two signals near the saturation point. This serves to identify the behavior of other intermodulation products in addition to the third order terms which are relevant in IP3 analysis. We provide the output power spectrum of the band with focus on the frequencies near the signal and pump tones, as well as $\omega_{\text{p}} + \omega_{\text{s}}$, in Fig. 40. That is, we can investigate intermodulation products around 6 GHz, 12 GHz, and 18 GHz.

The highest peak in the spectrum is the pump tone at 12 GHz, while the two signals and their idlers on either side of 6 GHz follow. The next largest components, the third order products plotted in Fig. 38 and the second order terms at $\omega_{\text{p}} + \omega_{\text{s}}$, remain a factor of at

least 21 below the two signal tones. We therefore believe intermodulation products remain manageable up to saturation power, and we note that the saturation point is reached not because of pump power being consumed by these intermodulation products, but because of fundamental limits to the amplifier's ability to amplify at the signal frequency.

4.7.3 Tolerance of amplifier performance to variations in circuit parameters

The JPA circuit designs provided in this Chapter and their predicted PAE are derived by considering ideal circuits, where repeating blocks are able to be manufactured identically and with no variation in parameters. We consider here how the performance of the degenerate RF-SQUID amplifier specified in Table 5 is affected by variations in the fluxes through each of the 10 loops in our circuit. To do this, we simulate the circuit with intermediate nodes and stray capacitances as in Sec. 4.4.2. In particular, we simulated the RF-SQUID amplifier circuit with 10 equations of motion, where each equation corresponds to a single RF-SQUID, and the flux through each SQUID's loop is varied. Since this is a computationally difficult problem, we computed amplifier performance for a single set of fluxes which varied from the optimized flux by a random amount selected via a normal distribution. We increased the standard deviation of this distribution to test the effect of increasing variations on amplifier performance.

We find that when adding variations to the flux through the loop, we must adjust the pump power to maintain our 20 dB target gain in the low signal regime. In Fig. 41, we show gain versus signal amplitude for varying standard deviation of the fluxes without adjusting pump power. The gain at low signal amplitude quickly leaves the 20 dB $\pm$ 1dB region, as indicated by the black horizontal lines.

We then consider decreasing the pump power for different amounts of flux variation to return to our 20 dB $\pm$ 1dB regime and recompute PAE. We find that for a standard deviation of $0.003\phi_0$, we are able to retain a PAE of at least 34.3% (Fig. 42(a)), as compared to 37.9% without the added flux variations. That is, with this level of variation in flux, we lose only a marginal amount of efficiency. Increasing the standard deviation to $0.005\phi_0$, we find a PAE of at least 11.3% (Fig. 42(b)). For a standard deviation of $0.01\phi_0$, the PAE is at least 8%

(Fig. 42(c)). Therefore, for this JPA circuit design, it is ideal to keep variations in threaded flux below $0.003\phi_0$ to $0.005\phi_0$.

Another possible manufacturing defect is a uniform offset of a device parameter from the ideal value described in this Chapter. In practical use, the ideal operating point of an amplifier is determined by adjusting both pump power and frequency so as to maximize PAE. In order to demonstrate how this can mitigate uniform manufacturing defects, we consider the case of our degenerate RF-SQUID circuit specified in Table 5 with a decrease of 1%, 3% and 5% of the linear inductances from their ideal values. We adjust the pump power and signal/pump frequency together in order to achieve the highest possible PAE under these defects, as compared to 37.9% with no defects. With 1% offset, we find that the PAE can be restored to at least 33.0%, with 3% offset, we can achieve at least 20.8% PAE, and with 5% offset, we can achieve at least 9.2% PAE. We provide the gain versus input signal power in these three cases in Fig. 43. We therefore find that it is possible to recover amplifier performance in practical amplifiers which are subject to the limitations of manufacturing precision.

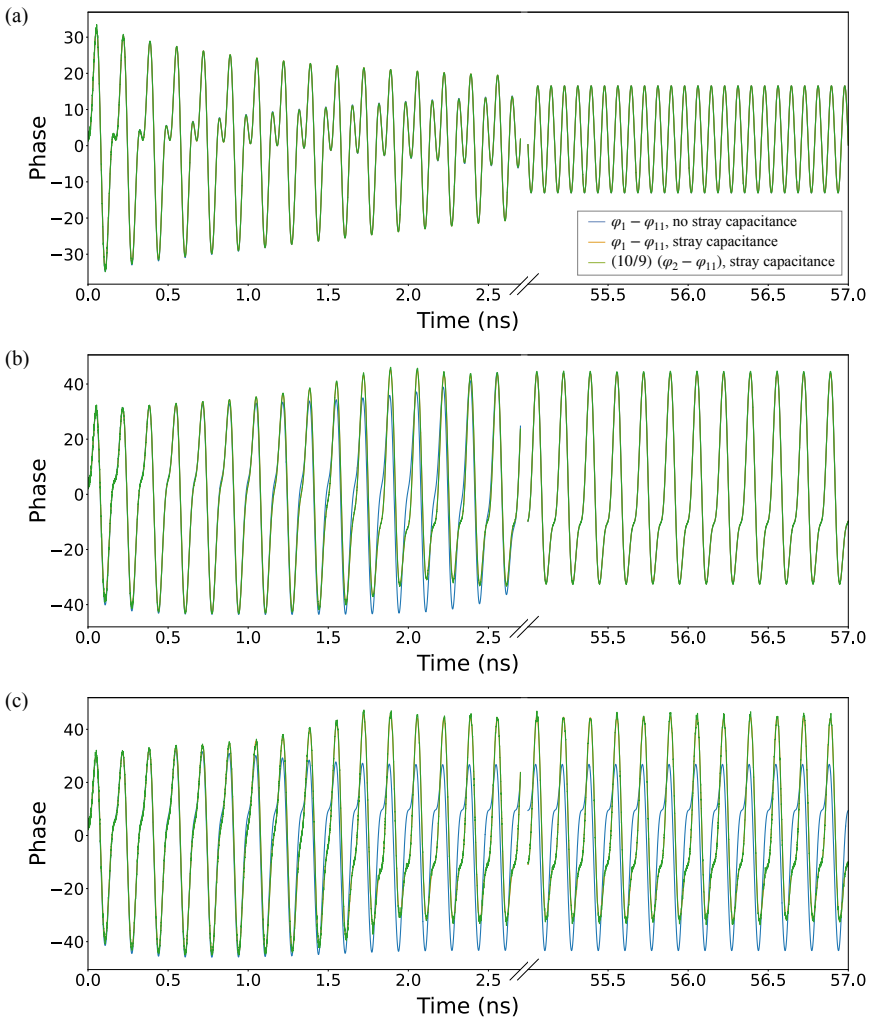

Figure 39: Example time-domain output signals computed by DTI for amplifiers with 10 RF-SQUIDs. In each panel, we plot the signal for short-time, demonstrating the transient behavior, and for long-time, demonstrating the steady-state behavior. (a) Amplifier with inductive block whose current-phase relation is very monotonic, i.e. its slope is never near zero. In this case, we see the initial transient behavior, and then the steady state behavior, with agreement among simulations with and without stray capacitances, and at intermediate phases. (b) Amplifier with inductive block whose current-phase relation is nearly nonmonotonic, i.e. it is monotonic but its slope nears zero. Here, we see transient behavior, but the steady state settles with agreement among simulations. (c) Amplifier with inductive block whose current-phase relation is nonmonotonic. In this case, the amplifier never settles, behavior is not periodic even in the long-time regime, and the simulations do not agree.

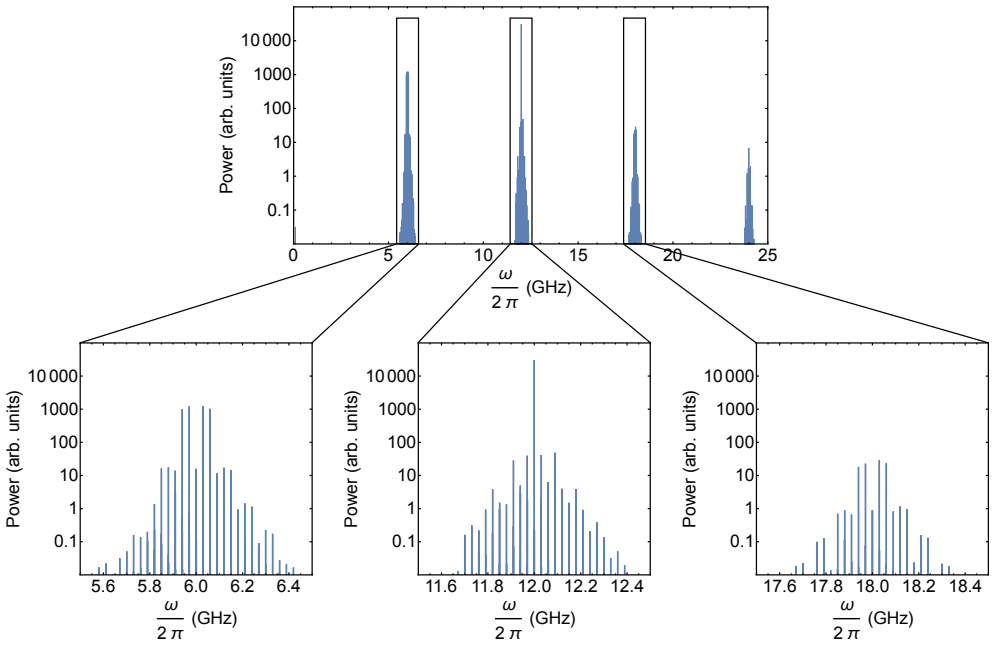

Figure 40: Fourier analysis of the output of the nondegenerate RF-SQUID amplifier near the saturation point. Here we have the two signal frequencies $\omega_1 = 101/201\,\omega_\mathrm{p}$ and $\omega_2 = 101/200\,\omega_\mathrm{p}$, which are given the same input power (-105.9 dBm). The top portion of the figure shows the spectrum of the full band, from 0 GHz to 25 GHz. We provide further detail of the power spectrum around 6 GHz, 12 GHz, and 18 GHz, which shows the vicinity of the signal frequencies and the pump frequency, as well as second order terms which mix pump and signal. The two peaks just above 6 GHz represent the two signals which are approximately 1 to 2 orders of magnitude higher than the next highest products (except their idlers, which are approximately equal), and are lower than only the pump tone at 12 GHz.

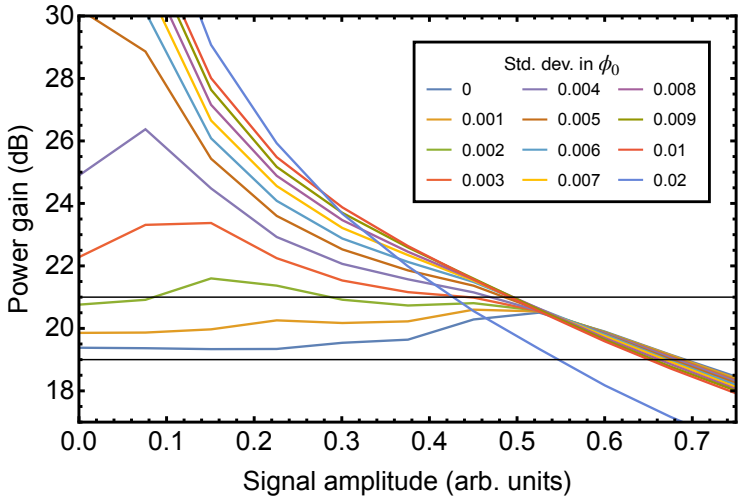

Figure 41: Gain versus signal amplitude for different amounts of variation in the external flux through each RF-SQUID loop. In the low signal amplitude regime, increasing the variation increases gain, leaving the desired ±1 dB region. For higher signal amplitudes, the performance tends to be less sensitive to variations in flux.

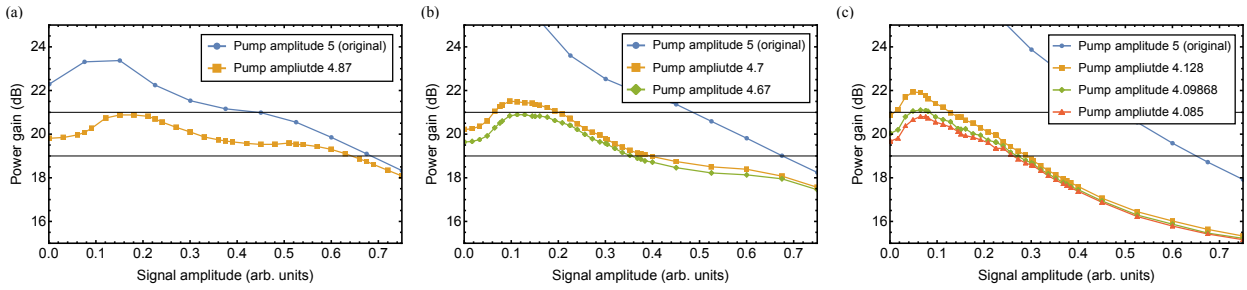

Figure 42: Gain versus signal amplitude for select amounts of variation in external flux. We reduce signal power gradually to re-enter the ±1 dB region. (a) Variations with standard deviation of $0.003\phi_0$. (b) Variations with standard deviation of $0.005\phi_0$. (c) Variations with standard deviation of $0.01\phi_0$.

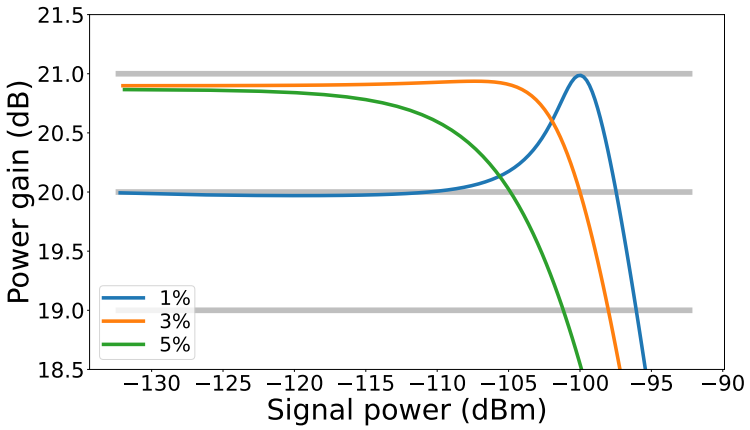

Figure 43: Gain versus input signal power for 1%, 3%, and 5% decreases in the linear inductances in the degenerate RF-SQUID amplifier. The pump power and pump/signal frequencies have been adjusted to recover PAE. As compared to the original design, in the 1% case the pump and signal frequencies are increased by 1.4% and the pump power is -72.2 dBm. For the 3% offset, the frequencies are increased by 3.7% and the pump power is -71.9 dBm. For the 5% offset, the frequencies are increased by 5% and the pump power is -71.5 dBm.

5.0 Micromaser theory

5.1 Introduction

The word maser is an acronym that stands for microwave amplification by stimulated emission of radiation. The maser is the microwave equivalent of the laser. Just like a laser, a maser takes incoherent pump light and converts it to coherent output light, where the output light is at optical frequencies for lasers and microwave frequencies for masers. The theory of the maser was developed in 1952 by Basov, Prokhorov, and Weber. The first maser light was produced by Townes, Gordon, and Zeiger at Columbia University in 1953, seven years before the first laser was made at Hughes Research Lab by Maiman based on the theory of Townes and Schawlow. A micromaser is a maser which is composed of a single-atom coupled to a masing cavity field. First proposed by Filipowicz, Javanainen, and Meystre [37], such devices allow for a detailed study and probing of the atom-cavity interaction [99]. In particular, the theory of micromasers raises the possibility of tuning the atom-cavity coupling so as to achieve favorable masing properties such as lower linewidth.

Narrow linewidth is an important property of masers for applications in quantum information and optics. Schawlow and Townes introduced the standard quantum limit (SQL) on maser linewidth [97], which says that the linewidth minimum is proportional to the cavity linewidth divided by the average photon population of the cavity. Previous work has shown that by engineering the atom-cavity coupling (and cavity-output coupling), it is possible to reduce maser linewidth below this limit [116, 65], possibly such that the maser linewidth is proportional to $\langle n \rangle^{-2}$, which is known as the Heisenberg limit [5].

The Hatlab has developed a micromaser system where the gain medium is an artificial atom composed of superconducting quantum circuit components. The experimental setup allows for an artificial atom which can be pumped into a population inverted state, and the coupling between this artificial atom and the masing cavity can be tuned by designing alternative, nonlinear atom-cavity coupling circuits.

In this section, we will begin by considering the experimental setup of the Hatlab mi-

cromaser and discuss the transitions we believe play an important role in the output of the maser. We will then model this micromaser by writing the Hamiltonians of each component of the masing system and using this to write a master equation for the maser. We will use this to determine the maser brightness as it varies with atom frequency and pump strength. Finally, we will discuss the theory underlying a system composed of an atom coupled to a cavity field and investigate how maser linewidth depends on the atom-cavity coupling.

5.2 Theory of operation of micromasers composed of nonlinear superconducting components

The artificial atom in our micromaser (see Fig. 45) is composed of a SNAIL qubit (henceforth referred to as simply the SNAIL) coupled to a transmon qubit. The artificial atom is coupled to the masing cavity which itself is coupled to the output channel. The artificial atom is set up such that the SNAIL has a short lifetime while the transmon has a much longer lifetime. For describing the artificial atom we use the $|\text{SNAIL}, \text{transmon}\rangle$ basis while for describing the whole maser we use the $|\text{SNAIL}, \text{transmon}, \text{cavity}\rangle$ basis. To make state labels easier to read we use $g, e, f, ...$ to label the photon number states of the transmon and $0, 1, 2, ...$ to label the photon number states of the SNAIL and of the cavity. E.g. the state $|0e5\rangle$ has no photons in the SNAIL, one photon in the transmon, and five photons in the cavity.

We will describe several schemes for achieving population inversion and running the maser. In the simplest scheme, we pump from the ground state of the system to the $|1e\rangle$ state of the artificial atom. This transition is made possible by the cubic nonlinearity of the SNAIL, which converts one pump photon into one SNAIL and one transmon photon. Because of the large loss in the SNAIL, the state quickly decays to the $|0e\rangle$ state, resulting in population inversion. In this scheme, due to the anharmonicity of the transmon, we do not populate further excited states of the transmon. We then tune the transmon such that its first excited state is on resonance with the masing cavity level spacing. We can pump the cavity by continuously driving the artificial atom to the population inverted state and thus

achieve masing.

By tuning the transmon and pump frequencies, it is also possible to achieve masing where population inversion occurs in different states. The masing scheme described above involves photon transfer to the cavity by the $|0e\rangle \rightarrow |0g\rangle$ transition of the artificial atom, as depicted in Fig 44(a). The first alternative scheme involves masing via the $|0f\rangle \rightarrow |0e\rangle$ transition that is activated by (a) modifying the pump to achieve population inversion in the $|0f\rangle$ state and (b) by making $|0f\rangle \rightarrow |0e\rangle$ transition resonant with the level spacing of the cavity, as in Fig. 44(b). The second alternative masing scheme activates a two-photon process associated with the $|0f\rangle \rightarrow |0g\rangle$ transition of the artificial atom. To activate this transition, the cavity level spacing must be resonant with $(E_{|0f\rangle} - E_{|0g\rangle})/2$, shown in Fig. 44(c).

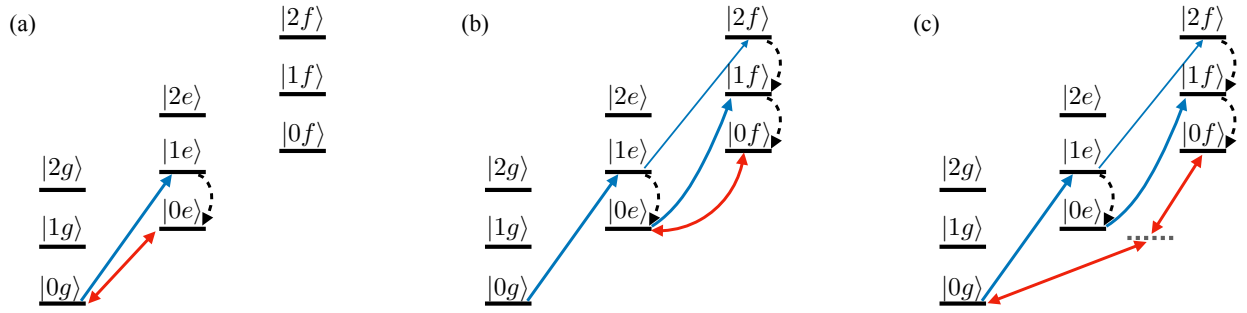

Figure 44: Diagram of levels in the SNAIL-transmon subsystem. Blue arrows represent couplings due to the parametric pump, black dashed arrows show relaxation of the SNAIL, and red arrows indicate cavity-atom coupling. (a) Masing mediated by the transition between the transmon's first excited state and ground state. (b) Masing mediated by the transition between the transmon's second excited state and first excited state. (c) Masing mediated by the transition between the transmon's second excited state and ground state.

5.3 Simulating micromaser system with cQED

In this section, we present our description of the maser system, which relies on circuit QED methods to obtain an approximate master equation for the three main components of

the system (SNAIL, transmon, and cavity) followed by eigenanalysis of the resulting equation to find the steady state solution as well as maser linewidth. We start by writing the Hamiltonian of each component separately in terms of dimensionless superconducting phase variables φ_s, φ_t, and φ_c for the SNAIL, transmon, and cavity (see Fig. 45). Next, we discretize the phase variables to obtain a Schrödinger equation, in matrix form, for each component. We verify that the low-energy eigenspectrum of each of our Schrödinger equations is insensitive to the discretization scheme and then we use the resulting low-energy spectrum as a basis to describe each of the components. We construct the complete Hamiltonian for the system using the resulting basis states by combining the diagonal Hamiltonians for each of the components, the discrete representations of the SNAIL-transmon and transmon-cavity coupling Hamiltonians, and the SNAIL pump Hamiltonian. Next, we hybridize the SNAIL and transmon to obtain the Hamiltonian of the artificial atom that is coupled to the cavity. The artificial atom-cavity basis allows us to construct an approximate master equation for the maser by (a) introducing the Lindbladian loss terms for each component as prescribed by Ref. [86] and (b) considering only the most relevant couplings induced by the pump. Through eigenanalysis of the time evolution superoperator, we compute the population of the maser states and the maser linewidth.

We note that the approach that we follow for constructing the basis states and Hamiltonians of the SNAIL and transmon is in contrast to the commonly used approach of expressing the Hamiltonians in terms of quadratic, cubic, and quartic terms composed of creation and annihilation operators. The reason we go to the trouble of constructing basis states of individual components is that this approach allows for the full, nonlinear description of the quantum states of each component, and as a result we can obtain low-energy basis states that are insensitive to the Hilbert space truncation scheme. On the other hand, quadratic, cubic, and quartic approximations of the Hamiltonians are not very accurate and as a result the eigenspectra obtained using them are strongly dependent on how the Hilbert space is truncated. Indeed, as the quartic term is usually negative, the spectrum of the approximate Hamiltonians becomes unbounded from below as we include more and more photon number states in the Hilbert space. In the method that we outlined above, we begin from the circuit QED description of the maser components and the truncation is done in the photon number

basis after taking into account the full nonlinearity of the component. The combination of the strong nonlinearity of the transmon and the fast decay of the SNAIL implies that neither needs to be modeled with a basis of more than 5 photon states. We have confirmed this notion by verifying that the maser populations in the steady state do not vary significantly upon increasing the basis size of the SNAIL and transmon beyond 5 photons each. We also confirm from our simulation that the higher states of these components have extremely low occupation (below 10^{-9}).

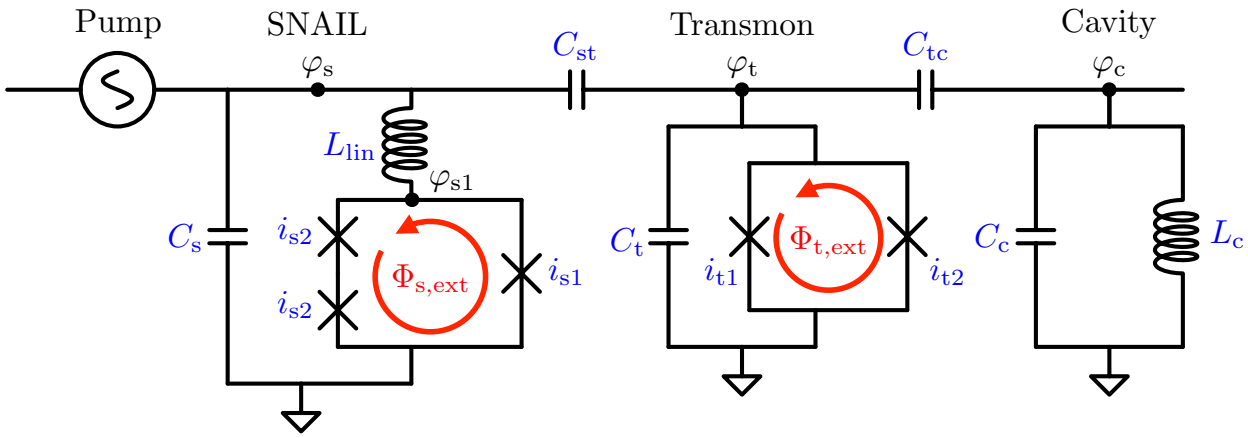

Figure 45: Diagram of the maser circuit including the pump, SNAIL, transmon, cavity.

We start modeling this system, using circuit QED methods [44], by writing the (classical) Hamiltonian of each of these three components (SNAIL, transmon, and cavity). The circuit for this system is shown in Fig. 45, showing each of these components. We can write the Hamiltonian for the components as follows:

$$\begin{aligned} H_s &= \frac{1}{2}C_s\dot{\varphi}_{s1}^2 - \phi_0 i_{s1}\cos(\varphi_{s1} + \Phi_{s,\,ext}) \\ &\quad - 2\phi_0 i_{s2}\cos(\varphi_{s1}/2) + \frac{1}{2L_{lin}}(\varphi_s - \varphi_{s1})^2, \end{aligned} \tag{107}$$

$$H_t = \frac{1}{2}C_t\dot{\varphi}_t^2 - \phi_0 i_{t1}\cos(\varphi_t + \Phi_{t,\,ext}) - \phi_0 i_{t2}\cos(\varphi_t), \tag{108}$$

$$H_c = \frac{1}{2}C_t\dot{\varphi}_c^2 + \frac{1}{2L_c}\varphi_c^2, \tag{109}$$

where C_α represent capacitances, L_β represent inductances, i_γ represent Josephson critical currents, $\Phi_{\delta,\text{ext}}$ represent external magnetic fluxes, and φ_ϵ represent dimensionless super-

conducting order parameter phase at the nodes of the circuit shown in Fig. 45. We define $\varphi_\epsilon = \phi_\epsilon/\phi_0$, where $\phi_0 = \frac{\hbar}{2e}$ is reduced magnetic flux quantum and ϕ_ϵ is the flux.

For the capacitive couplings between the components, we write the coupling Hamiltonians:

$$H_{\rm st} = \frac{1}{2}C_{\rm st}(\dot{\varphi}_{\rm s} - \dot{\varphi}_{\rm t})^2 \tag{110}$$

$$H_{\rm tc} = \frac{1}{2}C_{\rm tc}(\dot{\varphi}_{\rm t} - \dot{\varphi}_{\rm c})^2. \tag{111}$$

Note that each of these coupling Hamiltonians includes terms which act on only a single component of the system, i.e. $\dot{\varphi}_{\rm s}^2, \dot{\varphi}_{\rm t}^2, \dot{\varphi}_{\rm c}^2$. We treat these terms as part of the single-component Hamiltonians, leaving only the cross terms in the coupling Hamiltonians.

$$\tilde{H}_{\rm s} = H_{\rm s} + \frac{1}{2}C_{\rm st}\dot{\varphi}_{\rm s}^2 \tag{112}$$

$$\tilde{H}_{\rm t} = H_{\rm t} + \frac{1}{2}(C_{\rm st} + C_{\rm tc})\dot{\varphi}_{\rm t}^2 \tag{113}$$

$$\tilde{H}_{\rm c} = H_{\rm c} + \frac{1}{2}C_{\rm tc}\dot{\varphi}_{\rm c}^2 \tag{114}$$

$$\tilde{H}_{\rm st} = C_{\rm st}\dot{\varphi}_{\rm s}\dot{\varphi}_{\rm t} \tag{115}$$

$$\tilde{H}_{\rm tc} = C_{\rm tc}\dot{\varphi}_{\rm t}\dot{\varphi}_{\rm c}. \tag{116}$$

Finally, we introduce quantum momentum operators by inverting the capacitance matrix

$$\begin{pmatrix} C_{\rm s} + C_{\rm st} & C_{\rm st} & 0 \\ C_{\rm st} & C_{\rm t} + C_{\rm st} + C_{\rm tc} & C_{\rm tc} \\ 0 & C_{\rm tc} & C_{\rm c} + C_{\rm tc} \end{pmatrix} \tag{117}$$

for the system. Using the inverse of the capacitance matrix, to first order in the couplings

$$\begin{pmatrix} \frac{1}{C_{\rm s}} - \frac{C_{\rm st}}{C_{\rm s}^2} & -\frac{C_{\rm st}}{C_{\rm s}C_{\rm t}} & 0 \\ -\frac{C_{\rm st}}{C_{\rm s}C_{\rm t}} & \frac{1}{C_{\rm t}} - \frac{C_{\rm st}+C_{\rm tc}}{C_{\rm t}^2} & -\frac{C_{\rm tc}}{C_{\rm t}C_{\rm c}} \\ 0 & -\frac{C_{\rm tc}}{C_{\rm t}C_{\rm c}} & \frac{1}{C_{\rm c}} - \frac{C_{\rm tc}}{C_{\rm c}^2} \end{pmatrix} \tag{118}$$

we write down the kinetic energy terms of the quantum Hamiltonian for the system

$$T_{\mathrm{s}} = -\frac{1}{2}\left(\frac{1}{C_{\mathrm{s}}} - \frac{C_{\mathrm{st}}}{C_{\mathrm{s}}^2}\right)\partial_{\mathrm{s}}^2 \tag{119}$$

$$T_{\mathrm{t}} = -\frac{1}{2}\left(\frac{1}{C_{\mathrm{t}}} - \frac{C_{\mathrm{st}} + C_{\mathrm{tc}}}{C_{\mathrm{t}}^2}\right)\partial_{\mathrm{t}}^2 \tag{120}$$

$$T_{\mathrm{c}} = -\frac{1}{2}\left(\frac{1}{C_{\mathrm{c}}} - \frac{C_{\mathrm{tc}}}{C_{\mathrm{c}}^2}\right)\partial_{\mathrm{c}}^2 \tag{121}$$

$$T_{\mathrm{st}} = \frac{C_{\mathrm{st}}}{C_{\mathrm{s}}C_{\mathrm{t}}}\partial_{\mathrm{s}}\partial_{\mathrm{t}} \tag{122}$$

$$T_{\mathrm{tc}} = \frac{C_{\mathrm{tc}}}{C_{\mathrm{t}}C_{\mathrm{c}}}\partial_{\mathrm{t}}\partial_{\mathrm{c}}. \tag{123}$$

For each of the SNAIL, transmon, and cavity, we solve the Schrödinger equation to derive its eigenstates, and use these eigenstates as a basis to construct a Hamiltonian for the complete system. To do so, we discretize the phase variable and solve the resulting difference equations numerically (see Appendix 5.6.1 for more details). This is accomplished by constructing the matrices for the Hamiltonian of each component in Mathematica. The appendix shows how we can write the matrices for derivative operators using partial differences, and the potential energy terms can be written in this matrix form by evaluating the potential energies at the discretized values of phase we choose. Note that for the transmon and cavity, the phase Hamiltonian of each is dependent directly on the phase variable φ_{t} and φ_{c} directly. However, the SNAIL has the additional internal phase φ_{s1} which determines how the phase φ_{s} is divided between the SNAIL loop and a stray linear inductance L_{lin}. Handling of this internal phase and fitting the SNAIL to experimental data is discussed in Appendix 5.6.2.

The energies of the eigenstates of each component can be used to produce a Hamiltonian using photon number in each component as a basis. We get these energies and eigenstates by using the Eigensystem[] solver in Mathematica. For building the Hamiltonian of these components, we are not yet taxing the limits of our computational resources, and so the method of solving the system is not of deep importance. At later steps in this process, we will use a method of solving for eigenstates of the system which optimizes for our use case. Then, the cross terms in the coupling Hamiltonians can also be constructed using these eigenstates by computing matrix elements for the $\tilde{H}_{\mathrm{st}}$ and $\tilde{H}_{\mathrm{tc}}$ terms, which can be done

independently for each component since the operators for each component commute. That is, we can compute the matrix elements which go into the the coupling Hamiltonians in this basis as

$$\langle \Psi_{j,n} | \, \partial_{\varphi,j} \, | \Psi_{j,m} \rangle \, , \tag{124}$$

where $\Psi_{j,n}$ is the n-th eigenstate for the component $j = \mathrm{s}, \mathrm{t}, \mathrm{c}$, and $\partial_{\varphi,j}$ is the finite differences matrix for the first derivative of that component (as defined in Appendix 5.6.1). We can then use this to write all necessary $\tilde{H}$ terms which will contribute to the system Hamiltonian for the three micromaser components and their couplings.

These terms can again be written in matrix form in Mathematica by considering the derivative operators as partial difference matrices. For the cross terms, we can evaluate the matrix elements of the derivative operators for each component independently, which we can do since the derivative operators of each component commute with each other. Then, for each term in the Hamiltonian of the system, we write it in matrix form by taking a Kronecker product of the matrices for each component in that term. For example, in the T_{st} term, we take a Kronecker product of the identity matrix in the cavity's basis, the matrix of transmon first derivative terms evaluated via $\langle \Psi_{\mathrm{t},n} | \, \partial_{\varphi,\mathrm{t}} \, | \Psi_{\mathrm{t},m} \rangle$, and the matrix of SNAIL first derivative terms evaluated via $\langle \Psi_{\mathrm{s},n} | \, \partial_{\varphi,\mathrm{s}} \, | \Psi_{\mathrm{s},m} \rangle$.

We write the contribution of the pump, which acts on the SNAIL directly, as

$$H_{\mathrm{pump}} = i\Omega \cos(\omega_{\mathrm{p}} t) \dot{\varphi}_{\mathrm{s}}, \tag{125}$$

where Ω is the amplitude of the pump and ω_{p} is the frequency of the pump.

As the snail-transmon coupling is much stronger than the transmon cavity coupling, we proceed by diagonalizing the artificial atom Hamiltonian $H_{\mathrm{aa}} = \tilde{H}_{\mathrm{s}} + \tilde{H}_{\mathrm{t}} + \tilde{H}_{\mathrm{st}}$, once again using Mathematica's Eigensystem[] solver. In the eigenbasis of the artificial atom Hamiltonian the basis states are nearly product states of the original basis with a fixed photon number on each component – which allows us to label the new eigenstates by photon numbers. We identify the labeling by finding the component of the new basis states in the old basis which has the maximum amplitude, indicating the greatest overlap with that state in the old basis. It is in this new basis that we apply Lindbladian loss which affects the

SNAIL and transmon [86]. Specifically, SNAIL photon loss is applied between eigenstates of the artificial atom which differ by one photon in the SNAIL (according to their most similar states in the original basis). The same is true for transmon photon loss, which is applied between eigenstates which differ by one photon in the transmon (according to their most similar states in the original basis). This scheme for applying the Lindbladian terms reduces the effect of Purcell loss, the origin of which is discussed in Ref. [86]. We apply these losses in an uncorrelated way. I.e., we consider a Lindbladian associated with the loss between any two states independently, rather than a single Lindbladian operator encompassing all SNAIL or transmon loss processes. The reason for treating the different loss processes as incoherent is that the photon frequencies associated with the different loss processes are different from each other because of the nonlinearities of the artificial atom subsystem. On the other hand, for the cavity loss, we consider a single Lindbladian with correlated losses, which are between states differing by one cavity photon.

For the pump, we take H_{pump} and transform it into the eigenbasis of the artificial atom. We keep only the terms that are relevant, that is the terms which differ by 1 photon in the SNAIL and 1 photon in the transmon. This includes, for example, pumping from the ground state of the artificial atom $|0g\rangle$ to the $|1e\rangle$ state, or from the $|1e\rangle$ to $|2f\rangle$ state, and so on. It also includes pumping from $|0e\rangle$ to $|1f\rangle$, $|1g\rangle$ to $|2e\rangle$, and similar contributions. For each state that we keep, we will find the maximum magnitude of the matrix element (when $t = 0$) and incorporate the rotation as $\exp(i\omega_{\text{p}}t)$. We refer to this new, reduced pump as $\tilde{H}_{\text{pump}}$.

We then write the master equation of the system,

$$\begin{aligned}\dot{\rho} = &-i[H_{\text{aa}} + \tilde{H}_{\text{c}} + \tilde{H}_{\text{tc}} + \tilde{H}_{\text{pump}}, \rho] \\ &+\chi_{\text{s}} \sum_{i=1}^{n_{\text{s}}} \left(\hat{\text{s}}_i \rho \hat{\text{s}}_i^\dagger - \frac{1}{2}\hat{\text{s}}_i^\dagger \hat{\text{s}}_i \rho - \frac{1}{2}\rho \hat{\text{s}}_i^\dagger \hat{\text{s}}_i\right) \\ &+\chi_{\text{t}} \sum_{i=1}^{n_{\text{t}}} \left(\hat{\text{t}}_i \rho \hat{\text{t}}_i^\dagger - \frac{1}{2}\hat{\text{t}}_i^\dagger \hat{\text{t}}_i \rho - \frac{1}{2}\rho \hat{\text{t}}_i^\dagger \hat{\text{t}}_i\right) \\ &+\chi_{\text{c}}\left(\hat{\text{c}} \rho \hat{\text{c}}^\dagger - \frac{1}{2}\hat{\text{c}}^\dagger \hat{\text{c}} \rho - \frac{1}{2}\rho \hat{\text{c}}^\dagger \hat{\text{c}}\right),\end{aligned} \tag{126}$$

where ρ is the density matrix for the system and χ_j is the decay rate for the component j (SNAIL, transmon, cavity). The operators $\hat{s}_i$ and $\hat{t}_i$ and their Hermitian conjugates are the creation and annihilation operators which induce transitions between eigenstates in the

artificial atom basis where the SNAIL and transmon photon numbers change by one. We have separate operators for each pair of states of the artificial atom in order to implement uncorrelated losses. The number of states in our Hilbert space for each of these components is n_{s} for the SNAIL and n_{t} for the transmon. For the cavity, we write the standard creation and annihilation operators as $\hat{c}^{\dagger}, \hat{c}$ since losses are correlated (n_{c}, the number of states we consider in the cavity, does not appear in the expression above for this reason). We have ensured that our choices of $n_{\mathrm{s}}, n_{\mathrm{t}}, n_{\mathrm{c}}$ are sufficient for the conditions we simulate by checking that our results do not vary significantly as we increase these cutoffs.

This master equation can be considered as a superoperator $\mathcal{L}$ for $\dot{\rho}$ acting on ρ, i.e. $\dot{\rho} = \mathcal{L}\rho$. This matrix $\mathcal{L}$ can be written in Mathematica by extracting the coefficients of each term of the density operator from the master equation. However, this superoperator contains rotating terms due to the pump, which makes analysis of the system more complex. To simplify the problem, we transform to a rotating basis and drop the remaining rotating terms, as described in Appendix 5.6.3. Then, the steady state of the maser can be determined by computing the eigenstate of $\mathcal{L}$ which has eigenvalue 0. The next smallest eigenvalue by real part gives the linewidth of the system. Therefore, constructing and analyzing $\mathcal{L}$ allows us to determine maser behavior which we can sweep over experimental parameters such as transmon and pump frequencies.

We use Mathematica's Eigensystem[] solver to find the zero eigenvector as well as the eigenvectors associated with the next few smallest eigenvalues. This, combined with the fact that our superoperator is a sparse matrix, allows us to use methods which make this computational problem tractable. In particular, here we use the Arnoldi method, which can quickly evaluate the smallest eigenvectors and eigenvalues of large sparse matrices.

Using the zero eigenvector, which in this case represents the steady-state density matrix, we compute the population of the masing cavity, indicating maser brightness, over a sweep of transmon and pump frequencies and across a range of pump power. In Fig. 46, we plot the brightness of the maser as it is related to these two system parameters, and plot this for increasing pump power. Due to the computational intensity of the task, we model the cavity with only 10 states, and therefore the maximum number of photons that can occupy the cavity is 9. In our model, we consider the maser to be bright if this maximum number of

photons is saturated. For small pump power, we see two bright spots indicating two masing modes. The spot at lower transmon frequency represents the masing scheme in which the transmon's first excited state to ground transition is tuned to the cavity spacing, i.e. the $|0e\rangle \rightarrow |0g\rangle$ masing mode. The spot at higher transmon frequency is due to masing when the transmon's second excited state to first excited state transition is equal to the cavity spacing, i.e. the $|0f\rangle \rightarrow |0e\rangle$ masing mode. We see that as the pump power is increased, these spots brighten and eventually merge, with masing possible at a wide range of transmon frequencies.

However, the Hatlab is also able to measure a third bright spot at a transmon frequency between the other two. We associate this third bright spot with the two-photon masing mode described in Fig. 44(c), i.e. the $|0f\rangle \rightarrow |0g\rangle$ masing mode. We are able to see this masing mode in our simulation if we increase the atom-cavity coupling sufficiently, as shown in Fig. 47, where in addition to the two single-photon masing modes, we see a distinct third bright spot at an intermediate transmon frequency. This demonstrates a qualitative agreement between our theory and the experimental results, and we are working on a joint paper with Hatlab on this maser.

5.4 Theory of masing via non Jaynes-Cummings atom-cavity coupling

In this Section, we will model a simpler masing system which is composed of a two-level atom and a masing cavity. This system allows us to modify the atom-cavity coupling and directly probe how this affects maser brightness and linewidth. We will start by writing down a maser equation which describes an atom with drive from the ground state to the excited state, a cavity with decay, and a coupling Hamiltonian which allows us to specify a coupling operator. Then, we will consider a set of five coupling operators including the Jaynes-Cummings operator, the Suskind-Glogower operator, and combinations of these. We will then compute how laser linewidth decreases with cavity population in cases of different coupling strengths and operators, and see how they compare to the standard quantum limit. Finally, we will look closely at the cavity population distribution in two-photon masing cases,

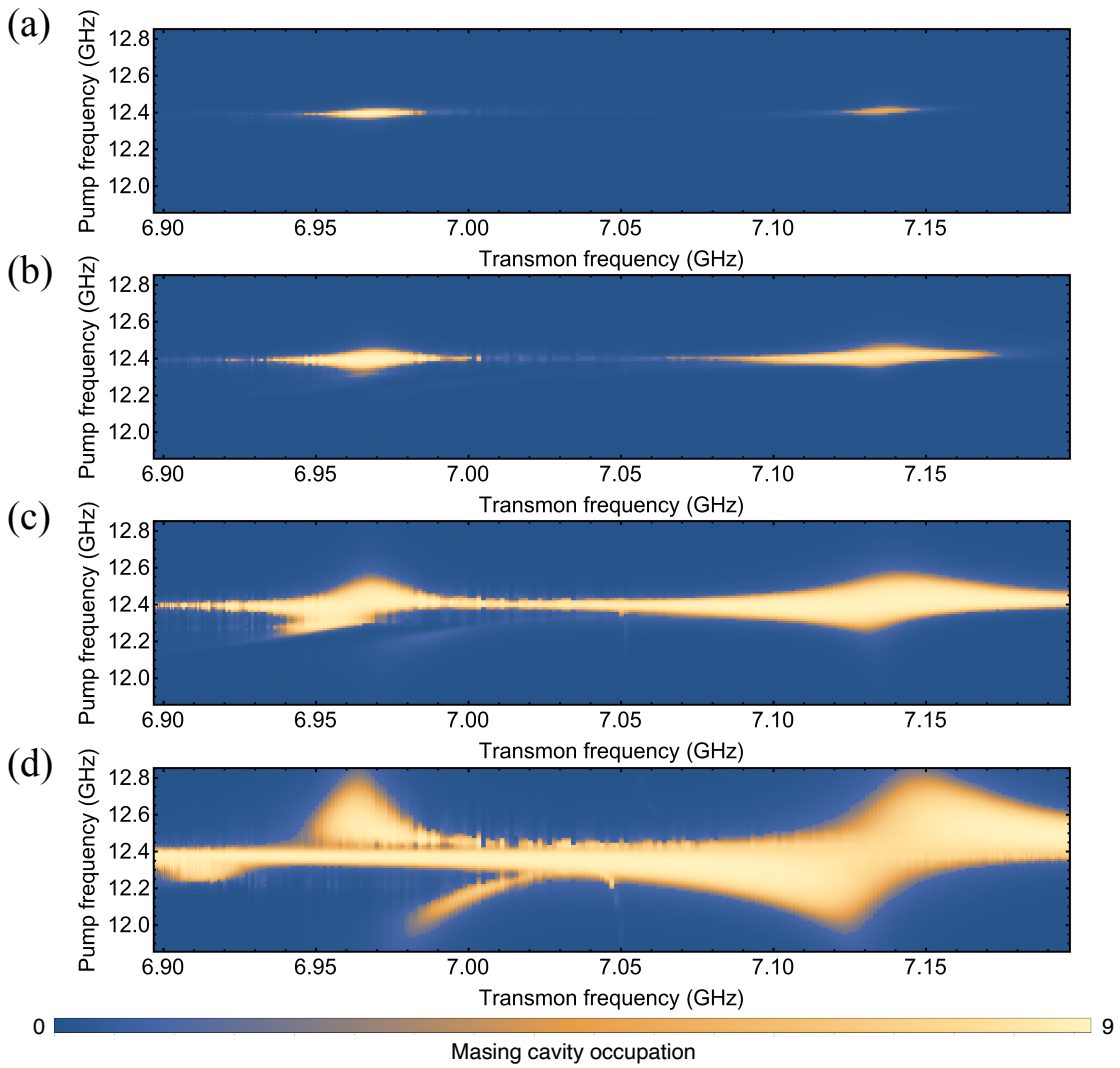

Figure 46: Occupation of the masing cavity according to our simulation for varying transmon and pump frequencies. From panel (a) to (d), we show maser brightness for increasing pump power. We associate the bright region at a lower transmon frequency with the ordinary masing scheme, while the bright region at a higher transmon frequency represents the first alternative masing scheme.

and see that it introduces a bistable masing mode.

We begin by modeling the maser as a single atom with two levels and a masing cavity.

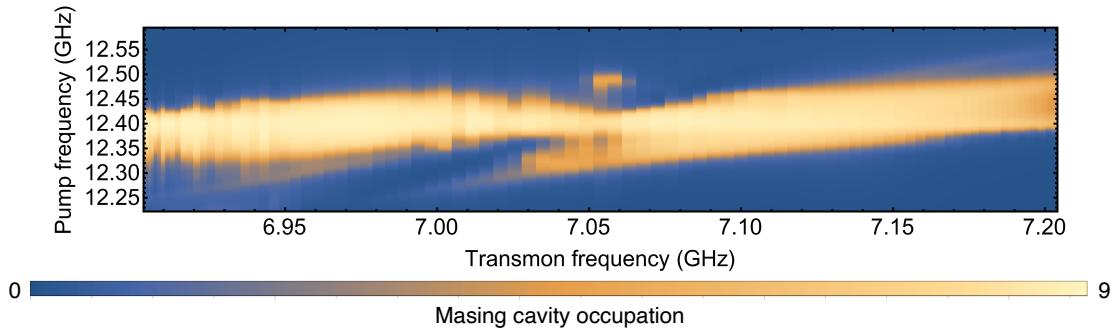

Figure 47: Occupation of the masing cavity according to our simulation for varying transmon and pump frequencies with atom-cavity coupling strength increased. There is now a third distinct bright spot, which we associate with a two-photon transition.

These are coupled by a Hamiltonian

$$H = g(\sigma_+ a + a^\dagger \sigma_-) \tag{127}$$

where σ_+, σ_- are the raising and lowering operators for the atom and $a^\dagger, a$ are generic operators which act on the photon number in the cavity. This is the interaction Hamiltonian in the Jaynes-Cummings model of a two-level atom coupled to a cavity field [52]. In an ordinary maser, these operators would be $c^\dagger, c$ which are the usual creation and annihilation operators. When acting on a state $|n\rangle$ of the cavity, we have $c\,|n\rangle = \sqrt{n}\,|n-1\rangle$ and $c^\dagger\,|n\rangle = \sqrt{n+1}\,|n+1\rangle$.

We write this Hamiltonian in Mathematica by writing the creation and annihilation operators for the cavity and the atom as matrices, and taking a Kronecker product between them. Then, the Hamiltonian is constructed via simple matrix multiplication.

In order to write the master equation for this maser, we must consider the incoherent drive of the atom to its excited state as well as cavity loss. We incorporate both via Lindbladian

terms so that the master equation becomes

$$\begin{aligned}\dot{\rho} = &- i[H, \rho] \\ &+\Omega_d\big(\sigma_-\rho\sigma_+\frac{1}{2}\sigma_+\sigma_-\rho - \frac{1}{2}\rho\sigma_+\sigma_-\big) \\ &+\chi_c\big(a\rho a^\dagger - \frac{1}{2}a^\dagger a\rho - \frac{1}{2}\rho a^\dagger a\big),\end{aligned} \tag{128}$$

where ρ is the density matrix for the system, Ω_d is the drive strength on the atom, and χ_c is the decay rate of the cavity. Again, we are able to write this as an equation for the entries of ρ since we have all the necessary matrices to construct the master equation in Mathematica.

We consider alternative choices for the $a^\dagger, a$ operators. First, the Susskind-Glogower (SG) operators $e^\dagger, e$ which act on the cavity states as $e\,|n\rangle = |n-1\rangle$ and $e^\dagger\,|n\rangle = |n+1\rangle$. This and the traditional maser both represent single-photon masing modes. However, we consider three cases of two-photon masing via $a = cc, a = ec, a = ee$ and complex conjugates for $a^\dagger$. These three operators act on the cavity so as to shift the photon number by two, but vary in how the rate corresponds to the photon number in the cavity. This rate is known as the Bose enhancement factor, and in these three cases range from linear dependence on n to no dependence on n. Previous analysis of these coupling operators has found that the SG operator, where the coupling strength is independent of cavity population, provides the lowest maser linewidth [65]. In Mathematica, implementing these different couplings constitutes replacing the matrices for the usual operators with matrices which represent the SG operators, or two-photon operators formed by multiplying the matrices of two such operators together.

The master equation can be solved for the steady-state solution of the system by considering a superoperator $\mathcal{L}$ for $\dot{\rho}$ which acts on ρ, i.e. $\dot{\rho} = \mathcal{L}\rho$. By computing the eigenspectrum of $\mathcal{L}$ and identifying the eigenstate associated with a zero eigenvalue, we find the steady state of the maser which allows us to compute the population of the masing cavity. The next smallest eigenvalue by real part gives the linewidth of the maser. This process is accomplished in the same manner as in Sec, 5.3, by using Mathematica's Eigensystem[] solver with sparse matrices.

For each of our five coupling operators (two one-photon and three two-photon operators), we compute maser linewidth and cavity population over a range of drive strengths Ω_d. Then,

we can plot the linewidth against the population and compare it to the standard quantum limit and the Heisenberg limit. In each case, we also have to choose the important ratio g/χ_c, which sets the relative strength of the coupling to the decay of the cavity.

5.4.1 Results

For each of the five coupling operators, we compute maser linewidth versus cavity population to see how linewidth decreases relative to $\langle n\rangle^{-1}$ and $\langle n\rangle^{-2}$. First, it is important to establish how the ratio g/χ_c affects these results. Specifically, we anticipate that a faster decay of the cavity will lead to a lower population of the cavity before linewidth begins to decrease, and vice versa. Equivalently, a stronger coupling will lead to a higher population of the cavity before linewidth begins to decrease, and vice versa. Here, we will simulate the system with a cavity linewidth of 1 MHz (i.e. $\chi_c/(2\pi) = 1$ MHz), and we show in Fig. 48 that our expectation holds. In the Figure, we see that with a traditional $c^\dagger, c$ coupling, we see the linewidth decrease more quickly than $\langle n\rangle^{-1}$, and it approaches the standard quantum limit without reaching it, regardless of g/χ_c. We plot the standard quantum limit, $\chi_c/(4\langle n\rangle)$, and the Heisenberg limit, $\chi_c/(4\langle n\rangle)$, for reference. Note that the Heisenberg limit plotted here is correct in slope, but the particular coefficient is not relevant since a maser with cavity loss cannot achieve this limit.

At some point before reaching the standard quantum limit, the population begins to decrease (and linewidth increase) as the drive strength is increased. We ascribe this to a "quantum Zeno" effect, where more quickly resetting the two level atom to its excited state makes an effective measurement, leaving no time for photon exchange with the cavity.

We find that the appropriate choice of g/χ_c depends on the choice of coupling operator. In particular, the order of $c^\dagger, c$ operators in the coupling significantly affects the range of g/χ_c for which the inflection point occurs at a reasonable cavity population. In this case, "reasonable" means that the inflection point is sufficiently above 1 photon since our standard quantum limit is only meaningful in the regime of a more populated cavity. The inflection point must also occur at a low enough population that we can tractably compute the linewidth, since it takes ever greater computational resources to do this calculation with a greater cavity

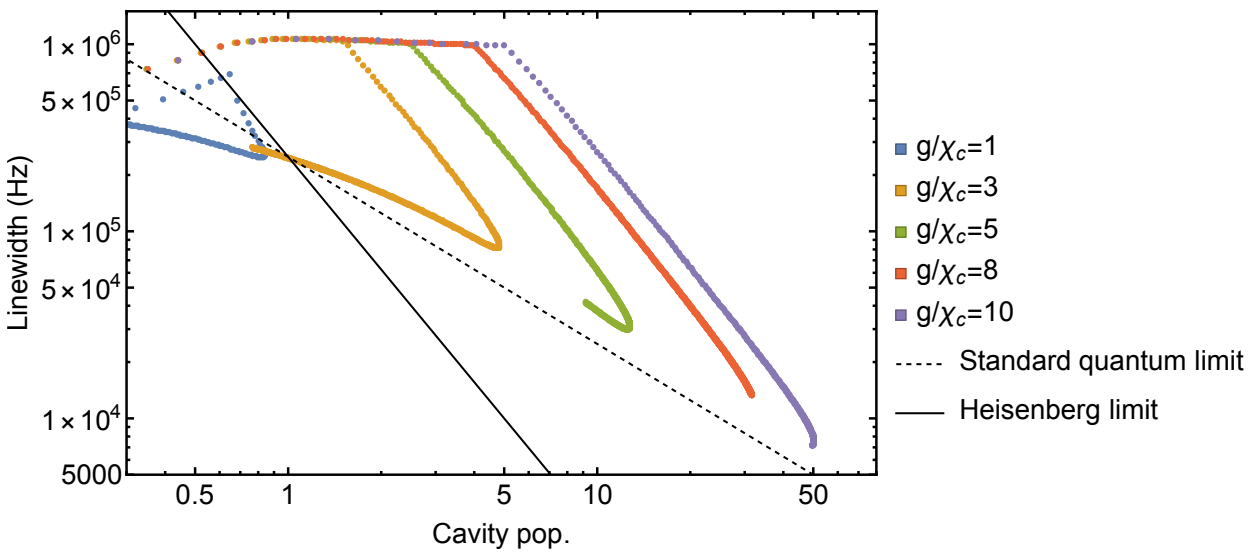

Figure 48: Linewidth versus cavity population for a tradition $c^\dagger, c$ operator with various g/χ_c. The Heisenberg limit as shown here gives the correct slope, but cannot be achieved with cavity loss.

population. We in general limit this calculation to 200 cavity photons as simulating more becomes unreasonably slow. We find that reasonable g/χ_c for coupling operators with no $c^\dagger, c$ component (i.e. $a = e$ or $a = ee$) is on the order of $g/\chi_c = 100$. For $a = c$ or $a = ec$, reasonable g/χ_c is around 10. For $a = cc$, reasonable g/χ_c is approximately 1.

Next, we compare the behavior of the maser with each coupling operator with an appropriate choice of g/χ_c. In Fig. 49, we plot linewidth versus cavity population for $a = cc$ with $g/\chi_c = 1$, $a = c$ and $a = ec$ with $g/\chi_c = 10$, and $a = e$ and $a = ee$ with $g/\chi_c = 50$. The case with two $c^\dagger, c$ operators, i.e. $a = cc$, has a linewidth which decreases as $\langle n \rangle^{-1}$. This is not as narrow as the standard case with the single $c^\dagger, c$ operator (i.e. $a = c$), which has linewidth that decreases as $\langle n \rangle^{-2}$ until near the standard quantum limit. The same is also true for the $a = ec$ case, although the details of how the linewidth approaches the standard quantum limit are different (Fig. 50). That is, the linewidth slightly passes the limit before turning around due to the quantum Zeno effect. The two cases with $a = e$ and $a = ee$ have linewidth which decreases below the standard quantum limit, and ultimately approaches half

the limit.

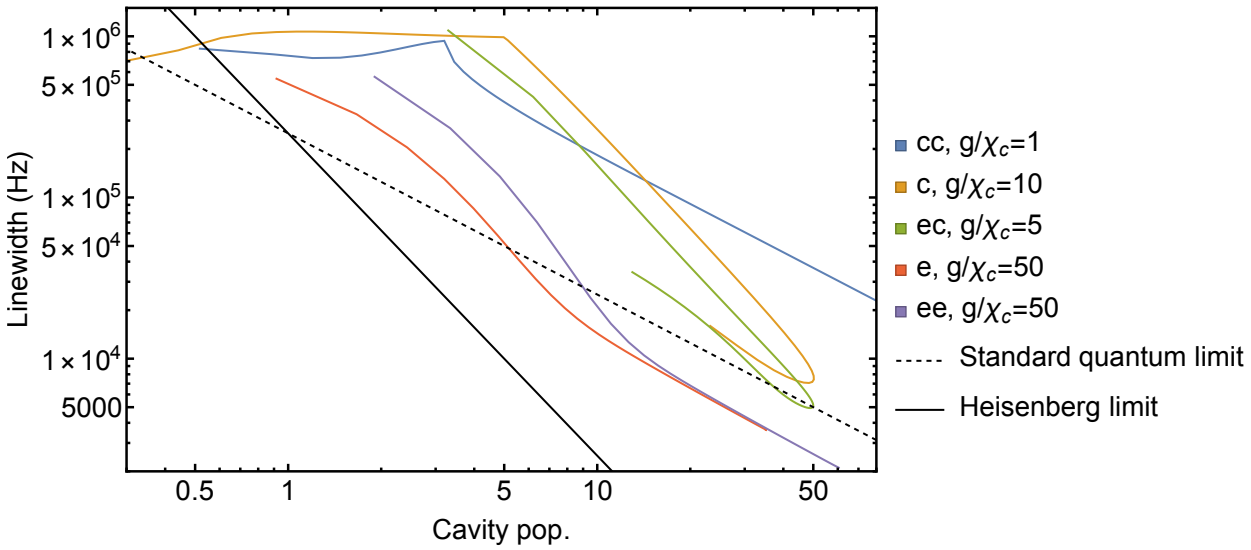

Figure 49: Linewidth versus cavity population for each of the 5 coupling operators; $a = cc$, $a = c$, $a = ec$, $a = e$, and $a = ee$. The Heisenberg limit as shown here gives the correct slope, but cannot be achieved with cavity loss.

In addition to the linewidth of the maser, we can compute the width of the cavity photon number distribution in each case. In the typical case, where $a = c$, the width of this distribution grows with the population n as $\sqrt{n}$. However, the $a = cc$ case is wider, with a distribution width which grows as $\sqrt{2n}$, as shown in Fig. 51. The $a = cc$ case is particularly interesting because, on closer inspection, the distribution of the cavity populations is bimodal for certain choices of parameters. Shown in Fig. 52 for $g/\chi_c = 0.9$, the distribution appears to have a mode with low cavity population, a dark mode, in addition to a bright mode, indicating a bistable maser.

It remains unclear why this choice of coupling operator should lead to this bistability, but we can confirm that the second mode is stable by looking at the smallest eigenvalues by real part. As usual, the first eigenvalue by real part should be 0, indicating a stable solution. In the $a = cc$ case, as the drive is increased, the second eigenvalue decreases and reaches zero. Rather than representing the linewidth of the maser, this represents a second stable solution. In this case, the linewidth can be extracted from the third eigenvalue. Fig. 53

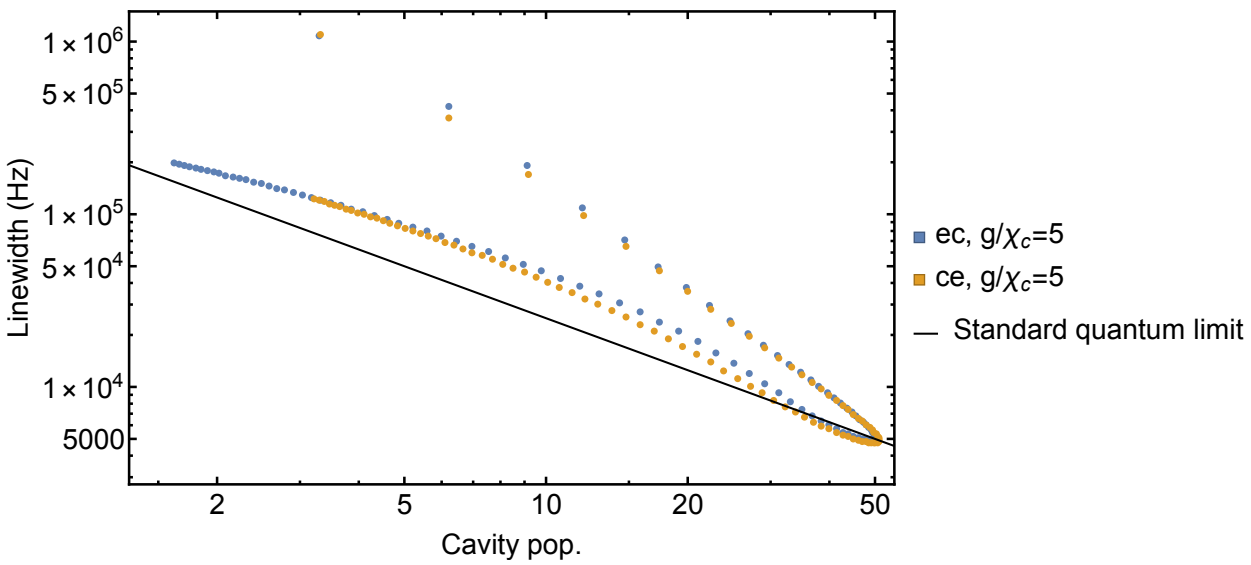

Figure 50: Linewidth versus cavity population for $a = ec$ and $a = ce$. The order of the two operators in the coupling operator a does not significantly affect the linewidth versus cavity population.

shows these first three eigenvalues, with the second eigenvalue decreasing to zero, indicating that a second stable solution arises.

5.5 Summary

We have modeled the Hatlab micromaser and as a result have determined the origin of regions of peak maser brightness that result from sweeping maser operating parameters. Our model captures the physics of the nonlinear superconducting components whose level structure contributes to the maser output.

This masing system inspires us to consider ways to reduce maser linewidth by designing a novel atom-cavity coupler which is composed of nonlinear superconducting elements. We show that using coupling operators with different Bose enhancement factors can reduce the maser linewidth. Realizing such a maser in a physical system would require engineering

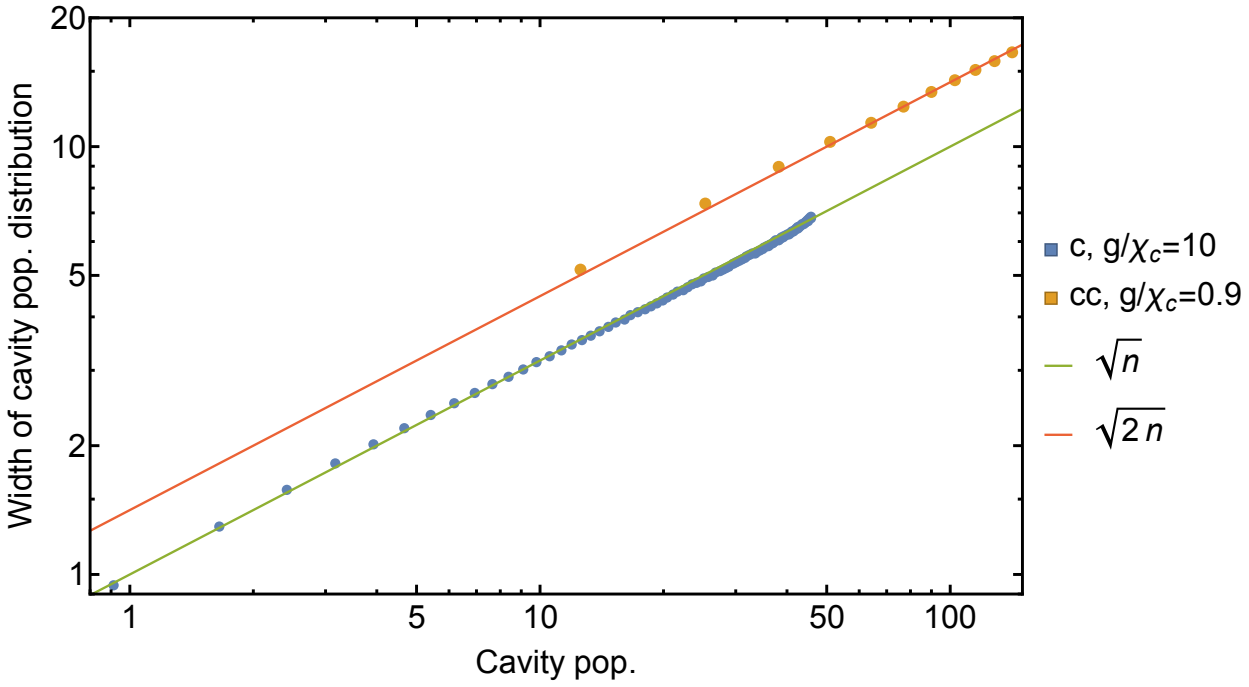

Figure 51: Width of cavity population distribution versus cavity population for $a = c$ and $a = cc$.

coupling circuits which implement these operators. Further research in this domain could draw from the circuit modeling and optimization techniques laid out in Chapter 4, so that these coupling circuits could be designed to minimize linewidth.

This masing system also represents a source of coherent light available at low temperatures in a dilution refrigerator without the need for AC control lines. Coherent light sources are essential in many scientific applications, including spectroscopy and interferometry. More specialized applications range from cooling systems such as Doppler cooling and velocity-selective coherent population trapping which are used in atomic clocks and trapped ion systems, to optical tweezers which are used in molecular biology. Lasers, as a source of coherent light, have led to a vast range of innovations, and the work in this Chapter provides a new kind of coherent light source which may prove to have many analogous applications.

We also observe new phenomena with respect to the cavity photon number distribution

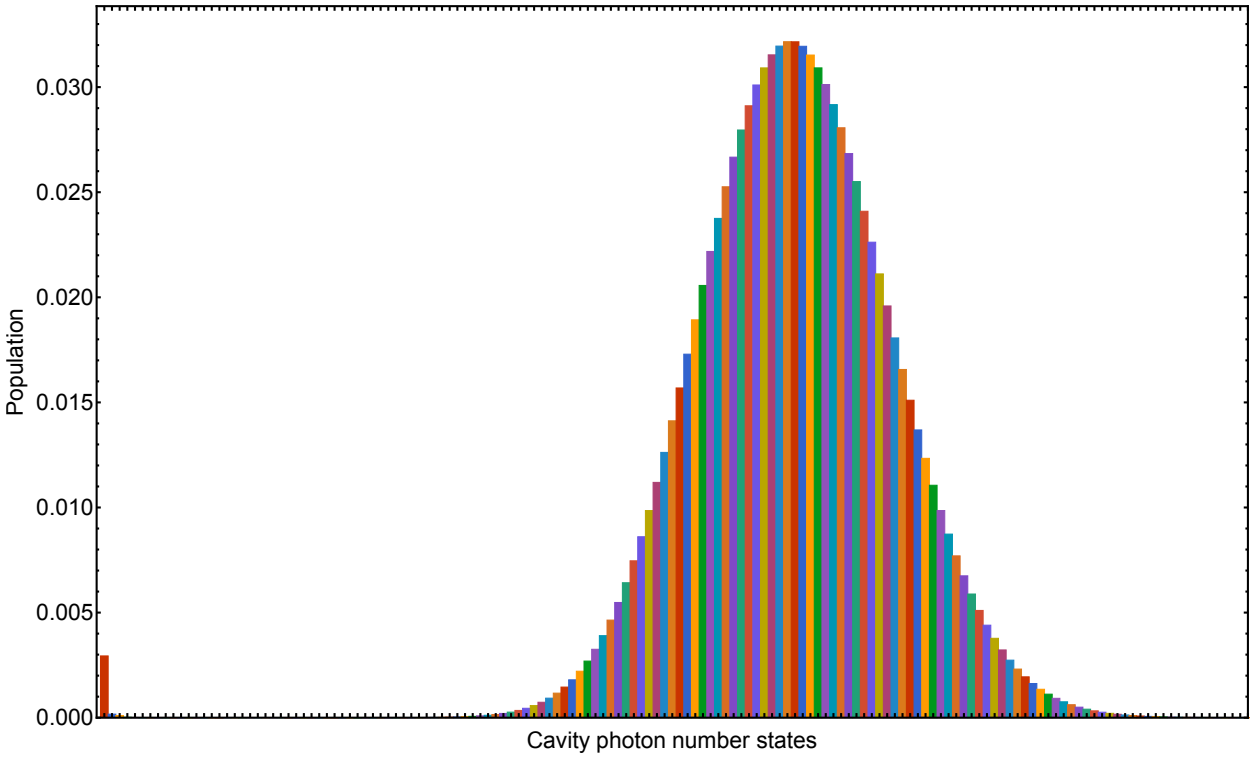

Figure 52: Population distribution of cavity with $a = cc$ and $g/\chi_c = 0.9$ with the drive strength set so as to demonstrate the bistability. There is a small peak at photon number zero in the cavity, as well as a larger primary peak representing a bright maser.

of two-photon masers with Bose enhancement factor larger than that of traditional masers. We find that such a maser may be bistable for certain ratios of the atom-cavity coupling and the cavity decay rate. This raises the possibility of designing future devices which take advantage of this bistability to operate as the maser a sensor.

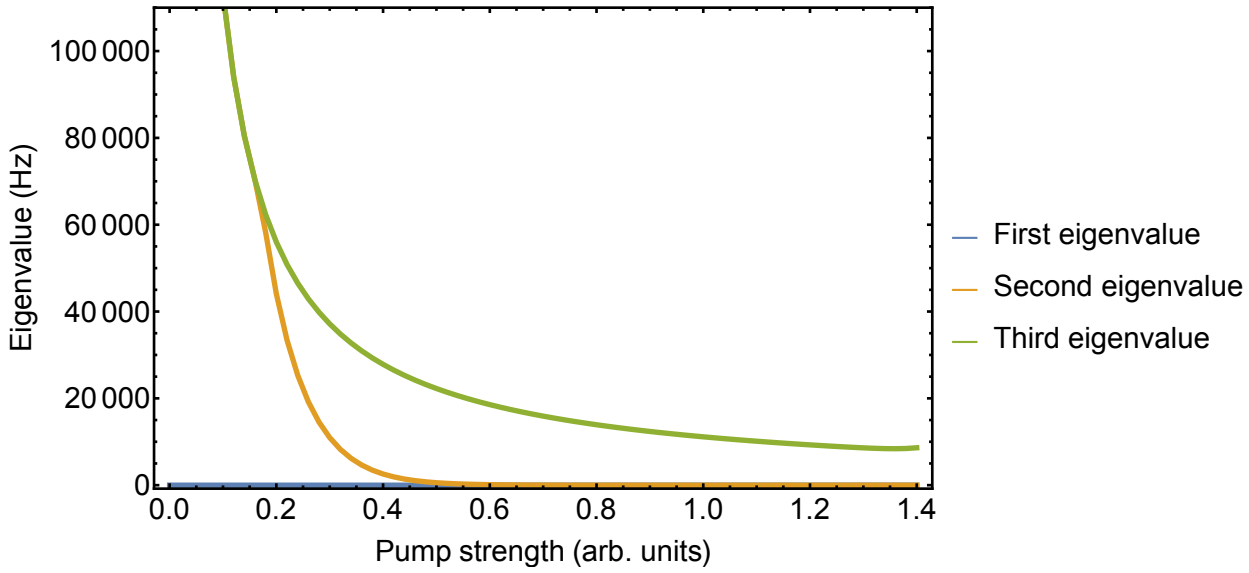

Figure 53: The first three eigenvalues of the $a = cc$ maser with $g/\chi_c = 0.9$. The eigenvalues are sorted from smallest to largest by real part. The first is always zero, indicating a stable solution. The second and third are initially similar, both being equal to the linewidth of the stable mode. As drive increases, a second mode becomes stable, so the second eigenvalue reaches zero.

5.6 Appendix

5.6.1 Derivative operators

Upon quantization, the momentum operator $C\dot{\varphi}$ becomes $-i\hbar\partial_\varphi$ (and we use the units where $\hbar = 1$). In order to implement derivatives in the discrete Hamiltonian, we use the finite differences method to define operators for first and second derivatives for each component. Given the value of a function Ψ at a point φ_0 and its nearest neighbors in a grid with spacing h_φ, we express the first and second derivatives at the point as

$$f'(\varphi_0) = \frac{-f(\varphi_0 - h_\varphi) + f(\varphi_0 + h_\varphi)}{2h_\varphi} \tag{129}$$

$$f''(\varphi_0) = \frac{f(\varphi_0 - h_\varphi) - 2f(\varphi_0) + f(\varphi_0 + h_\varphi)}{h_\varphi^2}. \tag{130}$$

Therefore, the discrete first derivative operator with respect to φ for each component j (SNAIL, transmon, cavity) can be expressed as

$$\partial_{\varphi,j} = \frac{1}{2h_{\varphi,j}} \begin{pmatrix} 0 & 1 & 0 & 0 & \dots \\ -1 & 0 & 1 & 0 & \dots \\ 0 & -1 & 0 & 1 & \dots \\ 0 & 0 & -1 & 0 & \dots \\ \vdots & \vdots & \vdots & \vdots & \ddots \end{pmatrix} \tag{131}$$

where for each component we select an appropriate spacing $h_{\varphi,j}$. For the cavity, we use $n_{\mathrm{c}} = 14000$ and $h_{\varphi,\mathrm{c}} = 0.0003$. This small spacing is necessary to preserve the harmonic nature of the cavity. We have confirmed that this n_{c} is sufficient by verifying that the spacings of the cavity states are the same to within 2 kHz, which is small compared to the spacings themselves which are on the order of 7 GHz. For the transmon and the SNAIL, the total range of phase possible is fixed (to 2π for the transmon and 4π for the SNAIL due to the SNAIL design). We select $n_{\mathrm{t}} = 1000$ and $n_{\mathrm{s}} = 1000$, fixing the spacing of points for each. Since the transmon and SNAIL are periodic, we set the top right and bottom left elements in the first derivative matrix to -1 and 1, respectively, since the points at 0 and 2π are equivalent. We build the second derivative matrix for each component in a similar manner. We confirm that n_{s} and n_{t} are sufficient since the energies of their first five levels do not change significantly by increasing these parameters further, as show in Fig. 54.

5.6.2 Fitting and modeling the SNAIL

Modeling our SNAIL, like modeling the transmon and cavity, requires fitting its circuit parameters such that the SNAIL behavior matches experimental data. However, the SNAIL is more complicated than the other components because we include in our model a stray linear inductance L_{lin} which divides the phase φ_{s}. Therefore, the SNAIL is dependent not only on φ_{s}, but also on φ_{s1} which is itself dependent on φ_{s}, as it is the phase which minimizes the energy of the SNAIL component for a given value of φ_{s}. In discretizing the phase variable for the SNAIL, the phase φ_{s1} must be determined for each desired value of φ_{s}.

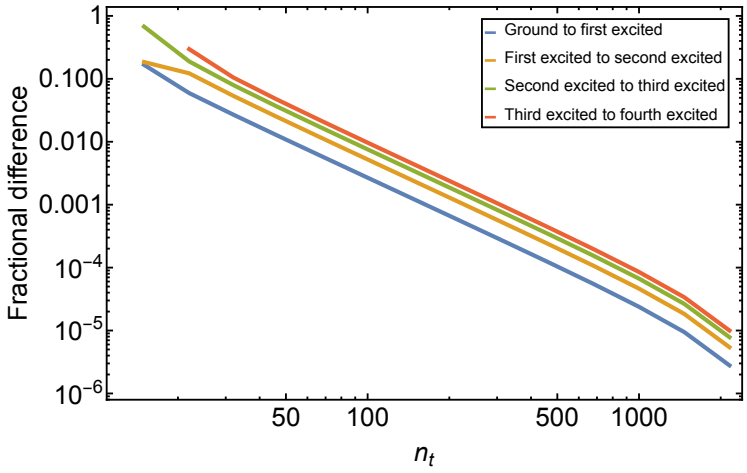

Figure 54: Convergence of spacing of the levels of the transmon. For various n_t, we plot the spacings between the 5 lowest levels to show how they converge as n_t increases. Here, we plot the fractional difference between these spacings and the spacings computed with $n_\mathrm{t} = 3000$. By $n_\mathrm{t} = 1000$, the difference is smaller than one part per 10000, and so we consider this sufficient.

With this intermediate phase considered in our model, we have 3 fitting parameters to determine, $i_{\mathrm{s1}}, i_{\mathrm{s2}},$ and L_{lin}. The capacitance C_s is determined directly by experiment to be 341 pF. To find the values of the fitting parameters, we fit the ground state to first excited state transition to experimental data as shown in Fig. 55.

5.6.3 Applying a rotating frame and dropping rotating terms

The master equation as written in Eq. (126) contains rotating terms due to the pump. We apply a rotation which takes us to a frame where these rotating terms are stationary which allows for tractable analysis of the master equation without integrating in time to find the steady state solution. In particular, we apply the unitary transformation which rotates the system based on the number of photons in the SNAIL. That is, each state is rotated by $e^{is\omega_\mathrm{p}t}$, where s is the number of photons in the SNAIL (in the transformed basis where SNAIL and transmon are hybridized). We apply the rotation in this way since the pump

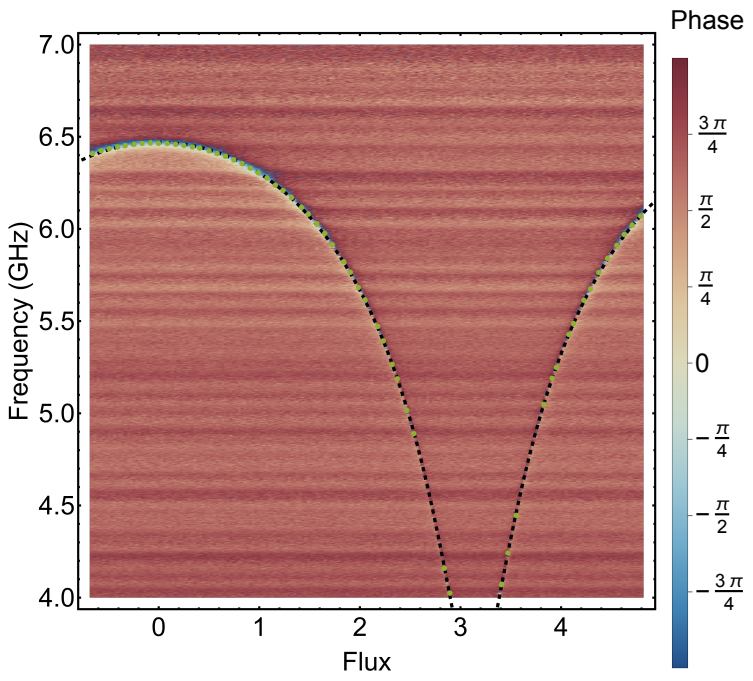

Figure 55: Plot of the ground to first excited state transition of the SNAIL. The green points are extracted from the experimental data and lie along the transition over the flux sweep. The black dotted line shows the frequency of the transition according to our theory after fitting.

acts on the SNAIL, inducing a rotation at ω_p. This counter-rotation applies to terms in the pump which link two states with different SNAIL photon number, with the counter-rotation always having a net effect of rotating by $-\omega_p$. The result is that the pump, when written in the rotating frame, contains only stationary terms. However, any rotation will induce new rotating terms in $\tilde{H}_{tc}$, the transmon cavity coupling. The rotation we have chosen is advantageous since the most important terms in this coupling do not couple states with different SNAIL number, and thus will not be rotating when applying our transformation. After applying our rotation, we drop all remaining rotating terms in $\tilde{H}_{tc}$ and arrive at a new Hamiltonian with no rotating terms which closely approximates the original Hamiltonian.

6.0 Conclusions

In this Dissertation, we have discussed the simulation and modeling of several superconducting quantum systems and their results. Here, we will summarize the important results of each Chapter.

In Chapter 2, we used tight-binding and continuum models to compute the band structure of monolayer graphene under an arbitrary periodic electrostatic potential. We found that certain potentials, particularly those with symmetries similar to that of the graphene lattice itself, can result in flat bands near the chemical potential. This result inspires the idea of using an electrostatic potential for band engineering which could reveal new properties in graphene, akin to the discovery of superconductivity in magic angle twisted bilayer graphene.

In Chapter 3, we modeled the behavior of mesoscopic DC-SQUIDs written at the interface of complex oxides. These devices differ from typical DC-SQUIDs since they have low superfluid density and are small enough to be entirely penetrated by external fields. In this work, we extracted important device parameters of the SQUIDs and formed a theoretical explanation for unusual experimental results, namely the short period of oscillation of critical current with magnetic field and the asymmetry between the positive and negative critical currents in the device. Two-dimensional superconductors in this material which can be reprogrammed via c-AFM lithography could form the basis for manufacturing superconducting devices with novel properties in the future.

In Chapter 4, we investigated improving the power added efficiency of Josephson parametric amplifiers by optimizing the inductive blocks in JPA circuits. We started by introducing a semiclassical model for the dynamics of these circuits, and used this to model RF-SQUID amplifiers and optimize their parameters for high PAE. We then investigated additional circuit designs, and established a new circuit design rule. Namely, we found that amplifier circuits composed of repeating chains of inductive elements should avoid elements with nonmonotonic current-phase relations since these result in unstable amplification. We then proposed circuits which extend the RF-SQUID amplifier design by adding new tuning parameters to these circuits, allowing for higher PAE. Our optimized RF-SQUID amplifiers

and extended RF-SQUID amplifiers achieve PAE which is several orders of magnitude higher than previous designs, being as high as 42.6% as compared to around 0.1%. This greatly improved PAE makes JPAs more useful in superconducting quantum computing applications since less heat needs to be dissipated in millikelvin environments with limited cooling power available. This may allow for multiplexing applications where more amplifiers must be located in the same dilution refrigerator to amplify signals from many qubits, and so this work represents an important step in scaling superconducting quantum computing systems.

In Chapter 5, we simulated a micromaser composed of superconducting quantum computing components in order to explain phenomena observed in micromaser experiments. We found that the multiple bright operating regions of the maser are due to the nonlinearities of the maser's components which provide a sophisticated band structure which allows for multiple masing modes. We then explored the theoretical possibility of using nonstandard atom-cavity coupling in these systems, and showed that this can introduce a bistable maser with dark and bright states.

Bibliography

[1] The BCS theory of superconductivity. `https://www.weizmann.ac.il/condmat/oreg/sites/condmat.oreg/files/uploads/2016/tutorial_3.pdf`, 2016.

[2] Low noise factory. `https://lownoisefactory.com/`, Oct 2023.

[3] Eva Y Andrei and Allan H MacDonald. Graphene bilayers with a twist. *Nature materials*, 19(12):1265–1275, 2020.

[4] Jose Aumentado. Superconducting parametric amplifiers: The state of the art in josephson parametric amplifiers. *IEEE Microwave Magazine*, 21(8):45–59, 2020.

[5] Travis J. Baker, Seyed N. Saadatmand, Dominic W. Berry, and Howard M. Wiseman. The heisenberg limit for laser coherence. *Nature Physics*, 17(2):179–183, October 2020.

[6] M. Barbier, P. Vasilopoulos, and F. M. Peeters. Extra dirac points in the energy spectrum for superlattices on single-layer graphene. *Phys. Rev. B*, 81:075438, Feb 2010.

[7] J. Bardeen, L. N. Cooper, and J. R. Schrieffer. Theory of superconductivity. *Physical Review*, 108(5):1175–1204, December 1957.

[8] N. Bergeal, F. Schackert, M. Metcalfe, R. Vijay, V. E. Manucharyan, L. Frunzio, D. E. Prober, R. J. Schoelkopf, S. M. Girvin, and M. H. Devoret. Phase-preserving amplification near the quantum limit with a josephson ring modulator. *Nature*, 465(7294):64–68, May 2010.

[9] N. Bergeal, R. Vijay, V. E. Manucharyan, I. Siddiqi, R. J. Schoelkopf, S. M. Girvin, and M. H. Devoret. Analog information processing at the quantum limit with a josephson ring modulator. *Nature Physics*, 6(4):296–302, February 2010.

[10] Doron L. Bergman, Congjun Wu, and Leon Balents. Band touching from real-space topology in frustrated hopping models. *Phys. Rev. B*, 78:125104, Sep 2008.

[11] R. Bistritzer and A. H. MacDonald. Moire bands in twisted double-layer graphene. *Proceedings of the National Academy of Sciences*, 108(30):12233–12237, July 2011.

[12] Alexandre Blais, Arne L. Grimsmo, S.M. Girvin, and Andreas Wallraff. Circuit quantum electrodynamics. *Reviews of Modern Physics*, 93(2), May 2021.

[13] Samuel Boutin, David M. Toyli, Aditya V. Venkatramani, Andrew W. Eddins, Irfan Siddiqi, and Alexandre Blais. Effect of higher-order nonlinearities on amplification and squeezing in josephson parametric amplifiers. *Phys. Rev. Appl.*, 8:054030, Nov 2017.

[14] L. Brey and H. A. Fertig. Emerging zero modes for graphene in a periodic potential. *Phys. Rev. Lett.*, 103:046809, Jul 2009.

[15] Yuan Cao, Valla Fatemi, Ahmet Demir, Shiang Fang, Spencer L. Tomarken, Jason Y. Luo, Javier D. Sanchez-Yamagishi, Kenji Watanabe, Takashi Taniguchi, Efthimios Kaxiras, Ray C. Ashoori, and Pablo Jarillo-Herrero. Correlated insulator behaviour at half-filling in magic-angle graphene superlattices. *Nature*, 556(7699):80–84, March 2018.

[16] Yuan Cao, Valla Fatemi, Shiang Fang, Kenji Watanabe, Takashi Taniguchi, Efthimios Kaxiras, and Pablo Jarillo-Herrero. Unconventional superconductivity in magic-angle graphene superlattices. *Nature*, 556(7699):43–50, March 2018.

[17] Stephen Carr, Daniel Massatt, Shiang Fang, Paul Cazeaux, Mitchell Luskin, and Efthimios Kaxiras. Twistronics: Manipulating the electronic properties of two-dimensional layered structures through their twist angle. *Phys. Rev. B*, 95:075420, Feb 2017.

[18] M. A. Castellanos-Beltran and K. W. Lehnert. Widely tunable parametric amplifier based on a superconducting quantum interference device array resonator. *Applied Physics Letters*, 91(8):083509, 08 2007.

[19] Manuel A. Castellanos-Beltran, Kent D. Irwin, Leila R. Vale, Gene C. Hilton, and Konrad W. Lehnert. Bandwidth and dynamic range of a widely tunable josephson parametric amplifier. *IEEE Transactions on Applied Superconductivity*, 19(3):944–947, 2009.

[20] A. H. Castro Neto, F. Guinea, N. M. R. Peres, K. S. Novoselov, and A. K. Geim. The electronic properties of graphene. *Rev. Mod. Phys.*, 81:109–162, Jan 2009.

[21] Carlton M. Caves. Quantum limits on noise in linear amplifiers. *Phys. Rev. D*, 26:1817–1839, Oct 1982.

[22] C. Cen, S. Thiel, G. Hammerl, C. W. Schneider, K. E. Andersen, C. S. Hellberg, J. Mannhart, and J. Levy. Nanoscale control of an interfacial metal–insulator transition at room temperature. *Nature Materials*, 7(4):298–302, March 2008.

[23] Cheng Cen, Stefan Thiel, Jochen Mannhart, and Jeremy Levy. Oxide nanoelectronics on demand. *Science*, 323(5917):1026–1030, February 2009.

[24] S. Chaudhuri, D. Li, K. D. Irwin, C. Bockstiegel, J. Hubmayr, J. N. Ullom, M. R. Vissers, and J. Gao. Broadband parametric amplifiers based on nonlinear kinetic inductance artificial transmission lines. *Applied Physics Letters*, 110(15), April 2017.

[25] A. Chaves, J. G. Azadani, Hussain Alsalman, D. R. da Costa, R. Frisenda, A. J. Chaves, Seung Hyun Song, Y. D. Kim, Daowei He, Jiadong Zhou, A. Castellanos-Gomez, F. M. Peeters, Zheng Liu, C. L. Hinkle, Sang-Hyun Oh, Peide D. Ye, Steven J. Koester, Young Hee Lee, Ph. Avouris, Xinran Wang, and Tony Low. Bandgap engineering of two-dimensional semiconductor materials. *npj 2d materials and applications*, 4(1), August 2020.

[26] Long Chen. Finite difference methods for poisson equation. https://www.math.uci.edu/ chenlong/226/FDM.pdf, 2008.

[27] Shunfeng Chen, Yuanjie Ning, Chi Sin Tang, Liang Dai, Shengwei Zeng, Kun Han, Jun Zhou, Ming Yang, Yanqun Guo, Chuanbing Cai, Ariando Ariando, Andrew T. S. Wee, and Xinmao Yin. Laalo3/srtio3 heterointerface: 20 years and beyond. *Advanced Electronic Materials*, 10(3), January 2024.

[28] Zheng Chen, Zhongran Liu, Yanqiu Sun, Xiaoxin Chen, Yuan Liu, Hui Zhang, Hekang Li, Meng Zhang, Siyuan Hong, Tianshuang Ren, Chao Zhang, He Tian, Yi Zhou, Jirong Sun, and Yanwu Xie. Two-dimensional superconductivity at the $LaAlO_3/KTaO_3$ heterointerface. *Physical Review Letters*, 126(2), January 2021.

[29] Kevin S. Chou, Tali Shemma, Heather McCarrick, Tzu-Chiao Chien, James D. Teoh, Patrick Winkel, Amos Anderson, Jonathan Chen, Jacob Curtis, Stijn J. de Graaf, John W. O. Garmon, Benjamin Gudlewski, William D. Kalfus, Trevor Keen, Nishaad Khedkar, Chan U Lei, Gangqiang Liu, Pinlei Lu, Yao Lu, Aniket Maiti, Luke Mastalli-Kelly, Nitish Mehta, Shantanu O. Mundhada, Anirudh Narla, Taewan Noh, Takahiro Tsunoda, Sophia H. Xue, Joseph O. Yuan, Luigi Frunzio, Jose Aumentado, Shruti Puri, Steven M. Girvin, Jr. au2 S. Harvey Moseley, and Robert J. Schoelkopf. Demonstrating a superconducting dual-rail cavity qubit with erasure-detected logical measurements, 2023.

[30] A. A. Clerk, M. H. Devoret, S. M. Girvin, Florian Marquardt, and R. J. Schoelkopf. Introduction to quantum noise, measurement, and amplification. *Reviews of Modern Physics*, 82(2):1155–1208, April 2010.

[31] N. Du, N. Force, R. Khatiwada, E. Lentz, R. Ottens, L.J Rosenberg, G. Rybka, G. Carosi, N. Woollett, D. Bowring, A.S. Chou, A. Sonnenschein, W. Wester, C. Boutan, N.S. Oblath, R. Bradley, E.J. Daw, A.V. Dixit, J. Clarke, S.R. O'Kelley, N. Crisosto, J.R. Gleason, S. Jois, P. Sikivie, I. Stern, N.S. Sullivan, D.B Tanner, and G.C. Hilton. Search for invisible axion dark matter with the axion dark matter experiment. *Physical Review Letters*, 120(15), April 2018.

[32] Sudipta Dubey, Vibhor Singh, Ajay K Bhat, Pritesh Parikh, Sameer Grover, Rajdeep Sensarma, Vikram Tripathi, K Sengupta, and Mandar M Deshmukh. Tunable superlattice in graphene to control the number of dirac points. *Nano letters*, 13(9):3990–3995, 2013.

[33] Sudipta Dubey, Vibhor Singh, Ajay K. Bhat, Pritesh Parikh, Sameer Grover, Rajdeep Sensarma, Vikram Tripathi, K. Sengupta, and Mandar M. Deshmukh. Tunable superlattice in graphene to control the number of dirac points. *Nano Letters*, 13(9):3990–3995, August 2013.

[34] Christopher Eichler and Andreas Wallraff. Controlling the dynamic range of a josephson parametric amplifier. *EPJ Quantum Technology*, 1(1):2, Jan 2014.

[35] M. J. Feldman and M. T. Levinsen. Gain-dependent noise temperature of josephson parametric amplifiers. *Applied Physics Letters*, 36(10):854–856, 05 1980.

[36] M. J. Feldman, P. T. Parrish, and R. Y. Chiao. Parametric amplification by unbiased josephson junctions. *Journal of Applied Physics*, 46(9):4031–4042, 09 1975.

[37] P. Filipowicz, Juha Javanainen, and P. Meystre. The micromaser. In *International Quantum Electronics Conference*, page TUOO1. Optica Publishing Group, 1986.

[38] Carlos Forsythe, Xiaodong Zhou, Kenji Watanabe, Takashi Taniguchi, Abhay Pasupathy, Pilkyung Moon, Mikito Koshino, Philip Kim, and Cory R. Dean. Band structure engineering of 2d materials using patterned dielectric superlattices. *Nature Nanotechnology*, 13(7):566–571, May 2018.

[39] S. Frasca, C. Roy, G. Beaulieu, and P. Scarlino. Three-wave-mixing quantum-limited kinetic inductance parametric amplifier operating at 6 t near 1 k. *Physical Review Applied*, 21(2), February 2024.

[40] N. E. Frattini, V. V. Sivak, A. Lingenfelter, S. Shankar, and M. H. Devoret. Optimizing the nonlinearity and dissipation of a snail parametric amplifier for dynamic range. *Phys. Rev. Appl.*, 10:054020, Nov 2018.

[41] Maria N. Gastiasoro, Jonathan Ruhman, and Rafael M. Fernandes. Superconductivity in dilute $SrTiO_3$: A review. *Annals of Physics*, 417:168107, June 2020.

[42] A. K. Geim and K. S. Novoselov. The rise of graphene. *Nature Materials*, 6(3):183–191, March 2007.

[43] V. L. Ginzburg and L. D. Landau. On the theory of superconductivity. *Zh. Eksperim. i. Teor. Fiz.*, 20:1064, 1950.

[44] S. M. Girvin. *Circuit QED: superconducting qubits coupled to microwave photons*, page 113–256. Oxford University PressOxford, June 2014.

[45] Srijit Goswami, Emre Mulazimoglu, Ana M. R. V. L. Monteiro, Roman Wölbing, Dieter Koelle, Reinhold Kleiner, Ya. M. Blanter, Lieven M. K. Vandersypen, and Andrea D. Caviglia. Quantum interference in an interfacial superconductor. *Nature Nanotechnology*, 11(10):861–865, July 2016.

[46] Per Brinch Hansen. Numerical solution of laplace's equation. https://surface.syr.edu/eecs_techreports/168/, Sep 1992.

[47] M. Hatridge, S. Shankar, M. Mirrahimi, F. Schackert, K. Geerlings, T. Brecht, K. M. Sliwa, B. Abdo, L. Frunzio, S. M. Girvin, R. J. Schoelkopf, and M. H. Devoret. Quantum back-action of an individual variable-strength measurement. *Science*, 339(6116):178–181, 2013.

[48] E. Hoskinson, Y. Sato, I. Hahn, and R. E. Packard. Transition from phase slips to the josephson effect in a superfluid 4he weak link. *Nature Physics*, 2(1):23–26, December 2005.

[49] Nicholas Hougland, Ranjani Ramachandran, Jeremy Levy, and David Pekker. Theory of engineering flat bands in graphene using doubly-periodic electrostatic gating, 2021.

[50] Nicholas M. Hougland, Zhuan Li, Ryan Kaufman, Boris Mesits, Roger S. K. Mong, Michael Hatridge, and David Pekker. Pump-efficient josephson parametric amplifiers with high saturation power. *Physical Review A*, 111(2), February 2025.

[51] Mengchen Huang, Giriraj Jnawali, Jen-Feng Hsu, Shonali Dhingra, Hyungwoo Lee, Sangwoo Ryu, Feng Bi, Fereshte Ghahari, Jayakanth Ravichandran, Lu Chen, et al. Electric field effects in graphene/laalo3/srtio3 heterostructures and nanostructures. *APL materials*, 3(6):062502, 2015.

[52] E.T. Jaynes and F.W. Cummings. Comparison of quantum and semiclassical radiation theories with application to the beam maser. *Proceedings of the IEEE*, 51(1):89–109, 1963.

[53] Giriraj Jnawali, Hyungwoo Lee, Jung-Woo Lee, Mengchen Huang, Jen-Feng Hsu, Feng Bi, Rongpu Zhou, Guanglei Cheng, Brian D'Urso, Patrick Irvin, et al. Graphene-complex-oxide nanoscale device concepts. *ACS nano*, 12(6):6128–6136, 2018.

[54] B.D. Josephson. Possible new effects in superconductive tunnelling. *Physics Letters*, 1(7):251–253, July 1962.

[55] Ryan Kaufman, Chenxu Liu, Katarina Cicak, Boris Mesits, Mingkang Xia, Chao Zhou, Maria Nowicki, José Aumentado, David Pekker, and Michael Hatridge. Simple, high saturation power, quantum-limited, rf squid array-based josephson parametric amplifiers. *In Preparation*, 2024.

[56] Ryan Kaufman, Theodore White, Mark I. Dykman, Andrea Iorio, George Sterling, Sabrina Hong, Alex Opremcak, Andreas Bengtsson, Lara Faoro, Joseph C. Bardin, Tim Burger, Robert Gasca, and Ofer Naaman. Josephson parametric amplifier with chebyshev gain profile and high saturation. *Phys. Rev. Appl.*, 20:054058, Nov 2023.

[57] Martin Koch, Daniel M. Mittleman, Jan Ornik, and Enrique Castro-Camus. Terahertz time-domain spectroscopy. *Nature Reviews Methods Primers*, 3(1), June 2023.

[58] Sebastian Krinner, Nathan Lacroix, Ants Remm, Agustin Di Paolo, Elie Genois, Catherine Leroux, Christoph Hellings, Stefania Lazar, Francois Swiadek, Johannes Herrmann, Graham J. Norris, Christian Kraglund Andersen, Markus Müller, Alexandre Blais, Christopher Eichler, and Andreas Wallraff. Realizing repeated quantum error correction in a distance-three surface code. *Nature*, 605(7911):669–674, May 2022.

[59] Yoonseok Lee. BCS theory and superconductivity. https://www.phys.ufl.edu/courses/phy4523/spring12/Sample%202.pdf, 2012.

[60] Akash Levy, Feng Bi, Mengchen Huang, Shicheng Lu, Michelle Tomczyk, Guanglei Cheng, Patrick Irvin, and Jeremy Levy. Writing and low-temperature characterization of oxide nanostructures. *Journal of Visualized Experiments*, (89), July 2014.

[61] Yutao Li, Scott Dietrich, Carlos Forsythe, Takashi Taniguchi, Kenji Watanabe, Pilkyung Moon, and Cory R. Dean. Anisotropic band flattening in graphene with one-dimensional superlattices. *Nature Nanotechnology*, 16(5):525–530, February 2021.

[62] K. K. Likharev. Superconducting weak links. *Reviews of Modern Physics*, 51(1):101–159, January 1979.

[63] K.K. Likharev and L.A. Lakobson. Steady-state properties of superconducting bridges. *Zhurnal Tekhnicheskoi Fiziki*, 45:1503–1509, July 1975.

[64] Z. R. Lin, K. Inomata, W. D. Oliver, K. Koshino, Y. Nakamura, J. S. Tsai, and T. Yamamoto. Single-shot readout of a superconducting flux qubit with a flux-driven josephson parametric amplifier. *Applied Physics Letters*, 103(13):132602, 09 2013.

[65] C Liu, M Mucci, X Cao, M V G Dutt, M Hatridge, and D Pekker. Proposal for a continuous wave laser with linewidth well below the standard quantum limit. *Nature Communications*, 12(5620), 2021.

[66] Changjiang Liu, Xi Yan, Dafei Jin, Yang Ma, Haw-Wen Hsiao, Yulin Lin, Terence M. Bretz-Sullivan, Xianjing Zhou, John Pearson, Brandon Fisher, J. Samuel Jiang, Wei Han, Jian-Min Zuo, Jianguo Wen, Dillon D. Fong, Jirong Sun, Hua Zhou, and Anand Bhattacharya. Two-dimensional superconductivity and anisotropic transport at $KTaO_3$ (111) interfaces. *Science*, 371(6530):716–721, February 2021.

[67] Changjiang Liu, Xianjing Zhou, Deshun Hong, Brandon Fisher, Hong Zheng, John Pearson, Jidong Samuel Jiang, Dafei Jin, Michael R. Norman, and Anand Bhattacharya. Tunable superconductivity and its origin at ktao3 interfaces. *Nature Communications*, 14(1), February 2023.

[68] Chenxu Liu, Tzu-Chiao Chien, Michael Hatridge, and David Pekker. Optimizing josephson-ring-modulator-based josephson parametric amplifiers via full hamiltonian control. *Phys. Rev. A*, 101:042323, Apr 2020.

[69] J. M. B. Lopes dos Santos, N. M. R. Peres, and A. H. Castro Neto. Graphene bilayer with a twist: Electronic structure. *Phys. Rev. Lett.*, 99:256802, Dec 2007.

[70] Xiaobo Lu, Petr Stepanov, Wei Yang, Ming Xie, Mohammed Ali Aamir, Ipsita Das, Carles Urgell, Kenji Watanabe, Takashi Taniguchi, Guangyu Zhang, Adrian Bachtold, Allan H. MacDonald, and Dmitri K. Efetov. Superconductors, orbital magnets and correlated states in magic-angle bilayer graphene. *Nature*, 574(7780):653–657, October 2019.

[71] F. Mallet, M. A. Castellanos-Beltran, H. S. Ku, S. Glancy, E. Knill, K. D. Irwin, G. C. Hilton, L. R. Vale, and K. W. Lehnert. Quantum state tomography of an itinerant squeezed microwave field. *Phys. Rev. Lett.*, 106:220502, Jun 2011.

[72] S. Mallik, G. C. Ménard, G. Saïz, H. Witt, J. Lesueur, A. Gloter, L. Benfatto, M. Bibes, and N. Bergeal. Superfluid stiffness of a ktao3-based two-dimensional electron gas. *Nature Communications*, 13(1), August 2022.

[73] Michel E. Marhic, Peter A. Andrekson, Periklis Petropoulos, Stojan Radic, Christophe Peucheret, and Mahmoud Jazayerifar. Fiber optical parametric amplifiers in optical communication systems. *Laser & Photonics Reviews*, 9(1):50–74, September 2014.

[74] J. F. Marques, B. M. Varbanov, M. S. Moreira, H. Ali, N. Muthusubramanian, C. Zachariadis, F. Battistel, M. Beekman, N. Haider, W. Vlothuizen, A. Bruno, B. M. Terhal, and L. DiCarlo. Logical-qubit operations in an error-detecting surface code. *Nature Physics*, 18(1):80–86, December 2022.

[75] Edward McCann and Mikito Koshino. The electronic properties of bilayer graphene. *Reports on Progress in Physics*, 76(5):056503, apr 2013.

[76] K. S. Novoselov, A. K. Geim, S. V. Morozov, D. Jiang, M. I. Katsnelson, I. V. Grigorieva, S. V. Dubonos, and A. A. Firsov. Two-dimensional gas of massless dirac fermions in graphene. *Nature*, 438(7065):197–200, November 2005.

[77] K. S. Novoselov, A. K. Geim, S. V. Morozov, D. Jiang, Y. Zhang, S. V. Dubonos, I. V. Grigorieva, and A. A. Firsov. Electric field effect in atomically thin carbon films. *Science*, 306(5696):666–669, 2004.

[78] K. S. Novoselov, D. Jiang, F. Schedin, T. J. Booth, V. V. Khotkevich, S. V. Morozov, and A. K. Geim. Two-dimensional atomic crystals. *Proceedings of the National Academy of Sciences*, 102(30):10451–10453, July 2005.

[79] A. Ohtomo and H. Y. Hwang. A high-mobility electron gas at the laalo3/srtio3 heterointerface. *Nature*, 427(6973):423–426, January 2004.

[80] Gor'kov L. P. Microscopic derivation of the ginzburg-landau equations in the theory of superconductivity. *Zh. Eksperim. i. Teor. Fiz.*, 36:1918, June 1959.

[81] Cheol-Hwan Park, Young-Woo Son, Li Yang, Marvin L. Cohen, and Steven G. Louie. Landau levels and quantum hall effect in graphene superlattices. *Phys. Rev. Lett.*, 103:046808, Jul 2009.

[82] Cheol-Hwan Park, Li Yang, Young-Woo Son, Marvin L. Cohen, and Steven G. Louie. Anisotropic behaviours of massless dirac fermions in graphene under periodic potentials. *Nature Physics*, 4(3):213–217, February 2008.

[83] Cheol-Hwan Park, Li Yang, Young-Woo Son, Marvin L. Cohen, and Steven G. Louie. New generation of massless dirac fermions in graphene under external periodic potentials. *Phys. Rev. Lett.*, 101:126804, Sep 2008.

[84] Cheol-Hwan Park, Li Yang, Young-Woo Son, Marvin L. Cohen, and Steven G. Louie. New generation of massless dirac fermions in graphene under external periodic potentials. *Phys. Rev. Lett.*, 101:126804, Sep 2008.

[85] Daniel J. Parker, Mykhailo Savytskyi, Wyatt Vine, Arne Laucht, Timothy Duty, Andrea Morello, Arne L. Grimsmo, and Jarryd J. Pla. Degenerate parametric amplification via three-wave mixing using kinetic inductance. *Phys. Rev. Appl.*, 17:034064, Mar 2022.

[86] Param Jitendra Patel, Mingkang Xia, Chao Zhou, Pineli Lu, Xi Cao, Israa Yusuf, Maria Mucci, and Michael Hatridge. The waves-in-space purcell effect for superconducting qubits. *In Preparation*, 2025.

[87] J. Pearl. Current distribution in superconducting films carrying quantized fluxoids. *Applied Physics Letters*, 5(4):65–66, August 1964.

[88] Jesper Goor Pedersen and Thomas Garm Pedersen. Band gaps in graphene via periodic electrostatic gating. *Phys. Rev. B*, 85:235432, Jun 2012.

[89] David Pekker, Alexey Bezryadin, David S. Hopkins, and Paul M. Goldbart. Operation of a superconducting nanowire quantum interference device with mesoscopic leads. *Physical Review B*, 72(10), September 2005.

[90] Hoi Chun Po, Liujun Zou, T. Senthil, and Ashvin Vishwanath. Faithful tight-binding models and fragile topology of magic-angle bilayer graphene. *Phys. Rev. B*, 99:195455, May 2019.

[91] Hoi Chun Po, Liujun Zou, Ashvin Vishwanath, and T. Senthil. Origin of mott insulating behavior and superconductivity in twisted bilayer graphene. *Phys. Rev. X*, 8:031089, Sep 2018.

[92] D. M. Pozar. *Microwave Engineering, 4th Edition*. Wiley, Hoboken, New Jersey, 2011.

[93] M. Renger, S. Pogorzalek, Q. Chen, Y. Nojiri, K. Inomata, Y. Nakamura, M. Partanen, A. Marx, R. Gross, F. Deppe, and K. G. Fedorov. Beyond the standard quantum limit for parametric amplification of broadband signals. *npj Quantum Information*, 7(1), November 2021.

[94] N. Reyren, S. Thiel, A. D. Caviglia, L. Fitting Kourkoutis, G. Hammerl, C. Richter, C. W. Schneider, T. Kopp, A.-S. Rüetschi, D. Jaccard, M. Gabay, D. A. Muller, J.-M. Triscone, and J. Mannhart. Superconducting interfaces between insulating oxides. *Science*, 317(5842):1196–1199, August 2007.

[95] Ananda Roy and Michel Devoret. Introduction to parametric amplification of quantum signals with josephson circuits. *Comptes Rendus Physique*, 17(7):740–755, 2016.

[96] Martin Rymarz and David P. DiVincenzo. Consistent quantization of nearly singular superconducting circuits. *Phys. Rev. X*, 13:021017, May 2023.

[97] A. L. Schawlow and C. H. Townes. Infrared and optical masers. *Physical Review*, 112(6):1940–1949, December 1958.

[98] J. F. Schooley, W. R. Hosler, and Marvin L. Cohen. Superconductivity in semiconducting $SrTiO_3$. *Physical Review Letters*, 12(17):474–475, April 1964.

[99] Marlan O. Scully and M. Suhail Zubairy. *Quantum optics*. Cambridge University Press, Cambridge, 1997.

[100] Likun Shi, Jing Ma, and Justin C W Song. Gate-tunable flat bands in van der waals patterned dielectric superlattices. *2D Materials*, 7(1):015028, December 2019.

[101] V. V. Sivak, A. Eickbusch, B. Royer, S. Singh, I. Tsioutsios, S. Ganjam, A. Miano, B. L. Brock, A. Z. Ding, L. Frunzio, S. M. Girvin, R. J. Schoelkopf, and M. H. Devoret. Real-time quantum error correction beyond break-even. *Nature*, 616(7955):50–55, March 2023.

[102] V. V. Sivak, N. E. Frattini, V. R. Joshi, A. Lingenfelter, S. Shankar, and M. H. Devoret. Kerr-free three-wave mixing in superconducting quantum circuits. *Phys. Rev. Appl.*, 11:054060, May 2019.

[103] Charles Slichter. Introduction to the history of superconductivity. https://history.aip.org/exhibits/mod/superconductivity/01.html, 2007.

[104] David M.P. Smith, Laurens Bakker, Roel H. Witvers, Bert E.M. Woestenburg, and Keith D. Palmer. Low noise amplifier for radio astronomy. *International Journal of Microwave and Wireless Technologies*, 5(4):453–461, January 2013.

[105] E. Suárez Morell, J. D. Correa, P. Vargas, M. Pacheco, and Z. Barticevic. Flat bands in slightly twisted bilayer graphene: Tight-binding calculations. *Phys. Rev. B*, 82:121407(R), Sep 2010.

[106] Zhuxing Sun and Yun Hang Hu. How magical is magic-angle graphene? *Matter*, 2(5):1106–1114, May 2020.

[107] Grigory Tarnopolsky, Alex Jura Kruchkov, and Ashvin Vishwanath. Origin of magic angles in twisted bilayer graphene. *Phys. Rev. Lett.*, 122:106405, Mar 2019.

[108] J. R. Thompson, L. A. Boatner, and J. O. Thomson. Very low-temperature search for superconductivity in semiconducting ktao3. *Journal of Low Temperature Physics*, 47(5–6):467–475, June 1982.

[109] Michael Tinkham. *Introduction to Superconductivity, Second Edition*. Dover Publications, Mineola, New York, 2004.

[110] R. Vijay, D. H. Slichter, and I. Siddiqi. Observation of quantum jumps in a superconducting artificial atom. *Phys. Rev. Lett.*, 106:110502, Mar 2011.

[111] Pauli Virtanen, Ralf Gommers, Travis E. Oliphant, Matt Haberland, Tyler Reddy, David Cournapeau, Evgeni Burovski, Pearu Peterson, Warren Weckesser, Jonathan Bright, Stéfan J. van der Walt, Matthew Brett, Joshua Wilson, K. Jarrod Millman, Nikolay Mayorov, Andrew R. J. Nelson, Eric Jones, Robert Kern, Eric Larson,

C J Carey, İlhan Polat, Yu Feng, Eric W. Moore, Jake VanderPlas, Denis Laxalde, Josef Perktold, Robert Cimrman, Ian Henriksen, E. A. Quintero, Charles R. Harris, Anne M. Archibald, Antônio H. Ribeiro, Fabian Pedregosa, Paul van Mulbregt, and SciPy 1.0 Contributors. SciPy 1.0: Fundamental Algorithms for Scientific Computing in Python. *Nature Methods*, 17:261–272, 2020.

[112] Uri Vool and Michel Devoret. Introduction to quantum electromagnetic circuits. *International Journal of Circuit Theory and Applications*, 45(7):897–934, 2017.

[113] P. R. Wallace. The band theory of graphite. *Physical Review*, 71(9):622–634, May 1947.

[114] T. C. White, J. Y. Mutus, I.-C. Hoi, R. Barends, B. Campbell, Yu Chen, Z. Chen, B. Chiaro, A. Dunsworth, E. Jeffrey, J. Kelly, A. Megrant, C. Neill, P. J. J. O'Malley, P. Roushan, D. Sank, A. Vainsencher, J. Wenner, S. Chaudhuri, J. Gao, and John M. Martinis. Traveling wave parametric amplifier with josephson junctions using minimal resonator phase matching. *Applied Physics Letters*, 106(24), June 2015.

[115] Theodore White, Alex Opremcak, George Sterling, Alexander Korotkov, Daniel Sank, Rajeev Acharya, Markus Ansmann, Frank Arute, Kunal Arya, Joseph C. Bardin, Andreas Bengtsson, Alexandre Bourassa, Jenna Bovaird, Leon Brill, Bob B. Buckley, David A. Buell, Tim Burger, Brian Burkett, Nicholas Bushnell, Zijun Chen, Ben Chiaro, Josh Cogan, Roberto Collins, Alexander L. Crook, Ben Curtin, Sean Demura, Andrew Dunsworth, Catherine Erickson, Reza Fatemi, Leslie Flores Burgos, Ebrahim Forati, Brooks Foxen, William Giang, Marissa Giustina, Alejandro Grajales Dau, Michael C. Hamilton, Sean D. Harrington, Jeremy Hilton, Markus Hoffmann, Sabrina Hong, Trent Huang, Ashley Huff, Justin Iveland, Evan Jeffrey, Mária Kieferová, Seon Kim, Paul V. Klimov, Fedor Kostritsa, John Mark Kreikebaum, David Landhuis, Pavel Laptev, Lily Laws, Kenny Lee, Brian J. Lester, Alexander Lill, Wayne Liu, Aditya Locharla, Erik Lucero, Trevor McCourt, Matt McEwen, Xiao Mi, Kevin C. Miao, Shirin Montazeri, Alexis Morvan, Matthew Neeley, Charles Neill, Ani Nersisyan, Jiun How Ng, Anthony Nguyen, Murray Nguyen, Rebecca Potter, Chris Quintana, Pedram Roushan, Kannan Sankaragomathi, Kevin J. Satzinger, Christopher Schuster, Michael J. Shearn, Aaron Shorter, Vladimir Shvarts, Jindra Skruzny, W. Clarke Smith, Marco Szalay, Alfredo Torres, Bryan W. K. Woo, Z. Jamie Yao, Ping Yeh, Juhwan Yoo, Grayson Young, Ningfeng Zhu, Nicholas Zobrist, Yu Chen, Anthony Megrant, Julian Kelly, and Ofer Naaman. Readout of a quantum processor with high dynamic range josephson parametric amplifiers. *Applied Physics Letters*, 122(1):014001, 01 2023.

[116] H. M. Wiseman. Light amplification without stimulated emission: Beyond the standard quantum limit to the laser linewidth. *Physical Review A*, 60(5):4083–4093,

November 1999.

[117] Si Wu, Matthew Killi, and Arun Paramekanti. Graphene under spatially varying external potentials: Landau levels, magnetotransport, and topological modes. *Phys. Rev. B*, 85:195404, May 2012.

[118] Dengyu Yang, Shan Hao, Jun Chen, Qing Guo, Muqing Yu, Yang Hu, Kitae Eom, Jung-Woo Lee, Chang-Beom Eom, Patrick Irvin, et al. Nanoscale control of laalo3/srtio3 metal–insulator transition using ultra-low-voltage electron-beam lithography. *Applied Physics Letters*, 117(25):253103, 2020.

[119] Matthew Yankowitz, Shaowen Chen, Hryhoriy Polshyn, Yuxuan Zhang, K. Watanabe, T. Taniguchi, David Graf, Andrea F. Young, and Cory R. Dean. Tuning superconductivity in twisted bilayer graphene. *Science*, 363(6431):1059–1064, January 2019.

[120] Muqing Yu, Nicholas Hougland, Qianheng Du, Junyi Yang, Sayanwita Biswas, Ranjani Ramachandran, Dengyu Yang, Anand Bhattacharya, David Pekker, Patrick Irvin, and Jeremy Levy. Sketched nanoscale $KTaO_3$-based superconducting quantum interference device. *Physical Review X*, 15(1), February 2025.

[121] Muqing Yu, Changjiang Liu, Dengyu Yang, Xi Yan, Qianheng Du, Dillon D. Fong, Anand Bhattacharya, Patrick Irvin, and Jeremy Levy. Nanoscale control of the metal–insulator transition at $LaAlO_3/KTaO_3$ interfaces. *Nano Letters*, 22(15):6062–6068, July 2022.

[122] B. Yurke, L. R. Corruccini, P. G. Kaminsky, L. W. Rupp, A. D. Smith, A. H. Silver, R. W. Simon, and E. A. Whittaker. Observation of parametric amplification and deamplification in a josephson parametric amplifier. *Phys. Rev. A*, 39:2519–2533, Mar 1989.

[123] B. Yurke, P. G. Kaminsky, R. E. Miller, E. A. Whittaker, A. D. Smith, A. H. Silver, and R. W. Simon. Observation of 4.2-k equilibrium-noise squeezing via a josephson-parametric amplifier. *Phys. Rev. Lett.*, 60:764–767, Feb 1988.

[124] Guanqun Zhang, Lijie Wang, Jinghui Wang, Guoan Li, Guangyi Huang, Guang Yang, Huanyi Xue, Zhongfeng Ning, Yueshen Wu, Jin-Peng Xu, Yanru Song, Zhenghua An, Changlin Zheng, Jie Shen, Jun Li, Yan Chen, and Wei Li. Spontaneous rotational symmetry breaking in ktao3 heterointerface superconductors. *Nature Communications*, 14(1), May 2023.

[125] Liujun Zou, Hoi Chun Po, Ashvin Vishwanath, and T. Senthil. Band structure of twisted bilayer graphene: Emergent symmetries, commensurate approximants, and wannier obstructions. *Phys. Rev. B*, 98:085435, Aug 2018.